FZR-406

Wissenschaftlich-Technische Berichte
FZR-406 August 2004 ISSN 1437-322X

Barbara Abendroth

Ion-induced stress relaxation during the growth of cubic boron nitride thin films

Forschungszentrum
Rossendorf

Wissenschaftlich- Technische Berichte
FZR-406
August 2004

Barbara Abendroth

Ion-induced stress relaxion during the growth of cubic boron nitride thin films

Forschungszentrum
Rossendorf

Institut für Ionenstrahlphysik und Materialforschung
Forschungszentrum Rossendorf e.V.

Ion-induced stress relaxation during the growth of cubic boron nitride thin films

von der
Fakultät Mathematik und Naturwissenschaften
der Technischen Universität Dresden
genehmigte

Dissertation
zur Erlangung des akademischen Grades
Doctor rerum naturalium
(Dr. rer. nat.)

vorgelegt von
Dipl. Min. Barbara Elisabeth Abendroth

geboren am 14.09.1974 in Darmstadt

Dresden 2004

Eingereicht am 18.02.2004

1. Gutachter: Prof. Dr. W. Möller
2. Gutachter: Prof. Dr. P. Ziemann
3. Gutachter: Prof. Dr. F. Richter

Verteidigt am 05.07.2004

Contents

Abbreviations

ADC	Analog Digital Converter
cBN	cubic Boron Nitride
CVD	Chemical Vapour Deposition
dc	Direct Current
EEDF	Electron Energy Distrubution Function
ERDA	Elastic Recoil Detection Analysis
FPUW	Force Per Units Width
FTIR	Fourier Transform Infra Red
FWHM	Full Width at Half Maximum
GID	Grazing Incidence Diffraction
hBN	hexagonal Boron Nitride
HOPBN	Highly Oriented hexagonal Boron Nitride
HPHT	High Temperature, High Pressure
HV	High Voltage
IBA	Ion Beam Analysis
IBAD	Ion Beam Assisted Deposition
IED	Ion Energy Distribution
IP	Ionization Potential
I - V	Current - Voltage
MS	Magnetron Sputtering
MSIBAD	Mass Selected IBAD
PAD	Plasma Assisted Deposition
PACVD	Plasma Assisted CVD
PDF	Powder Diffraction Files
PIII	Plasma Immersion Ion Implantation
PLD	Pulsed Laser Deposition, also Pulsed Laser Ablation
PSD	Position Sensitive Diode
PVD	Physical Vapour Deposition
rBN	rhombohedral Boron Nitride
RBS	Rutherford Backscattering Spectroscopy
r.f.	Radio Frequency
RT	Room Temperature
ta-C	Tetrahedral Amorphous Carbon
tBN	turbostratic Boron Nitride
TEM	Transmission Electron Microscopy
wBN	wurtzitic Boron Nitride
XRD	X-Ray Diffraction

1 Motivation

Among hard materials for thin film applications, cubic boron nitride (cBN) has attracted a lot of interest and a large number research activities in the last two decades. Besides the very high hardness (Vickers microhardness: H_v = 50 - 60 GPa [1, 2]), other outstanding properties give reason for the scientific interest. Superior to diamond, cBN is resistant to oxidation up to temperatures of 1300° C [3, 4] and does not react with ferrous materials [3]. This makes it a promising material for the coating of high speed cutting tools. Since cBN is transparent in the visible and infrared range, it is also a desirable material for protective coatings of optical elements. Due to its wide band gap of $\sim$ 6 eV, its ability of p- and n-type doping [5], and the high thermal conductivity of 13 $Wcm^{-1}K^{-1}$ [6] it also could be used in electronic devices.

Polycrystalline cBN was synthesized first in high temperature high pressure experiments by Wentdorf in 1957 [7]. Since the late 1980s also the preparation of cBN thin films became possible with a variety of deposition methods. It was found that cBN layers can be produced at relatively low temperatures (100 - 500° C) but in any case a bombardment with energetic particles is necessary to nucleate the cubic BN phase. The particles are usually ions in the energy range of 100 to 1000 eV. This particle bombardment of the growing film has some grave consequences for the film properties. On one hand the cubic phase does not nucleate directly on the most common substrates. This leads to a very characteristic layer structure of the films with a hexagonal BN (hBN) phase at the substrate/film interface from which the cubic phase nucleates. Additionally the thin film material is (almost) always nanocrystalline. On the other hand the ion bombardment leads to very high intrinsic compressive stress in the layers, exceeding -10 GPa. The characteristic evolution of the intrinsic stress during the layered growth of cBN was studied by in situ stress measurement during ion beam assisted deposition (IBAD) of boron nitride films by Fitz and Fukarek [8, 9].

Due to the layer structure and the poor crystallinity, up to now any application for electronic devices seemed to be not practicable. Only very recently however, the heteroepitaxial growth of cBN on diamond substrates could be demonstrated, which may open the path for the fabrication of electronic devices [10]. Regarding hard protective coatings, the high intrinsic stresses limit the adhesion of the films. Usually when the film thickness exceeds a critical thickness of some hundred nm, the films delaminate. In previous works it could be shown for IBAD that ion implantation in the energy range of 1.1 MeV to 35 keV during or after deposition significantly reduces the intrinsic stress [11–13]. Boyen et al. [12] could produce for the first time, 1 μm thick, stress released cBN layers by an alternating process of cBN IBAD and stress relaxation by ion implantation with 300 keV Ar ions. Fitz et al. used in situ stress measurement to monitor the stress relaxation in cBN induced by

medium energy ion implantation during post deposition ion implantation experiments [14] and simultaneous ion bombardment of the growing cBN film [13].

This route should enable the deposition of cBN films of μm thickness. However, IBAD has some drawbacks regarding industrial upscaling. This is mainly the low growth rate and the fact that the boron evaporation rates become unstable in long term deposition experiments. Also, for the stress relaxation, a linear accelerator providing the high energy ions is required.

On the other hand, magnetron sputter deposition offers a solution to the problems imposed on IBAD: it can be operated at high and stable deposition rates and is already widely used in the commercial deposition of hard coatings on tools. A broad knowledge of the cBN deposition regimes in magnetron sputtering has been collected by a large number of researchers along the last decade (e.g. references [15–22]). Different routes were described to produce adherent cBN films by magnetron sputtering, including the deposition of buffer layers [23, 24], the incorporation of third elements [25, 26], and the optimization of the process parameters [21, 27]. However, so far the residual stresses could not be reduced sufficiently to enable a commercial use of cBN coatings on machining tools. The possibility to apply a negative voltage to the substrate allows, also in magnetron sputtering the use of high energy ions for stress relaxation.

Out of these considerations the aims of the present work arose:

1. The deposition of cBN was to be realized by magnetron sputtering, which is a widely used method for the commercial deposition of hard coatings tools.

2. To be able to understand and control the cBN film growth, the plasma characteristics (ion flux, ion energy distribution and plasma composition) have to be known. Therefore the magnetron discharge had to be characterized by means of Langmuir probe measurements and energy selective mass spectroscopy.

3. The in situ stress measurement was to be adjusted for the magnetron sputtering process.

4. With in situ stress measurement, the stress evolution in BN films was to be measured during magnetron sputter deposition and to be compared with the results obtained previously by IBAD.

5. Stress relaxation by energetic ion bombardment was to be realized for magnetron sputtering by plasma immersion ion implantation technology using a pulsed substrate bias. In this way stress relaxation could be achievable at acceptable costs for industrial application.

6. The stress relaxation was also to be studied by in situ stress measurement. Specially the influence of the process parameters ion flux and ion energy on the stress relaxation was to be investigated with emphasis on very low ion energies (< 10 keV).

7. Changes of the microstructure of the layers induced by the ion bombardment were to be investigated. Specially the question arose whether the stress relaxation takes place within the cubic BN or it is due to a phase transformation to the hBN.

8. The parameters limiting the film adhesion were to be investigated and measures to improve the adhesion should be examined.

2 Boron nitride

2.1 Structure and properties of boron nitride

Boron nitride is isoelectronic to carbon and exists in different phases analogue to the carbon system. As in the case of carbon, boron nitride can have sp^2 or sp^3 hybridization. The structures of the crystalline boron nitride phases are shown in figure 2.1. The sp^2 hybridized phases are the hexagonal (hBN) and rhombohedral (rBN) boron nitride, which both consist of hexagonal basal planes but differ in their stacking sequence. The hBN is the analogon to graphite with an AA'A stacking sequence, whereas in the rBN the stacking of the hexagonal planes is in an ABC sequence. Due to the partial ionicity of the BN bonds the hBN is, unlike graphite, not conducting What is referred to as turbostratic boron nitride (tBN) is a low ordered form of hBN, where the hexagonal planes have random stacking and are randomly oriented around the c axis. Additionally, in tBN the spacing between the planes can be somewhat larger than the spacing in ordered hBN [28] and the hexagonal basal planes can be bended and cross-linked similar to the fullerene like structure in carbon and carbon nitride films [29]. Cubic boron nitride (cBN), which possess the Zincblende structure, is tetrahedrally coordinated with sp^3 hybridization. The high covalent degree of the bonding and the short bond length result in the very high hardness of this material. Wurtzitic boron nitride (wBN) is like the cBN sp^3 bonded and therefore also tetrahedrally coordinated. But here the unit cell is hexagonal and the stacking sequence is AA'A. Comparing the local bonding environment of cBN and wBN, in the wBN structure one of the tetrahedral bonds is elongated along the [0001] direction where the other bonds have the same length as in cBN. In thin BN films tBN and cBN are the predominant sp^2 and sp^3 phases, respectively. Table 2.1 summarizes the structural parameters of the four crystalline boron nitride phases.

The stability of the different BN allotropes was first investigated by Corrigan and Bundy in 1975 [34]. The p-T phase diagram was established with results from high pressure high temperature (HPHT) experiments [7] and extrapolation from the carbon phase diagram. The stability boundaries of Corrigan and Bundy, represented in figure 2.2 by the dashed lines, indicate that at ambient conditions hBN would be the stable phase. More recent thermodynamic [35] and ab initio calculations [36] however show that cBN is the stable phase at atmospheric pressure up to $\sim$1600 K, see figure 2.2. These calculations are supported by experimental results of Sachdev et al. [37]. The phase transition at ambient conditions is however hindered by kinetic barrier and as will be seen in the next section, cBN thin film deposition takes place at conditions far from equilibrium.

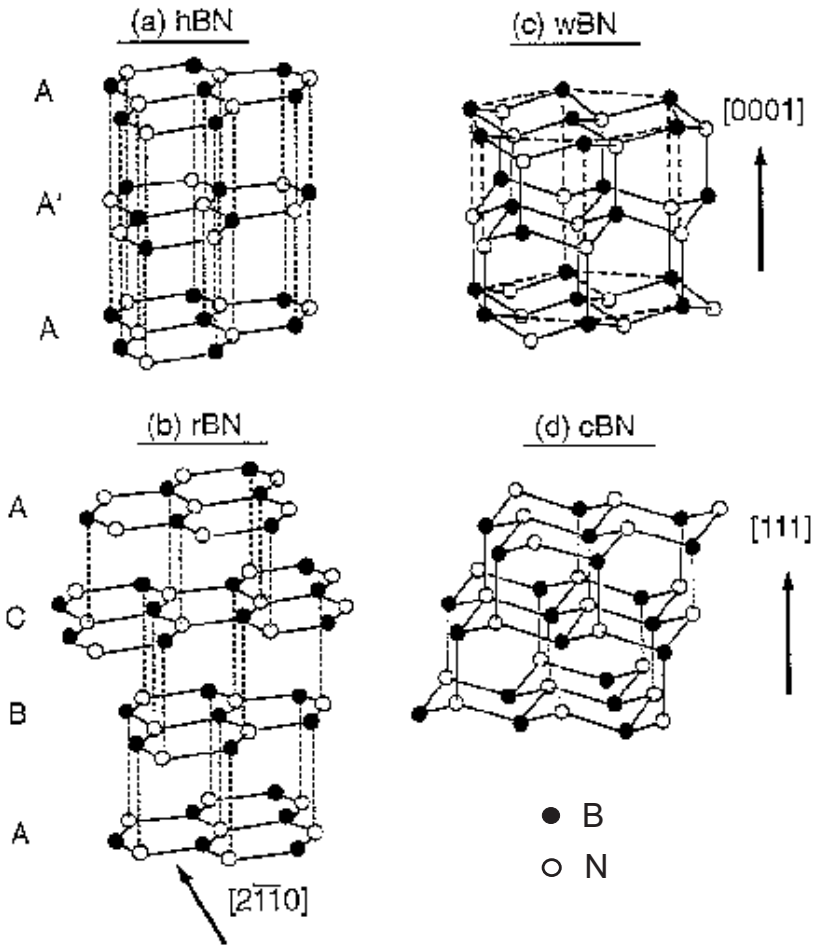

Figure 2.1: Structure of the hexagonal (hBN), cubic (cBN), rhombohedral (rBN), and wurtzitic (wBN) boron nitride modifications [30]

Table 2.1: Structural parameters of the boron nitride phases (Data are taken from [30] and references therein)

Phase	a(Å)	c(Å)	Space group	Reference
hBN	2.3043	6.6562	$P6_3mmc$ (195)	[31]
rBN	2.5042	9.99	R3m (160)	[32]
cBN	3.6153		$F\bar{4}3m$ (216)	[3, 33]
wBN	2.5505	4.210	$P6_3mc$ (186)	[33]

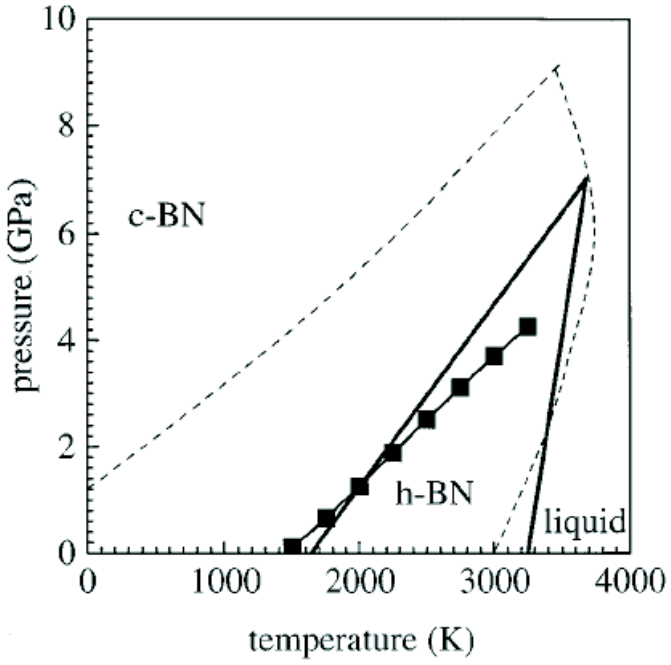

Figure 2.2: Phase stabilities in the BN system: the black dots are calculated by Albe [36] and compared to the calculation of Solozhenko (solid line)[35] and the data of Corrigan and Bundy (dashed line) [34]

2.2 cBN thin films

2.2.1 Parameters for cBN synthesis

In thin film growth a number of parameters limit the window for the fabrication of the cubic BN phase. In any case low energy ion bombardment of the film is required. The degree of ion bombardment can be generally controlled by four experimental parameters: a)ion energy E, b) ion mass m, c) ion flux J and d) the ratio of ions to film forming neutrals arriving at the substrate $\frac{J}{a}$. Kester et al. [38] found that the window for cBN growth can be described by the momentum of the ions transferred to the film:

$$\frac{P}{a} = \frac{J}{a}\sqrt{2mE\gamma} \tag{2.1}$$

where P is the momentum transferred to the film per incoming atom, a denotes the incoming neutral flux (number of atoms per unit area and time), m and E are the ion mass and energy, respectively. The factor γ describes the maximum energy that can be transferred in a single collision: $\gamma = \frac{4mM}{(m+M)^2}$, where M is the averaged mass of the target (i.e. film) atoms.

When more than one ion species are present $\frac{P}{a}$ is summed over each ion species i and equation 2.1 becomes:

$$\frac{P}{a} = \sum_i \left(\frac{J_i}{a}\right) \sqrt{2 m_i E_i \gamma_i} \tag{2.2}$$

In the above work the threshold momentum transfer for the growth of cBN was found to be around 200 $(\mathrm{eV} \cdot \mathrm{amu})^{1/2}$. Above 300 $(\mathrm{eV} \cdot \mathrm{amu})^{1/2}$ the authors observed no net film growth due to total resputtering. Mirkarimi et al. [39] investigated cBN growth by pulsed laser deposition (PLD). The authors argumented that cBN formation scales rather with the total momentum transfer of the incident ions, described by eq. 2.3, than with the maximum momentum that can be transferred in a single collision, as described in eq. 2.2, since for ion energies larger than 100 eV a single collision can not be assumed anymore (see section 5).

$$\frac{P}{a} = \sum_i \left(\frac{J_i}{a}\right) \sqrt{2 m_i E_i}. \tag{2.3}$$

In a recent literature review by Kulisch et al. [40] parameter spaces for cBN nucleation that were experimentally determined by a large number of groups are compiled. Out of this review, the cBN threshold data with respect to ion energy and ion/B-atom flux ratio F are given in figure 2.3. The different symbols of the data points stand for the different experimental groups (for detailed references see [40]), and the solid lines label $\mathrm{P_K}$ and $\mathrm{P_M}$ are the theoretical momentum transfer thresholds of Kester et al. [38] and Mirkarimi et al. [39]. The resputter limit is indicated with the upper line F_r and the lower line F_{st} points out a stoichiometry limit (the stoichiometry condition is discussed below).

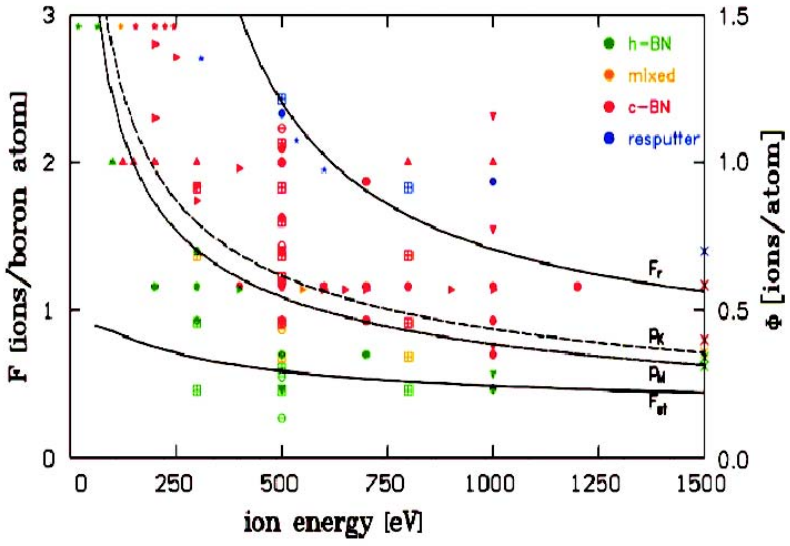

Figure 2.3: Parameter windows regarding ion energy and ion to neutral flux ratio for the deposition of cubic and hexagonal BN films obtained by different experimental groups as indicated by different data symbols (for detailed references see [40]). $\mathrm{P_K}$ and $\mathrm{P_M}$ are the theoretical momentum transfer thresholds given in [38] and [39], resp.. $F_r$and F_{st} indicate the resputter limit and a stoichiometry limit, resp.. The graph is taken from [40].

Besides the momentum transfer limit also a lower energy threshold exists for the formation of cBN [29]. In mass selected ion beam assisted deposition (MSIBAD) experiments, where boron and nitrogen both arrive as energetic ions, the lower energy threshold was determined to be 125 eV [41]. Typically the ion energies range from few hundred eV up to 1 keV.

It is generally observed that different ion bombardment thresholds exist for the nucleation and the growth of cBN ([40] and references therein). Once cBN has nucleated, the lower energy threshold for the growth of cBN is between 50 and 75 eV [42]. Since in the MSIBAD of cBN by B^+ and N^+ the resputter limit is not reached, the authors could perform also growth experiments at very high energies and found that cBN grows as well at ion energies of 15 and 20 keV for B^+ and N^+, resp. [42]. The growth under these extreme conditions should take place well below the surface (20-50 nm), and the mechanism is under discussion. The main goal of reducing the ion energy, ion/neutral arrival rate or the Ar^+/N_2^+ ratio after the cBN nucleation is the reduction of intrinsic stress and will be discussed in more detail in section 2.3.

Other parameters limiting the cBN nucleation and growth window include the substrate temperature, stoichiometry and the presence of other elements (alloying elements or contaminations). The temperature appears to affect only the nucleation of cBN. A lower temperature of 100° to 120° C is required for the nucleation process [43], whereas once nucleated cBN can be grown at room temperature [44]. Panayiotatos et al. [45] reported that for deposition at room temperature an homogeneous, amorphous sp^3 bonded material is produced that does not show the typical layered structure. For the nucleation and growth of cBN, a boron to nitrogen ratio of 1 has to be maintained [46, 47]. Even a small deviation of this stoichiometry condition leads to sp^2 bonded material. Also the presence of ~ 5 at% of other elements deliberately added or by contaminants inhibits cBN growth, e.g. [48, 49].

2.2.2 Nucleation models

Although meanwhile cBN films can be produced with a large number of different processes, the actual mechanism of the cBN nucleation is not yet fully understood. Different models have been developed to describe the cBN growth. Some of the models, like stress induced nucleation of cBN [50] and preferentially sputtering of sp^2 bonds [51] were not in agreement with experimental results [8, 52], and are therefore not described here in further detail.

The subplantation model [53] and the cylindrical thermal spike model [54] were both developed for the deposition of amorphous tetrahedrally bonded carbon (ta-C) films and adopted for cBN growth. Both models describe a subsurface growth process.

In the subplantation model, the sp^3 bond fraction is related to a local density increase due to interstitials below the surface. These interstitials can be formed either by direct penetration of an energetic ion or by knock on implantation of a surface atom during a collision with an energetic ion. A part of the interstitials is relaxed by diffusion to the surface during the thermal spike that follows the ion impact (see chapter 5).

On the other hand, Hofsäss et al. [54] described the formation of sp^3 bonds to take place in a volume where the excess ion energy is dissipated in thermal lattice vibrations,

the thermal spike. Assuming an activation energy of 3 eV [55] the number n_T of rearranged atoms is calculated and compared to the total number of n_S atoms in the spike volume. When the spike volume is quenched, the material solidifies in a phase according to the local density and bonding state. If the ratio of $n_T/n_S > 1$, the conditions are given for the formation of sp^3 bonds. This process occurs in the range of 10^{-12}s. The model predicts a lower and an upper energy limit for the cBN growth. The lower limit could be well confirmed with experimental data [42]. However, this group has shown recently that cBN growth takes place even at ion energies of 20 keV, which is clearly out of the limit of the thermal spike model. It was therefore suggested that different growth mechanisms may be involved in the different ion energy ranges.

2.2.3 Deposition methods

The deposition of cBN films is possible with a number of physical and chemical vapour deposition (PVD and CVD) techniques. All of them have in common that they are non equilibrium processes and that they employ ion bombardment of the film surface. The source of ions can be either an ion gun, e.g. a Kaufman ion source, or the ions are extracted via a substrate voltage from a plasma. Most common is the mixture of Ar and N_2 ions. But also Ne [56], Kr, and Xe ions [38, 39, 57] have been used. In most of the cases nitrogen is delivered as ionized species to the substrate. The film constituting boron is either physically evaporated or provided in form of volatile precursor compounds. Ion beam assisted deposition (IBAD), Pulsed laser deposition (PLD), and plasma assisted deposition (PAD) are described in the following to more detail.

Ion beam assisted deposition (IBAD) was one of the first successful techniques to synthesize nearly phase-pure cBN films [58]. In figure 2.2.3 the principle setup of such a system is shown. Here the source for the film forming boron atoms is an electron beam evaporator that is fed with grains of elemental boron. Using two electron beam evaporators with different source materials, also ternary compounds with a controlled stoichiometry can be synthesized [59]. A Kaufman-type ion source delivers Ar and N_2 ions to the growing films surface. Alternatively, as shown in figure 2.2.3, it is also possible to sputter a boron target by a second Kaufman ion source to provide the film forming boron atoms [60]. Since the ion and neutral fluxes and the energies of the ions can be controlled separately and independently, IBAD has been a widely used method to investigate the parameter space for cBN nucleation and growth in thin film deposition (e.g. [61, 62], more reference can be found in [30] and [40]).

A modification of IBAD is given by the mass selected IBAD (MSIBAD). Instead of evaporating or sputtering boron and bombarding the film with Ar and N_2 ions, here the film is deposited from magnetically mass separated $^{11}B^+$ and $^{14}N^+$ [41]. With this technique the cBN nucleation and growth was investigated in the energy range from 20 eV to 30 keV (see above) [41, 42].

Although IBAD is a very good tool for the study of the fundamental processes of the cBN growth, it has some drawbacks which inhibit any applicative upscaling of the process. These are mainly the very low growth rate, typically 0.1 Å/s, and the instability of the boron evaporation rate during long time deposition [8].

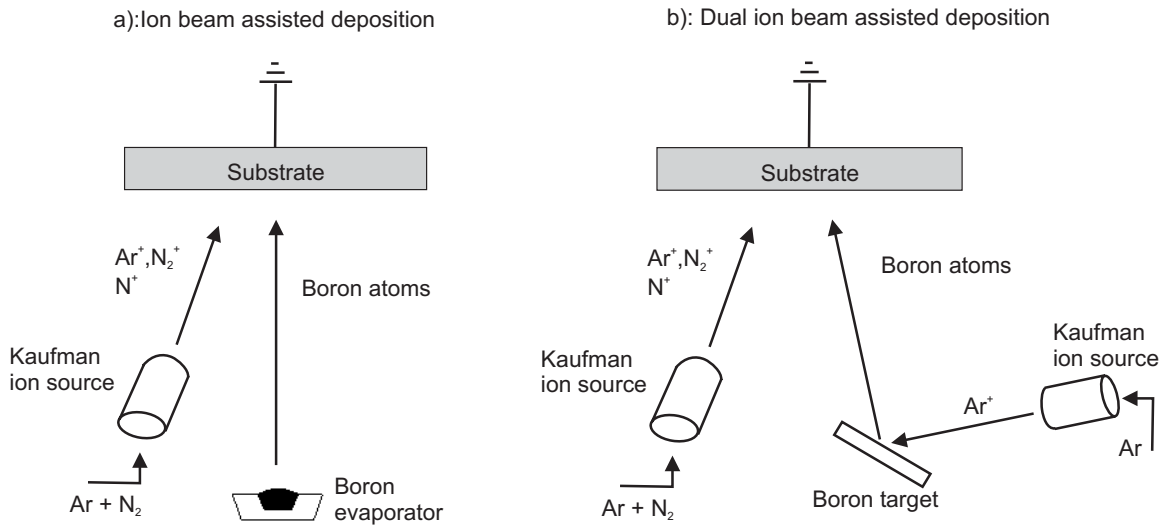

Figure 2.4: a):Schematic view of an ion beam assisted deposition using an electron beam evaporator and a Kaufman ion gun, b): Schematic view of a dual ion beam assisted deposition with a second Kaufman ion source sputtering a boron target

In **Pulsed laser deposition** (or pulsed laser ablation), a boron nitride target is ablated in N_2/Ar atmosphere with a powerful laser, e.g. an KrF excimer laser [57, 63]. In order to initiate nucleation of the cubic phase the film surface has to be bombarded additionally with ions of some 100 eV energy. With this method very high growth rates can be obtained. However, macroparticle incorporation is a serious problem, since each particulate from the ablation target incorporated into the film disrupts the cBN growth. A mechanical chopper or a bending magnetic field can be used to filter the macroparticles from the ablation plume. Naturally, the growth rate is decreased by such means.

Plasma assisted deposition techniques like magnetron sputtering, diode sputtering, and plasma assisted chemical vapour deposition (PACVD)[1] are as well able to produce cBN films if a negative bias voltage is applied to the substrate. Usually PAD gives much higher and more stable growth rates than IBAD. Additionally large areas can be coated homogeneously, and the process can be scaled up more easily.

One of the most commonly used PAD methods is magnetron sputtering (MS). The principles of MS are described in more detail in section 4.1. For the synthesis of boron nitride films, either a metallic boron [15, 16, 64, 65] or a ceramic boron nitride target are used [65, 66]. With a non-conducting hBN target the discharge has to be operated with an r.f. voltage. Although the deposition rates in r.f. discharges are generally lower than in dc discharges, higher cBN contents in the films were obtained with r.f. sputtering [15, 67]. Boron targets can be sputtered in a dc discharge when they are heated to about 800°C and the conductivity is sufficient. With the presence of sufficient nitrogen in the discharge, high

[1] PACVD is included here since the "chemistry" is restricted to the dissociation of the B and N precursors. The cBN growth process is comparable to plasma assisted PVD. When the precursors contain fluorine, the situation is different as will be described in the text.

quality cBN films can be produced also by using conducting B_4C targets in dc mode [26]. By reducing the nitrogen content in the plasma also ternary BCN films can be deposited [23, 68]. Up to now the ternary BCN films are all sp^2 bonded although a ternary sp^3 bonded BC_2N compound theoretically exists.

Unlike in chemical vapour deposition (CVD) of Diamond, the chemical route to deposit cBN films requires the assistance of ion bombardment. The process is then called **plasma assisted CVD** . Either an micro wave (2.45 GHz) or an r.f. (13.56 MHz) plasma is commonly used. The list of precursors in the literature is quite extensive. Some of these, like the widely used diborane (B_2H_6), [69, 70] are toxic. Other precursors are e.g. trimethylborazine ($B_3N_3H_2(CH_3)_3$) [71] or other organic compounds like borane dimethylamine [72]. By the introduction of fluorine in the PACVD process, recently, the deposition of several μm thick cBN films was achieved. In references [73] and [74] the deposition of cBN films with a DC plasma jet operated with an $Ar - N_2 - BF_3 - H_2$ gas mixture is described. Alternatively, an electron cyclotron resonance (ECR) plasma was used with an $Ar - He - N_2 - BF_3 - H_2$ gas mixture [75], which is more cost efficient and is capable of coating larger areas. It is believed that fluorine etches preferentially the sp^2 bonds and therefore leads to a very high sp^3 phase purity of the films. Hydrogen has to be added to the process to bond the surplus fluorine [76]. The films produced with fluorine-CVD exhibit a relative low amount of compressive stress, around -1 to -2 GPa [77]. This is most likely a result of the very high deposition temperatures that exceed 900°C, where stress is released in the film but also plastic deformation of the silicon substrate and in consequence stress relaxation occurs. The disadvantages of this process are on one hand the use the toxic BF_3 and on the other hand the very high temperatures that are required for the cBN growth, which are not practicable for tool coating.

2.2.4 The layer structure of cBN films

On all of the most commonly used substrate materials for cBN thin film deposition (Si, WC, Steel and TiN), the cubic phase can not be nucleated heteroepitaxially due to the large lattice mismatch and differences in bonding and ionicity. One exception to this rule is the heteroepitaxial deposition of cBN on CVD diamond substrates [10]. But in general the films have a very characteristic layered structure that was characterized by a large number of techniques (e.g. FTIR, ERD, TEM, in situ stress measurement). A typical TEM cross section image of the layer sequence of a BN thin film is shown in figure 2.5 (taken from [69]).

On Si substrates, the films exhibit the following layer sequence: 1. A thin amorphous layer at the substrate interface, 2. a layer of turbostratic BN, 3. the cBN nucleation zone, 4. the actual cBN layer.

The 2-5 nm wide amorphous layer is often described as amorphous boron or boron nitride (aBN). With in situ ellipsometry it could be shown, however, to be mainly amorphous silicon [9]. With high lateral resolution electron energy loss spectroscopy (EELS) and energy dispersive x-ray spectroscopy (EDX) the elemental composition of this layer was investigated [78]. Here the authors found that the amorphous layer consists of native Si oxide and complex oxide layer of Si, B, and N with 10 - 20% oxygen. This layer is most likely produced

by ion mixing during the first stage of the deposition [79], since the thickness of this layer is approximately the ion range.

On this amorphous layer, a layer of turbostratic BN is formed. When the film is deposited under ion bombardment, the tBN layer is oriented with the c axis parallel to the substrate surface and the hexagonal basal planes oriented randomly around the c axis [62, 80]. When the tBN grows without ion bombardment the basal planes are oriented with the c axis perpendicular to the surface. The origin of this preferred orientation is discussed in the literature to be either due to the minimization of the elastic strain energy (resulting in a minimization of the Gibbs free energy G) [81] or caused by plastic deformation [82, 83]. Theoretical calculations of the orientation-dependence of the strain energy are not in agreement with the experimental findings. Main reason is that the elastic tensor of the material is included in the calculations of G. Reliable data on the elastic properties of tBN thin films are not available but due to the microstructure of the films (larger lattice spacing, bending and cross-linking of planes as can be seen in fig 2.5) they should be rather different from bulk material.

Out of this textured tBN layer cBN can nucleate. The nucleation takes place in separated islands [84]. Up to the coalescence of the islands, both cBN and tBN crystallites are growing. When the coalescence is fully accomplished, almost pure cBN is growing further with columnar structure [85]. It is believed that the oriented tBN planes serve as growth template for the cBN (111) planes [86] in such a way that three of the cBN (111) planes match with two of the tBN (0002) planes. Then the relative lattice spacings of 2.09 Å and 3.33 Å for cBN and tBN, resp., approach a 2:3 ratio. This model is confirmed by high resolution TEM (HRTEM) by Weissmantel et al. [87] as can be seen in fig 2.6. An earlier model according to which the cBN nucleates directly by a stress induced compression of the tBN in [0002] direction appears to be less valid, since the stacking sequence in hBN and cBN is different (and the stacking sequence in tBN might be completely random).

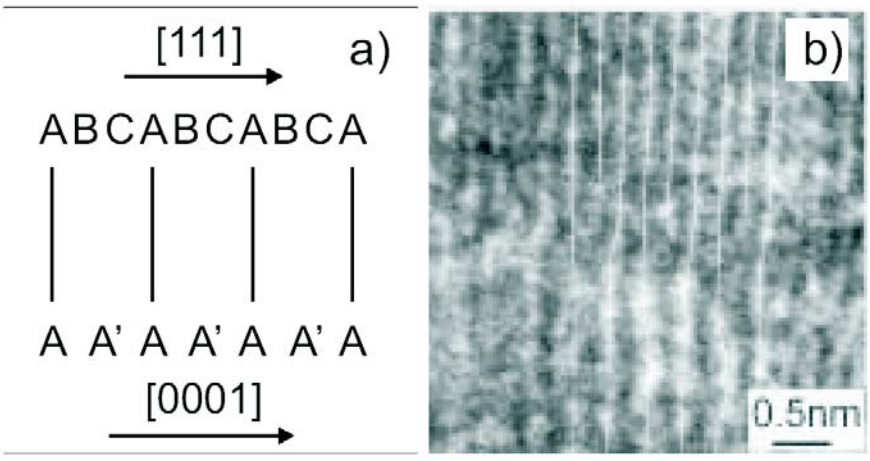

Figure 2.6: TEM cross sectional image of the hBN/cBN interface showing the 2:3 matching of the tBN (0002) planes with the cBN (111) planes [87]

The cubic crystallites are generally very small (10-30 nm) and with at least one of the

[111] directions parallel to the surface (an in-plane [111] texture) [86]. In some cases also a [110] out-of-plane texture with two [111] directions parallel to the surface is observed [88].

With surface sensitive techniques (e.g. Auger electron spectroscopy or electron energy loss spectroscopy but also HRTEM) very often a thin sp^2 bonded surface layer is observed (e.g. [89]). The thickness is usually not more than 1-2 nm. Fukarek could show with in situ ellipsometry that this sp^2 surface layer is present throughout the cBN growth with IBAD [9]. This leads to the conclusion that the formation of sp^3 bonds takes place below the surface within the ion range, which is supported by the subplantation model [53] and the thermal spike model [54].

2.3 Strategies for the deposition of thick cBN films

In the Literature several approaches are known to realize the deposition of thick ($>1\mu$m) cBN films at moderate temperatures. On one hand the reduction of the high intrinsic stress was pursued and on the other hand the adhesion of the film to the substrate was improved. In the following the different routes are discussed. A third route is to really relax the stress in the layers. This has been achieved by energetic ion implantation and the principles and outcomes are discussed in section 3.3.

Optimization of process parameters To reduce the stress in the cBN films, one way is the optimization of the process parameters, in particular the ion energy (see the Davis model p. 20). The fact that the ion energy can be reduced after the cBN nucleation [30] has been used in a number of publications to deposit layers at a reduced level of compressive stress [21, 27, 90–92]. Also the deposition with an increased ion energy (up to 1000 eV) was discussed by Kulisch et al. [71]. Using this high ion energy the deposition is operated very close to the resputter limit and an efficient growth rate can not be achieved. In order to grow cBN films with low stress, the following deposition parameters can be changed after cBN nucleation:

- Reduction of the ion mass, i.e. the reduction of the argon content of the growth assisting ions [52, 71]
- Decrease of the ion to neutral ratio [52, 93]
- Decrease of the substrate temperature after cBN nucleation [29] as well as post deposition annealing [21, 94] are discussed.

Addition of alloying elements In several publications it could be shown that the addition of alloying elements like C [26], Si [95], and Al [25] lead to reduced stress in the cBN films. However it was found for all alloying elements as well as for unintentional contaminations that the presence of more than ~ 5 at% of additional elements in the film completely inhibits a cBN nucleation. Also the achieved stress relaxation was not sufficient to produce μm thick films.

Adhesion layers and multilayers In the following paragraph those works are summarized, which deal with the improvement of the adhesion mainly by employing intermediate layers.

- BCN buffer layers with a gradually decreasing C content on Si and WC substrates proved to have sufficient adhesion strength to sustain several μm thick cBN layers on top [23]. Recently such a layer system was deposited on cutting tools and first tests of high speed cutting tools showed promising results [96].
- In several works the adhesion could be improved due to the deposition of a thick hBN interlayer either on Si substrates [97, 98], or on WC substrates [63]
- Boron-rich buffer layers were used to enable the deposition of adherent cBN films on Si, WC, and Al_2O_3 substrates [99, 100].
- The possibility of heteroepitaxial growth of cBN was demonstrated by Feldermann [101] at al. on AlN and by Zhang et al. on CVD Diamond [10]. In the latter however, this was achieved only at significantly elevated temperatures (900°C).
- Lee et al. [24] could deposit 0.4 μm thick cBN layers on top of an AlN buffer layer, however with an hBN interlayer. Further on in this work AlN/BN multilayers were produced. Since the cBN has to nucleate from the hBN in each multi layer period, a minimum period thickness of 20 nm was necessary to grow cBN containing multi layers.
- Also titanium nitride was used as an adhesion layer [102] and in TiN/BN multi layers. In these multi layers the boron nitride was fully hexagonal, since the minimum thickness needed for cBN nucleation was not reached.

Summarizing these results, it becomes clear that the different buffer layers provide a structure that is able to compensate or to bear the high stress of the film, but the stress itself is not reduced. Due to the fact that cBN cannot be grown heteroepitaxially (in most of the cases), multi layer deposition always will include some hexagonal boron nitride as a seed layer for the cBN nucleation.

3 Stress in thin films

The state of stress of a material is generally described by the stress tensor, which contains the directional stress components of a differential volume [103]:

$$s_{ij} = \begin{pmatrix} s_{11} & s_{12} & s_{13} \\ s_{21} & s_{22} & s_{23} \\ s_{31} & s_{32} & s_{33} \end{pmatrix} \tag{3.1}$$

The diagonal elements denote the normal contributions of the stress in a cartesian coordinate system, and the off-diagonal elements denote the shear stresses.

A biaxial state of stress is defined by the components $s_{11}, s_{22}, s_{12} = s_{21}$ and $s_{33} = s_{13} = s_{31} = s_{23} = s_{32} = 0$.

Any state of stress can be transformed to be aligned along its principal directions, where the shear components vanish. The principal stresses are denoted S_i.

In a thin film, where the film thickness is much smaller than the substrate thickness $d_f \ll d_s$ and the lateral dimensions are much larger than the total thickness of film and substrate, the state of stress is biaxial and the stress tensor can be written as

$$S_i = \begin{pmatrix} S_1 & 0 & 0 \\ 0 & S_2 & 0 \\ 0 & 0 & 0 \end{pmatrix}, \tag{3.2}$$

where S_1 and S_2 are the principal stresses in the plane of the film and S_3, which is the principal component normal to the plane is zero. Additionally, in-plane elastic isotropy is assumed in a thin film so that $S_1 = S_2$.

A strain ϵ that is imposed to the film (e.g. due to the introduction of defects, change of the temperature or a phase transformation) will lead, according to Hooks law, to a stress S that is:

$$S = S_1 = S_2 = Y\epsilon \tag{3.3}$$

where Y (biaxial modulus) is given by $Y = E/(1-\nu)$. E and ν are the Youngs modulus and the Poisson ratio of the film. Note that in the following S is used to describe a biaxial film stress that is averaged over the film thickness and $\sigma = \sigma(d_f)$ denotes the instantaneous biaxial stress at a certain depth d_f in the film.

In a thin film that is attached to the substrate, any strain and in consequence stress in the film, will lead to a bending of the substrate and the film. This is schematically shown in figure 3.1, where the strained film is symbolized by a elongated or compressed spring. The relations between the stress in the film and the bending radius R of the film/substrate compound are given below.

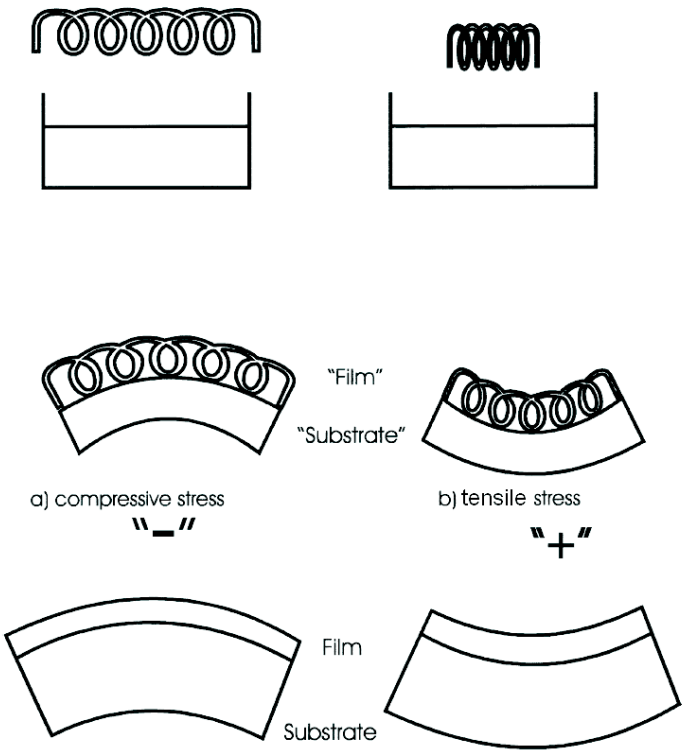

Figure 3.1: Schematic illustration of the bending of a film/substrate compound induced by biaxial stress in the thin film (picture taken from [104])

For an isotropic film and substrate, the total force imposed by the film on the substrate is an integral of the stress over a given cross sectional area:

$$F = \int_0^{d_f} \sigma(d_f) W dd_f, \tag{3.4}$$

where d_f is the thickness of the film and W the width of the film and substrate. If the stress is isotropically distributed throughout the film thickness, the film force can be expressed as $F = S_f d_f W$.

The steady state is reached when the moments of force of the substrate $M_s = Y_s W d_s^3/12R$ (with Y_s being the biaxial elastic modulus of the substrate, d_s the thickness of the substrate and R the bending radius) and of the film $M_f = S d_f W(d_s/2)$ are equal. Then the global stress becomes

$$S = \frac{Y_s d_s^2}{6 R d_f} \tag{3.5}$$

For silicon substrates $Y_s = 180GPa$ [105]. Positive values of S denote tensile stress, where negative values are defined as compressive stress. Equation 3.5 is known as the Stoney formula [106].

The film force per unit width (FPUW) on the substrate surface can be calculated by

$$FPUW = S d_f = \frac{Y_s d_s^2}{6R} \tag{3.6}$$

Equation 3.6 is valid for $d_f \ll d_s$, then the FPUW is proportional to the substrate curvature $1/R$.

If S varies through the film thickness (e.g. due to parameter changes during deposition or a phase transition), the instantaneous stress $\sigma(d_f)$ has to be considered. If no subsurface stress relaxation occurs (e.g. thermal relaxation or due to ion bombardment), then at a given instantaneous film thickness during deposition, σ is defined as the first derivative of the force per unit width with respect to the film thickness:

$$\sigma(d_f) = \left.\frac{\partial(FPUW)}{\partial(d_f)}\right|_{d_f} = \left.\frac{\partial(\frac{Y_s d_s^2}{6R})}{\partial d_f}\right|_{d_f} \tag{3.7}$$

From equation 3.7 it becomes obvious that for thin films with an inhomogeneous distribution of the stress, e.g. tBN/cBN layered films, to obtain the instantaneous stress, the evolution of both, bending radius of the substrate and film thickness has to be measured during the deposition. The experimental details are discussed in section 7.1.1.

3.1 Origin of stresses in thin films

Intrinsic stress of thin films can be produced by a number of processes and various types of defects. In epitaxial film growth misfit stress arises when the lattice spacings of the film and substrate material are different. The incorporation of residual gas atoms and non reactive process gases can lead to compressive stress. However, in the case of magnetron sputter deposition of metal films Thornton et al. found that the contribution of the noble gas incorporation to the total film stress is rather small [107, 108]. Other examples of defects that lead to stress are low angle grain boundaries, vacancies, and self atoms or impurities built in on interstitial sites. Recrystallization and phase transformation can lead to large volume changes and in consequence to high stress.

Thermal stresses are extrinsic and arise from differences in thermal expansion coefficients of the film (α_f) and the substrate (α_s). When changing the temperature from T_1 to T_2, e.g. from deposition temperature to ambient temperature, a thermal stress σ_T is produced, given by

$$\sigma_T = \frac{E_f}{1-\nu_f}(\alpha_f - \alpha_s)(T_1 - T_2). \tag{3.8}$$

E_f and ν_f are the Youngs modulus and the Poisson ratio of the film respectively. For cBN films deposited on silicon substrates, the thermal stress that arises during cooling from deposition to ambient temperature is tensile [8]. For cBN films on metal or hard metal substrates, where the thermal expansion coefficient is larger than that of the film, the thermal stress induce by cooling becomes compressive and adds additionally to the intrinsic compressive stress. Also for this reason, the deposition of cBN on metallic or hard metal substrates should be carried out at moderate temperatures.

Stress can also be induced by energetic particle bombardment of the film during deposition. This is discussed detailed in the next section.

3.2 Ion-induced stress in thin films

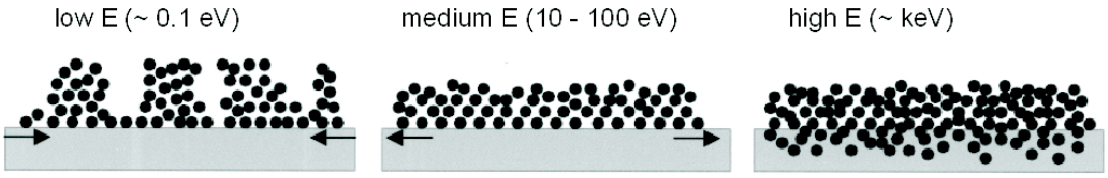

Figure 3.2: Thin film microstructure resulting from ion bombardment in different energy regimes (picture taken from [109])

In the 1970s to 1980s Thornton and Hoffman [107, 108] identified energetic particles as the origin of intrinsic compressive stress in thin films. In this early work, magnetron sputtering of metal films without any additional substrate bias was investigated and hence the energetic particles were neutralized inert gas atoms backscattered from the sputtering target (energy up to several 100s eV). Thornton and Hoffman explained the stress to be a result of recoil implantation of film surface atoms into some nm depth by the impact of the energetic particles (often referred to as 'ion peening', see also section 5). This process leads to a local densification and hence to compressive stress, as is schematically shown in figure 3.2. The principle of stress generation can be applied to all sorts of deposition processes where energetic neutrals or ions are involved like low pressure plasma assisted deposition with additional substrate bias, IBAD, cathodic arc evaporation, or pulsed laser ablation.

In the early 1990's Davis developed a simple theoretical model for cathodic arc deposition that relates the stress in thin films with the energy of incident ions [110]. Analog to the subplantation model for the formation of sp^3 bonds in diamond-like amorphous carbon (DLC) films by Robertson [111], in the model of Davis the stress results from a balance between recoil implantation and relaxation due to defect annealing in thermal spikes and is expressed by

$$\sigma(E_{ion}) \propto \frac{Y}{1-\nu}\frac{E^{1/2}}{a/J + 0.016\rho(E/E_0)^{5/3}}, \tag{3.9}$$

where Y is the in-plane Young's modulus, ν is Poisson's ratio, a is the rate of film atoms deposited per unit area, J is the flux of energetic ions to the film surface, ρ is a materials dependent parameter in the order of unity, E is the energy of the incident ions. E_0 is the excitation energy for atoms in metastable positions to move to the surface, which is assumed to be in the order of 10 eV [112]. A typical evolution of stress in a thin film with increasing ion/particle energy is shown in figure 3.3. For lower ion energies, the formation of defects prevail, and hence the stress is increasing with the ion energy. Depending on the material and the deposition conditions a maximum of compressive stress is usually found in the range of 100 - 200 eV. For higher ion energies the compressive stress decreases, since the removal of atoms on defect positions requires less energy than the formation of a new defect from an atom on a lattice position.

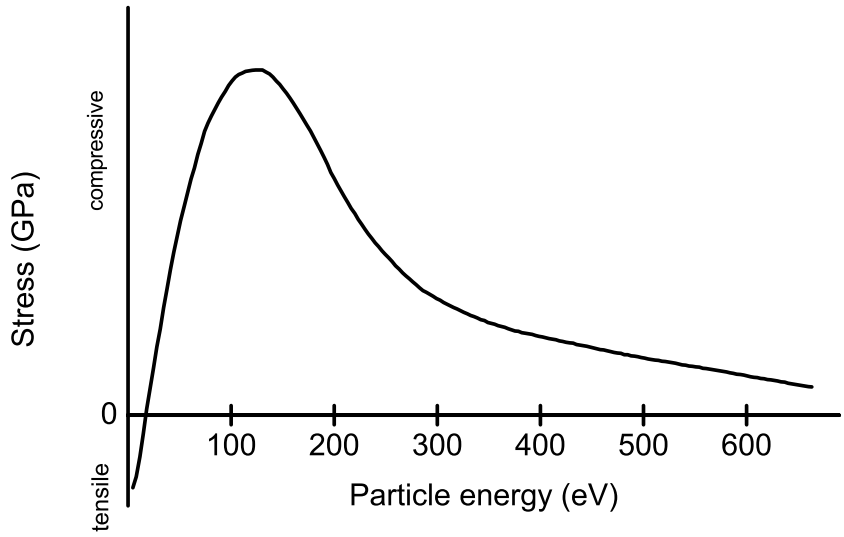

Figure 3.3: Dependence of the intrinsic stress in a thin film upon the energy of the incident particles.

From results of molecular dynamic simulations of a film deposition by carbon ions with energies between 1 and 100 eV, Marks et al. [113] proposed that in this case stress is produced by ion impact-induced compression of the surface bonds rather than subplantation or recoil implantation. As a result, a distribution of bond stresses was obtained, which gives an average compressive state of stress.

The evolution of stress in magnetron sputtered films could differ from the Davis model due to the presence of noble gas ions that bombard the film but are not incorporated into the crystalline structure. Kazansky et al. showed that for a substrate bias voltage of -350 V a significant amount of Ar is trapped in pores in the film [114].

The prediction of stress in a film becomes more complicated if the preferred orientation

in the film changes with the ion energy or when a phase transition can be induced by the ion bombardment, as it is the case for BN films. For amorphous and homogeneous sp^3 bonded BN films that were deposited with magnetron sputtering at room temperature, Panayiotatos et al. [45] showed that the stress dependence on negative bias voltage fits very well with the theoretical predictions of the Davis model.

3.3 Reducing stress in thin films

The model of Davis [110] and the results of Marks [113] described the stress relaxation taking place at higher ion energies and below the film surface. Within the thermal spike or the collision cascades, breaking of compressed bonds below the surface is induced with a subsequent reformation of the bonds without compression. Thus, to produce films with low stress, the ion energy has to be chosen either very low or very high. However, both models describe the case when the ions are incorporated into the film structure and nobel gas ions do not play a role. In a number of deposition processes including IBAD and magnetron sputtering this is not the case: here the film is formed by low energy neutrals (0.1 - 20 eV) and ions with energies ranging from several 10s of eV up to $\sim$ 1 keV are employed to densify the film or to induce phase transformation like in cBN deposition. Most commonly Ar ions are used and for reactive nitride film growth nitrogen ions are added. The consequence of this is that at low ion energies the desired film properties are not achieved and for very high ion energies the resputter limit is reached and no efficient film growth can be achieved (e.g. reference [115]). Especially in the case of cubic boron nitride the optimum ion energy range to produce dense and purely cubic films coincide with the maximum of stress in the 'Davis curve'.

To overcome this dilemma, it is proposed here that the film growth can be separated from the stress relaxation. This means that the film is formed mainly by the deposition of low energy particles (neutrals and/or ions) and only a small fraction of the particle flux to the film consists of high energy ions. Then the film growth takes place at the surface and is accompanied by large compressive stress. The high energy ions, however, can penetrate into some depth below the surface and induce thermal spikes or collision cascades and in turn the stress is released. Sputtering is minimized since the high energy ions account for only a few percent of the deposition flux, and if the energies are chosen to be very high ($>$ 10 keV) the sputter yield is decreased as well. In practice, this has been realized in plasma assisted deposition of hard coatings other than cBN by the application of a pulsed bias voltage in the range of 1 kV up to several 10 kV to the substrate [109, 116–119].

For the deposition of cBN, the lower threshold of the ion energy is in the order of 0.1 to 0.5 keV. So a process that realizes growth and stress relaxation needs to include ions with some hundred eV as well as ions with significantly higher energy. This was up to now performed only for IBAD with additional high energy ions (35 keV - 1.1 MeV) delivered by a linear accelerator. Thereby different experimental techniques have been used:

1. In post deposition ion implantation 1.1 MeV Xe and He ions were used [11]. Due to the mean ion range of $>$ 300 nm, the ions penetrated the total film, including the hBN layer and even are implanted into the substrate. The stress was reduced by this

treatment, however for ion doses $> 5 \cdot 10^{13}$ions/cm^2 a phase transformation from cBN to hBN was observed. The authors found that the implantation induced total number of displacements per unit volume is the key parameter for stress relaxation but also for phase transition.

2. In a sequential process of film growth, implantation of 300 keV Ar ions, and annealing 1 μm thick BN films with a very high cBN content could be produced [12]. The growth sequences were chosen to deposit 180 nm cBN to match the mean projected range of the ions. in this way, the substrate was not irradiated.

3. Fitz et al. [13] demonstrated for the first time a simultaneous process of film growth by IBAD and irradiation of the growing film with 35 keV N^+ or 70 keV Ar^+ ions. The hBN layer and about 40 nm cBN were deposited without additional ion implantation, in order to prevent the ions from penetrating the hBN/ cBN interface. By in situ stress measurement, the stress relaxation in cBN from > -10 GPa down to -1.3 GPa due to the ion implantation could be quantitatively measured for the first time in real time during deposition.

The experimental set up for the latter procedure is displayed in figure 3.4 showing a boron evaporator, a Kaufman ion source, and a Danfysik 200 kV implanter, which delivers 35 keV N^+ ions.

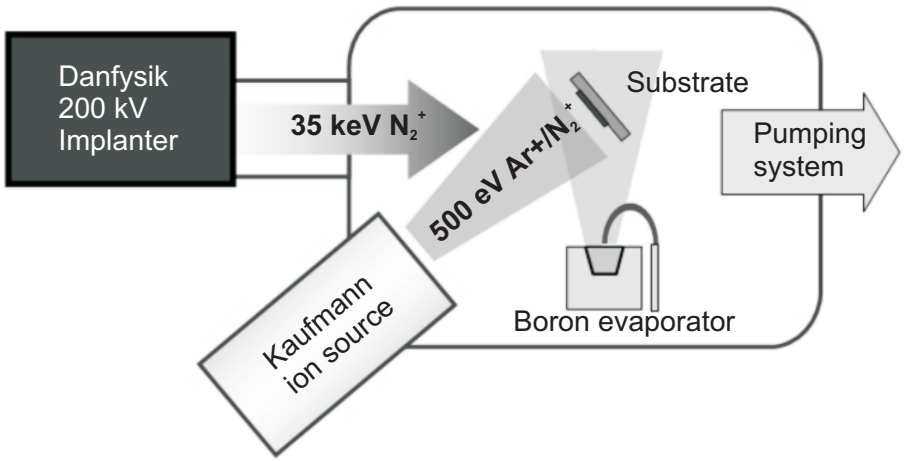

Figure 3.4: Experimental set up for the IBA deposition of low stress cBN films with simultaneous medium energy ion bombardment including a boron evaporator, a Kaufman ion source and Danfysik 200 kV implanter, which delivers 35 keV N^+ ions.

Up to now it was not possible to realize the range of ion energies in a plasma assisted PVD process, since no suitable power supply for the substrate bias was available. In the present work this has been realized and the experimental details are described in chapter 4.2 and the results are presented in chapter 8.

4 Film deposition

4.1 Magnetron sputter deposition

In this work magnetron sputtering was used for the deposition of the cBN films since it provides higher and more stable growth rates than IBAD and is a widely used method for the industrial deposition of many different functional thin films including hard coatings on tools. To be able to estimate the fluxes of sputtered particles to the substrate as well as ion fluxes and the ion energy distribution a detailed investigation of the deposition process in the magnetron system was performed and is summarized in section 6.

The most common method of PAD of cBN films is unbalanced magnetron sputtering. In a planar magnetron like shown in figure 4.1, a sputter target, that serves as cathode, is placed above a configuration of permanent magnets that produce a magnetic field over the target surface. In a "balanced" magnetic field all field lines are closed (i.e. they extend from the N pole to the S pole of the permanent magnets). In unbalanced magnetic configurations some of the magnetic field lines close on the substrate or the walls of the chamber. In operation, the electrons of the low pressure plasma are confined on a so called race track just above the target surface by the magnetic field due to the $\vec{E}$ x $\vec{B}$ drift. Therefore the electron density is increased in this area and consequently the ionization rate due to electron impact ionization of neutral gas particles is as well increased. The erosion of the target material by the ions is then very high leading to high deposition rates on the substrate. Compared to IBAD, the increase of the growth rate is however gained by the loss of separate control of neutral and ion fluxes to the substrate. In unbalanced magnetrons the high density plasma is extended towards the substrate and hence the ion flux to the substrate is increased. When insulating targets are used, the magnetron discharge has to be powered by an r.f. voltage, then also a matching network is required. Conducting targets are normally operated with a d.c voltage.

4.2 Experimental set up

The deposition chamber that was used in this work is schematically shown in figure 4.2, including the in situ ellipsometer and the in situ stress measurement (these in situ diagnostics are described more detailed in section 7.1). The reactor is evacuated with a turbo molecular pump down to 2x10^{-6} Pa. The argon and nitrogen feed gases (99.999999% and 99.99999 % purity, respectively) are introduced through a mass flow controller. If not stated else, for the deposition experiments the argon and nitrogen fluxes are set to 14 sccm and 7.5 sccm, respectively. For the plasma diagnostics, the Ar/(Ar + N_2) ratio was varied between 0 and 1.

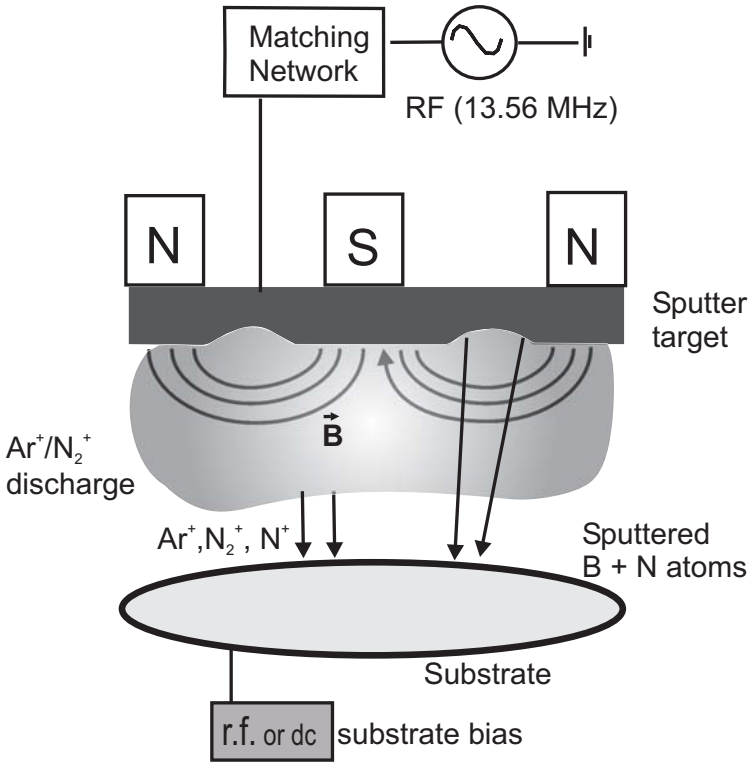

Figure 4.1: Schematic view of magnetron sputter deposition

During deposition a gate valve between the reactor and the turbo molecular pump is used to adjust the total pressure. For Langmuir probe measurements (see section 6.1) the working gas pressure was varied between 0.1 to 0.5 Pa, during deposition it was always 0.1 Pa. The sputtering system consists of an unbalanced magnetron parallel to the substrate surface at a distance of 60 mm. A 3" hBN target is sputtered in the Ar/N_2 ambient. The magnetron is capacitively powered by a 13.56 MHz radio frequency power supply. With an L-type matching network between the power supply and the discharge, the reflected power can be minimized to below a few percent. The r.f. power was scanned from 100 to 300 W in the plasma diagnostic experiments. For film deposition it was set to 250 W. All standard deposition parameter are summarized in table 4.1

The films are deposited on (001) oriented silicon substrates or on cantilever structures of 22 x 4 x 0.18 mm^3 that are etched into 45 x 30 x 0.3 mm^3 (001) silicon substrates. The substrates are clamped into a molybdenum mask of 3" diameter that is placed on the substrate holder. The mask is used to fix the cantilever and to ensure good electrical contact with the substrate holder since the substrate has to be biased. During deposition the substrate is heated to 350°C. The heater consists of a 100 W lamp positioned in the center of a parabolic mirror below the substrate, and the substrate temperature before deposition is measured ellipsometrically (see section 7.1.2).

In plasma based deposition methods like magnetron sputtering, the ion bombardment that is required for the nucleation and growth of the cubic BN phase, is provided through a bias voltage at the substrate. Since BN is insulating, either a r.f. self bias or a bipolar pulsed dc bias is required to prevent charging of the film surface during the deposition of

Table 4.1: Standard deposition parameters for the growth of cubic boron nitride films (Note that the substrate temperature is measured ellipsometrical, see section 7.1.2)

Deposition parameter	**Value**
Base pressure	$< 5 \cdot 10^{-5}$Pa
Working pressure	0.1 Pa
Ar Flow	14 sccm (65%)
N_2 Flow	7.5 sccm (35%)
R.F. power	250 W
Substrate bias	-150 V / +80 V
Substrate temperature	350 °C

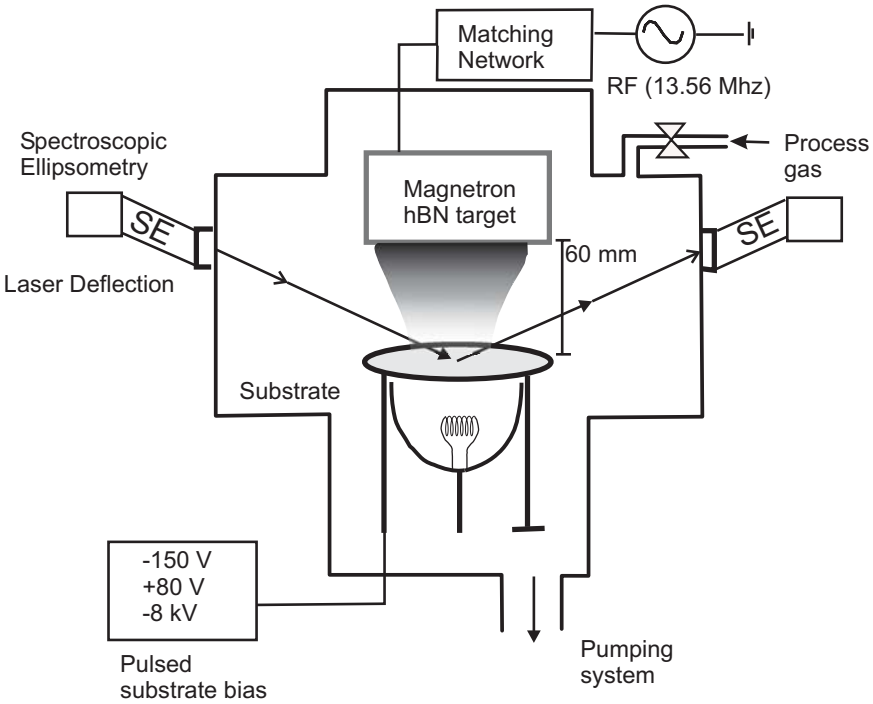

Figure 4.2: Schematic view of the magnetron system including the in situ ellipsometry and the in situ stress diagnostic.

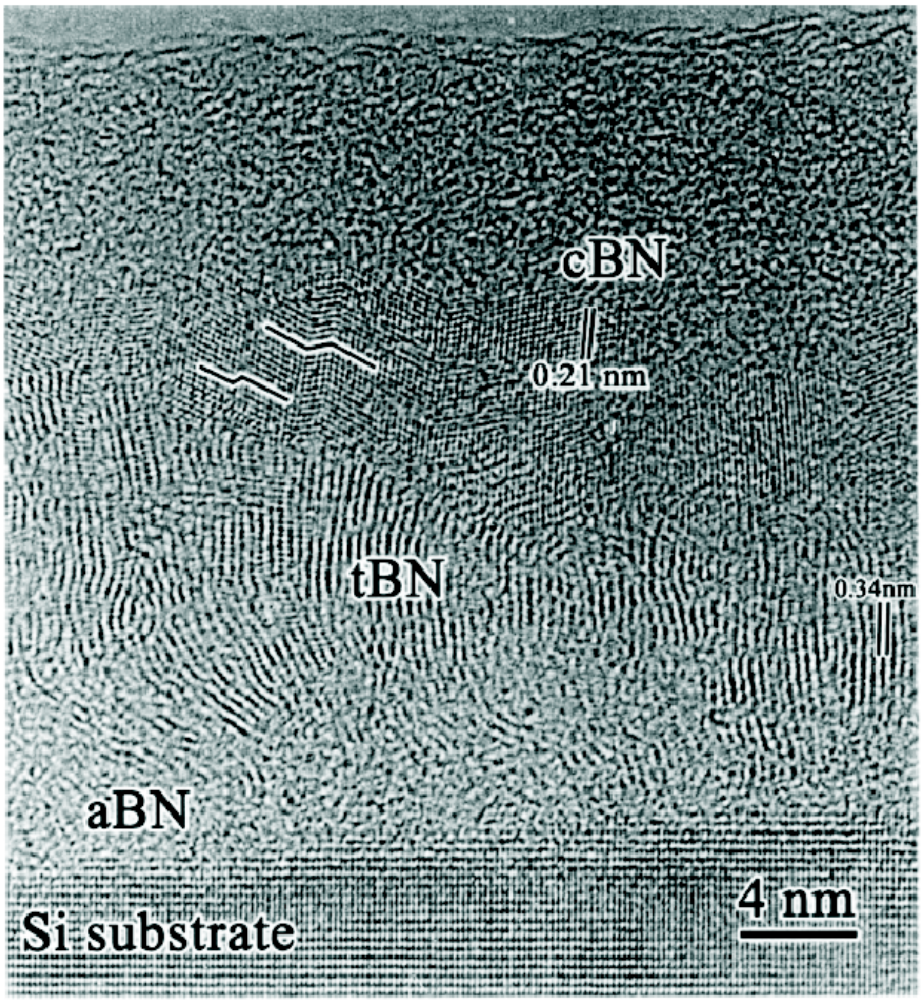

Figure 2.5: TEM cross section of the layered structure of a cubic boron nitride film consisting of an amorphous layer (aBN), a layer of turbostratic BN (tBN), a mixed region with tBN and cBN, and the cubic top layer (cBN). The figure is taken from reference [69].

thick films. In the experiments described here a bipolar pulsed dc bias is used.

The substrate bias power supply (developed by GBS Elektronik GmbH, Dresden, Germany) provides the possibility to add high voltage pulses to the bipolar pulsed low voltage dc bias. The substrate voltage sequence including high voltage pulses is schematically shown in figure 4.3 (note: the time axis is not scaled). If not stated else, the bias voltage settings for all experiments are as follows: the low voltage substrate bias that is required for cBN nucleation and growth is set to -150 V pulses of 80 μs. To discharge the surface, the low voltage pulse is followed by a short intermediate pulse of a positive voltage (+80 V for 3μs). High voltage pulses of -2 to -8 kV for 2 μs enable simultaneous stress relaxation by energetic ion bombardment. Since the negative HV pulses are followed directly by a positive discharge pulse, they are square shaped. The pulse rise time of $\sim$ 500 ns is added to the programmed pulse duration of 2 μs. In order to preserve the life time of the switches in the power supply, after each positive pulse a 5 μs brake is programmed, in which the voltage out put is zero. Varying the repetition rate of low-voltage cycles between the high voltage pulses, the ratio of high energy to low energy ions impinging on the substrate can be controlled. In this work, the 'duty cycle' is referred to the ratio of the on-times of the high energy pulses to the low energy bias and is varied between 0.3% and 1.2%, corresponding to HV pulse frequencies between 1.4 and 4.5 kHz. In this way the duty cycle is a direct measure for the flux ratio of high energy ions to low energy ions to the substrate.

The potential at the film surface does not necessarily equal the applied bias voltage. The reason herefore is the insulating character of the boron nitride film, resulting in charging of the surface and a voltage drop across the film thickness. The charging is avoided by applying a positive voltage pulses to the substrate. The discharge potential should be above the plasma potential (see section 6.1), but not too high in order to avoid excessive electron currents. In all experiments described here the discharge voltage was + 80 V. Using lower voltages, charging of the surface reduced the ion energy in such that the nucleation of cBN failed. Increasing the discharge voltage from +80 to +120 V did not show any effect on the phase composition or the film stress. Therefore it is concluded, that the film surface is completely discharged during a 3 μs pulse of +80 V.
Since boron nitride is an isolator, the film acts as a capacitor. The resulting voltage drop depends on the film thickness and the dielectric constant[1] of the film. Compared to the dimensions of the chamber, the film thickness is very small and the voltage drop across the film is negligible. In the experiments the applied substrate bias of -150 V was sufficient to sustain cBN growth up to a thickness of 900 nm (thicker films were not deposited).

Due to the shape of the cantilever and its fixation in the sample holder, the substrate temperature might be different on the cantilever tip and on the reference position. The reference spot on the frame of the structure is on three sides in good thermal and electrical contact with the substrate holder, where the cantilever itself has only on one short side contact with the sample holder. Very likely this leads to an inhomogeneous temperature distribution across the sample. Within the deposition chamber possibilities to measure the actual substrate and film temperature are limited. A thermo couple would not necessarily give the real substrate temperature and would not be able to detect an inhomogeneous temperature distribution. The temperature of the silicon substrate is therefore measured

[1] $\epsilon_\infty = 2 - 10$ [30] and references therein

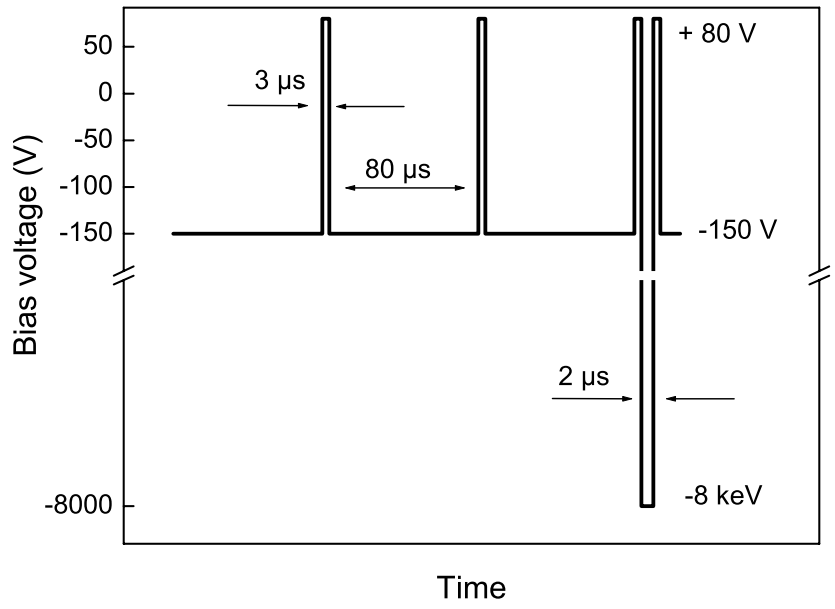

Figure 4.3: Schematic of the pulsed substrate bias voltage with typical settings

ellipsometrically by the shift of the band gap. This, however is only possible before the deposition, as soon as the silicon is covered by film material, the signature of the Si band gap can not be detected anymore. It is therefore also not possible to measure the temperature changes due to ion bombardment of the film. By a simple estimation of the heating power of the lamp and the ion flux to the substrate, it was found however that the additional heating power density due to the ion bombardment is small (0.02 W/cm^2)[2] compared to the heating power density from the lamp (1 W/cm^2).

[2]the heating power of the high energy ion bombardment was calculated assuming an time average ion flux of $\approx 1 \cdot 10^{13}$ions/cm^{2}s $= 1.6\mu$A/cm^2 and an ion energy of 8keV.

5 Ion bombardment effects

The effects of ion bombardment on a solid material can generally characterized in terms of the volume that is affected by the ion bombardment and the energy that is dissipated in this volume (for an in depth treatment of ion-solid interactions see references [120, 121]). The kinetic energy of the ion is transferred to the solid during elastic nuclear collisions and by inelastic electronic stopping processes. In the energy range considered here ($<$ 10 keV), nuclear stopping is dominant and therefore electronic stopping processes will not be considered. If the energy that is transferred during a binary collision from the incoming ion to a target[1] atom is larger than the displacement energy, the atom will be removed from its lattice position. If the transferred energy is less than the displacement energy, the target atom undergoes large amplitude vibrations and the energy is dissipated as heat (thermal spike). This thermal spike stage follows the collisional stage of the ion impact and can induce extremely high temperatures in the spike volume, which are exceeding the melting temperature. Displacement energies are typically around 25 eV and therefore during an ion impact with $E_i > 100eV$ several displacement collisions can take place (linear cascade). The displaced target atoms can receive sufficient energy to displace other target atoms in secondary collisions (collision cascade). The elastic energy transfer in a nuclear collision is given by:

$$T_n = E_0 \frac{4M_1M_2}{(M_1+M_2)^2} sin^2\left(\frac{\theta}{2}\right), \tag{5.1}$$

where E_0 is the ion energy, M_1 and M_2 are the projectile and target masses, resp., and θ is the scattering angle.

When the primary ion energy has been spent in collisions, the ion will finally come to rest somewhere in the solid. The distance between the surface and the settled ion is called projected range. The depth distribution of projected ion ranges can be approximated by a Gaussian distribution function and the mean projected range R_p is the most probable depth in the solid for the ion to stop, given by the center of the Gaussian. The displacement of lattice atoms, and the incorporation of the bombarding ion can lead to a number of defects like vacancies, interstitials, selfinterstitials and substitutional impurities. Also sputtering has to be considered, where the bombarded surface is eroded due to collisions between the incoming ions and the atoms in the near surface layer. The opposite effect is also known in thin film growth: an ion/atom collision occurring in the near surface region results in the implantation of the surface atom into regions below the surface is referred to as ion-peening,

[1] In the discussion of ion-solid interactions, the solid atoms are usually referred to as target. This should not be confused with the magnetron sputter target.

knock-on implantation, recoil implantation, or subplantation. This process is responsible for densification of the films and in turn can lead to phase transformation [53, 111] and/or high compressive stress [110].

Computer simulations like the TRIM [122] code that is based on the binary collision approximation enable the experimentator to estimate the ion ranges and predict the degree of radiation damage. Since in TRIM a static substrate is assumed, it can be used only for implantation in the range of low fluence. For the simulation of deposition or etching experiments the dynamic binary collision code TRIDYN has to be used. In these simulations the incoming ions are characterized by their mass, atomic number, angle of incidence and kinetic energy, and the target is determined by the mass and atomic number, stoichiometry, and surface binding energy of the constituents, and the element or compound density. TRIDYN considers also the incident fluxes and the surface growth or etching rate. A range distribution of 8keV Ar ions implanted into cBN as calculated by TRIM is shown in figure 5.1a. The atomic Ar concentrations were calculated for an implantation dose of $1 \cdot 10^{16}$ ions.

To estimate the ion radiation damage, the total number of displacement collisions that occur during one ion impact can be estimated by TRIM. From this number of displacements per each incident ion, the total ion fluence and the atomic number density of the substrate the number of displacements per atom (dpa), i.e. of how often each target atom is displaced, can be calculated. For the example of a fluence of $1 \cdot 10^{16}$ Ar ions impinging with 8 keV onto cBN the distribution of the dpa is shown in figure 5.1b.

For a dynamic process like film growth or etching, the number of displacements per atom or generated Frenkel pairs c_{FP} can be calculated considering the total number of displacement collisions N_{tot} per incoming ion, the ion flux J_i and the velocity of the surface ν_s (i.e. the growth rate). Using the Gaussian depth distribution function of the displacements generated per incident ion obtained from static TRIM, the relative time dependent concentration of Frenkel pairs can be calculated according to

$$c_{FP} = \sum_{i}^{n} \frac{J_i N_{tot}}{n\nu_s} \left[erf\left(\frac{x-\bar{x}}{w}\right) - erf\left(\frac{x-\nu_s t-\bar{x}}{w}\right)\right] \tag{5.2}$$

with *erf* being the error function , w the standard deviation of the Gaussian, $\bar{x}$ its center with respect to the surface or approximately the mean projected ion range, and t being the deposition time.

c_{FP} is given in displacements per atom (dpa) and is a measure of how often each film atom has undergone a displacement due to the high energy ion bombardment. Since w and $\bar{x}$ are a function of the ion energy (for a fixed ion mass and target density) and J_i is proportional to the duty cycle, the number of dpa in the experiments discussed here is controlled by the pulse voltage and the duty cycle.

Figure 5.2 shows dynamic depth profiles that were calculated for a cBN film growing with 5 nm/min under argon and nitrogen ion bombardment for 20, 60, 240, and 360 s deposition time after the beginning of the high energy ion bombardment. This example was calculated for a bias voltage of -8 kV and a duty cycle of 0.6 % (see section 4.2). The dynamic damage profiles were calculated separately for Ar^+, N_2^+, and N^+ and superpositioned according to the actual ion fluxes (see table 6.1 in section 6.1). In the graph, the actual position of the

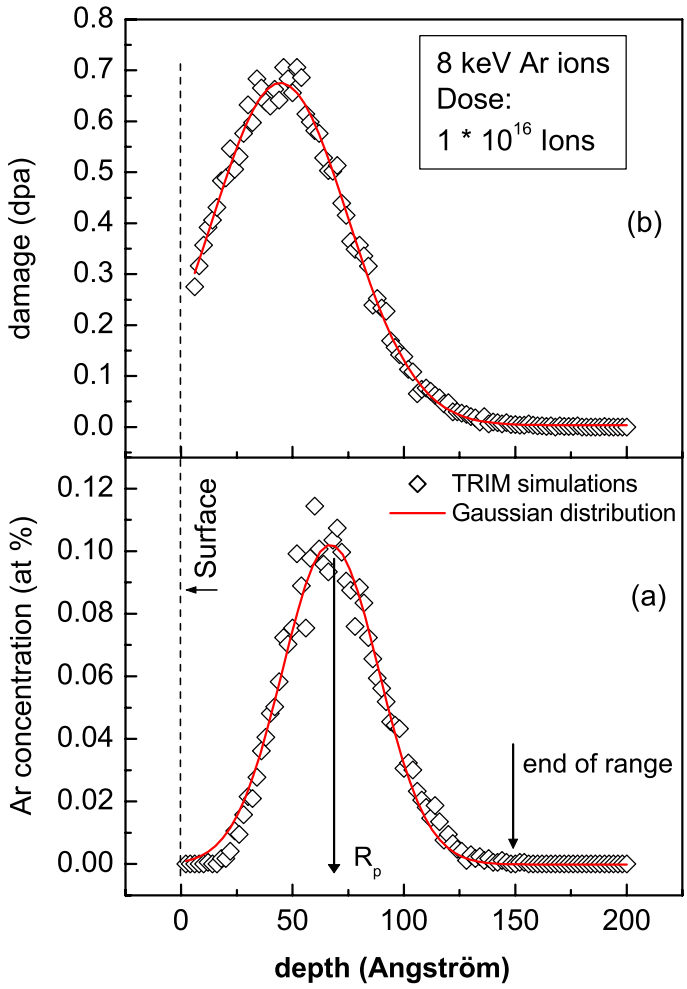

Figure 5.1: SRIM simulation of the Ar concentration profile (at%) and damage distribution (dpa) for the implantation of $1 \cdot 10^{16}$ Ar ions with an energy of 8 keV into cBN.

surface is indicated for each curve. The number of displacements are accumulating below the growing surface.

After about 5 min of film growth under ion bombardment, corresponding to an overgrown film thickness of about three times $\bar{x}$, a stationary amount of displacements is reached in the region well below the surface of the film, which represents the stationary bulk damage. The thin surface zone, where the damage is lower than the bulk damage value and where hence the state of stress is different from the bulk, is not considered, since the stress measured by cantilever bending (see section 7.1.1) is representative for the bulk. Only in section 8.4 where the results from x-ray absorption spectroscopy (XANES) are discussed, the stress in the surface region has to be considered, since this method is sensitive to the bonding configurations in the very surface region (max. 10-20 nm depth) .

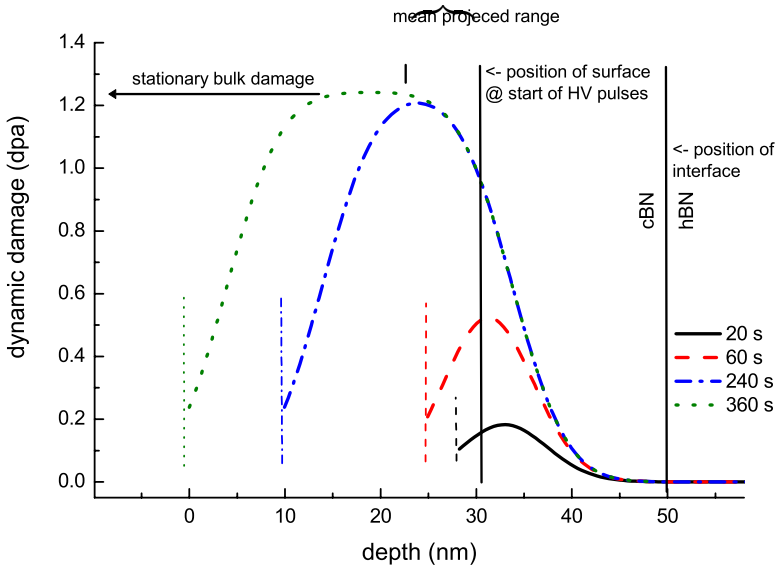

Figure 5.2: Dynamic damage profile evolution during Ar/N_2 ion bombardment of a cBN film growing with 5 nm/min. A bias voltage of -8 kV and a duty cycle of 0.6% were assumed. The profiles were calculated separately for Ar^+, N_2^+, and N^+ and superpositioned according to the actual ion fluxes (see table 6.1 in section 6.1).

In the following, the stress relaxation by simultaneous ion bombardment is discussed in terms of the stationary bulk damage. Since in most of the experiments, the parameters of the film forming (low energy) ion bombardment were kept constant , the damage that is introduced by these ions is not discussed here, although the damage that is introduced by the low energy ions (dynamic damage $\sim$ 3 dpa) is much higher than the damage due to the high energy ions .

6 Analysis of the deposition process

In magnetron sputtering the ion energy at the substrate is usually controlled by an external voltage that is applied to the substrate (bias or substrate bias). The energy that is gained by the ions traversing the plasma sheath has to be added to the energy gained due to the substrate bias. The neutral particles originate from sputtering at the target and therefore possess some kinetic energy of 10 to 20 eV [123, 124]. In order to understand and control growth and stress formation of the boron nitride films, the ion composition, flux, and energy distribution have to be known. Therefore, the ion density, plasma potential, and electron temperature have been measured with a Langmuir probe at the substrate position. Ion energy distribution and ion and neutral composition of the plasma including contaminations were measured using energy resolved mass spectrometry. The scaling of the incorporated neutral boron and nitrogen fluxes with the discharge power and pressure have been measured by elastic recoil detection analysis (ERDA) and the presence of contaminations originating from the sputter target, the sample holder, and the walls of the chamber were detected by Rutherford backscattering spectroscopy (RBS) and residual gas analysis. The experimental procedures of the ion beam analysis are given in sections 7.2.2 and 7.2.3.

6.1 Langmuir probe measurements

Electrical probes, commonly called Langmuir probes, are the oldest and up to date widely used tools to analyze plasmas. Such a probe consists of an electrode that is immersed in the plasma. By sweeping the probe through a voltage range and collecting the current from the plasma to the probe, electron and ion density (n_e and n_i, resp.), plasma and floating potential (V_p, V_f) and the mean electron temperature T_e can be evaluated. Further analysis yields also the electron energy distribution function (EEDF). Probe geometries can be planar, spherical or cylindrical. In this study, a cylindrical probe is used that consists of a thin tungsten wire. The dimensions of such a probe should fulfill the following requirements: the probe radius r should be much smaller than the sheath thickness s and the probe length l should be much larger than s. The dimensions of the tungsten wire are: $r = 0.19$mm, $l = 25$mm. In order to measure at the substrate position, during this measurements the substrate holder is removed.

As an example a current voltage characteristic (I-V curve) obtained from the r.f. unbalanced magnetron discharge is shown in figure 6.1. For large positive voltages, only electrons are collected by the probe and the current is called the electron saturation current. Between the plasma potential and the floating potential the electrons are repelled by the increasing

negative potential and only those who have sufficient energy reach the probe. Therefore this electron retardation region can be used to obtain the EEDF. At the floating potential the net current to the probe is zero. At high negative probe voltages (~ -60V), all electrons are repelled from the probe and only the ion current is collected. The current is then the ion saturation current.

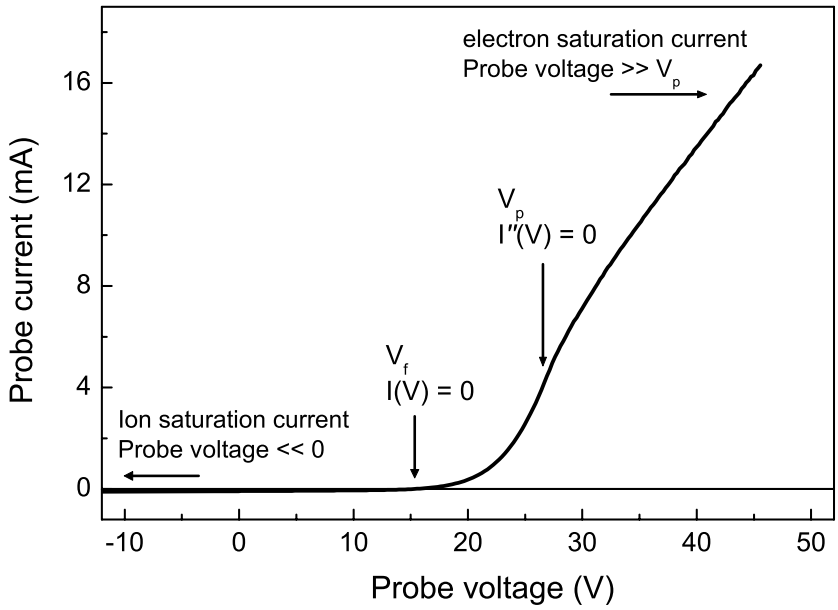

Figure 6.1: Current-voltage characteristic measured with a Langmuir probe in an Ar/N_2 magnetron discharge

The theory of electrical probe data analysis has been described by Chen [125] and by Swift and Schwar [126]. In 1966, Laframboise presented a numerical technique to extract the desired informations from the I-V characteristics [127]. A practically oriented review was published by Clements [128]. The main issues are pointed out in the following.

In order to simplify the analysis, some approximations are made: the plasma is homogeneous and isotropic, the sheath around the probe is collisionless (mean free path > probe radius), ions are only singly charged and have all the same mass, the ion temperature T_i is well below T_e, and finally the electrons have a Maxwellian energy distribution. Due to the magnetic confinement of the electrons, a magnetron discharge is naturally not homogeneous. But it is assumed that it is at least homogeneous within the surrounding of the probe tip. Also due to the unbalanced magnetic field, the electrons energy distribution is likely not a Maxwellian and a significant amount of electrons can be found in the high energy tail of the distribution [129, 130].

For a cylindrical probe of length l and radius r_p the collected ion saturation current I_i can be described as:

$$I_i = en_i r_p l \left(\frac{2\pi k T_e}{m_i}^{1/2} \right) i_i, \tag{6.1}$$

where m_i is the ion mass and i_i is a dimensionless ion current which originates from the sheath expansion due to the applied voltage and is a week function of the ion density [126].

The electron temperature can be obtained from the electron retardation region of the I-V curve. Here, the collected electron current is:

$$I_e \propto exp^{(\frac{eV}{kT_e})} \tag{6.2}$$

and a plot of lnI_e vs. V will give a straight line from whose slope T_e can be evaluated. The inflection point of the IV curve yields the plasma potential V_p, i.e. at $d^I(V)/dV^2 = 0$. The evaluation of the electron saturation current has some disadvantages since for probe voltages positive with respect to V_p, excessive electron currents can be collected by the probe. In this work the IV characteristics were analyzed using a commercially available software (Smart Soft ©Scientific Systems). Here T_e and V_p are extracted in a first step from spline fits. The software uses an iterative procedure to obtain n_i and i_i from the ion saturation current. Finally the electron density n_e is calculated from the probe current at V_p:

$$n_e = \frac{I(V_P)}{A_p}\left(\frac{2\pi m_e}{e^3 k t_e}\right)^{1/2}, \tag{6.3}$$

with A_p being the probe area and m_e the electron mass.

Probe measurements in magnetized and r.f. discharges

Probe characteristics can be influenced by a time varying field like in r.f. discharges and the presence of magnetic fields. Both are present in the magnetron discharge under investigation. In order to compensate for the r.f. field the probe has a reference electrode, which is allowed to follow the r.f. field and serves to correct the probe voltage. At the sputter target the magnetic field strength is 150 mT but decreases to less than 1 mT at the substrate position. Therefore the Langmuir probe current is not influenced significantly by the magnetic field lines.

Another source of error is the fact that a gas mixture is used and a number of different ions are present in the plasma (Ar^+, N_2^+, N^+). Since one single ion mass is used to calculate the plasma parameters from the I-V characteristic, an average ion mass is used here. It will be seen later from energy selective mass spectrometry that the ion composition in the discharge resembles the neutral gas composition. Therefore an average ion mass can be calculated on the base of the source gas composition.

6.2 Energy resolved mass spectroscopy

Ion and neutral composition, and ion energy distribution are measured with a HIDEN EQP 500 plasma monitor. The probe consists of an extractor tube with a 100 μm aperture followed by a 45° electrostatic energy analyzer (0 -100 eV) matched to a quadrupole mass filter (0 to 500 amu) and a secondary electron multiplier (channeltron). The plasma monitor is differentially pumped to a pressure of $5 \cdot 10^{-7}$ Pa. In neutral detection mode, neutral

species diffuse from the plasma into the mass spectrometer through the extractor orifice and are ionized by an integrated electron impact source. The electron energy can be adjusted between 10 and 120 eV. In general, the electron energy is held at 70 eV. By scanning the electron energy across the ionization threshold, also called appearance potential method, radicals in the plasma like atomic nitrogen can be detected [131]. Extractor and electron impact source can be biased to a positive potential. By choosing a bias voltage which is higher than the plasma potential, ions from the plasma are hindered from entering the analyzer. In the positive-ion-detection mode, ions pass through the orifice and are focused into the energy analyzer to be selected according to their energy. The selected ions enter the quadrupole r.f. mass filter to be detected as a function of their mass-to-charge ratio (m/z). Scanning the mass at fixed ion energy allows the detection of various ionic species, whereas scanning the energy at a fixed mass allows the measurement of the ion energy distribution. The plasma monitor is located at the substrate position with the orifice perpendicular to the target and substrate axis. In this way covering (and eventually complete sealing) of the pinhole by sputtered atoms from the target is prevented. In such a configuration, information is collected only from the plasma since the sputtered species cannot enter the pinhole.

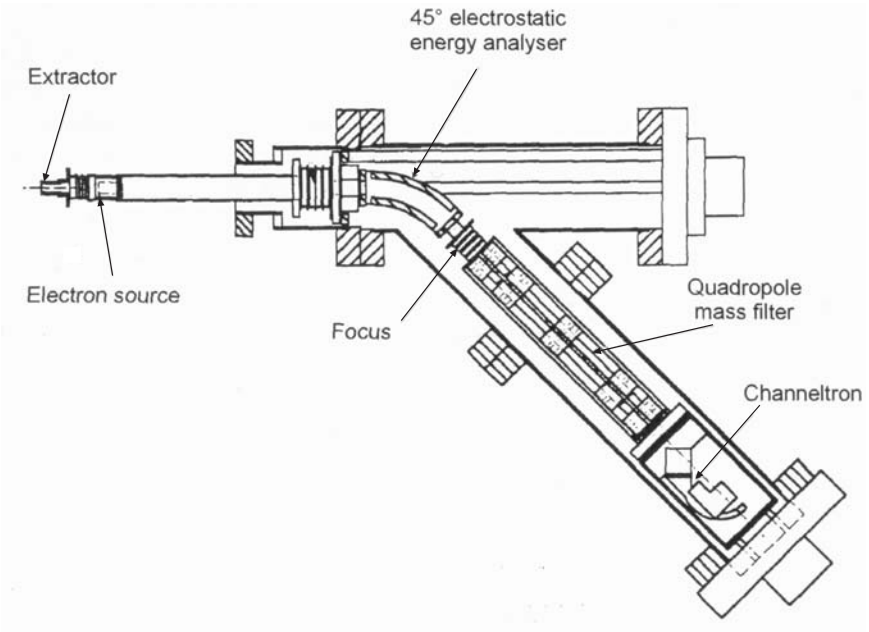

Figure 6.2: Schematic view of the HIDEN EQP 500 energy selective mass analyzer

In the following sections the ion and neutral characteristics of the magnetron discharge are discussed.

6.3 Ion characteristics

In figure 6.3 the ion densities N_i of a pure argon and a pure nitrogen discharge are plotted as a function of the working gas pressure. For both pure gases and the investigated mixed compositions, ion density increases with the pressure and r.f. power (not shown). Comparing the two gases, the ion density in the argon discharge is 4 to 5 times higher than in a nitrogen discharge at otherwise identical conditions. The increase of N_i with the argon content in the plasma is shown in figure 6.4. Studies of Pintaske et al. [16] on r.f. and dc Ar/N_2 magnetron discharges used for BN thin film deposition have shown similar results using a double Langmuir probe.

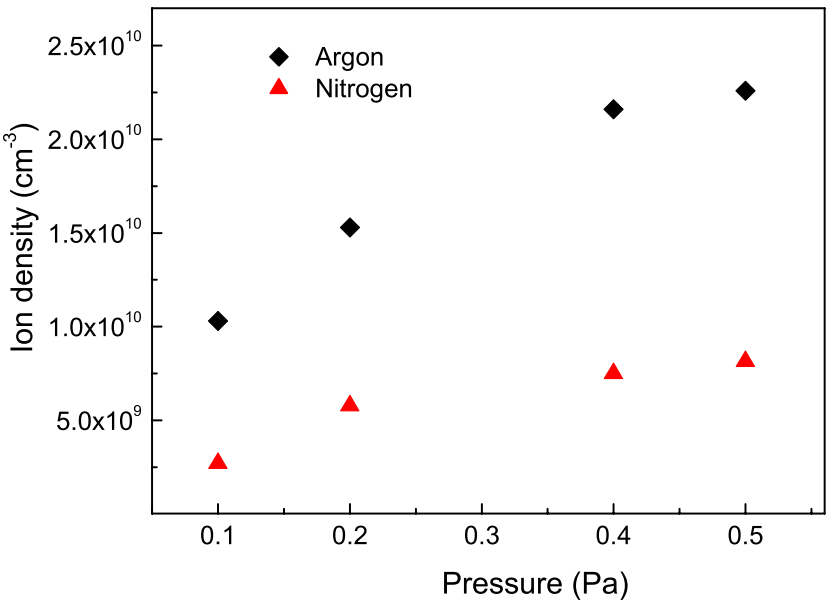

Figure 6.3: Ion density in an argon discharge (diamonds) and nitrogen discharge (triangles) at 225 W discharge power as a function of pressure.

In Figure 6.5 the spatial ion density distribution is shown for an Ar discharge. In this experiment, the Langmuir probe was moved stepwise outward from the center of the discharge. The ion density is constant within 5% up to a distance of 20 mm from the center of the discharge, and then decreases rapidly down to 50% at 50 mm. This inhomogeneous distribution results from the magnetic confinement of the electrons by the unbalanced magnetron configuration. It has to be considered that the inhomogeneous ion density distribution leads not only to a lower degree of ion bombardment but also to a lower deposition rate in the outer parts of the substrate.

The ion composition and the ion energy distribution function were measured by energy selective mass spectrometry. A typical ion mass spectrum sampled by the plasma monitor is shown in Figure 6.6. The dominant ion species in an Ar/N_2 discharge are Ar^+ and N_2^+. A small amount of N^+ ions is found, Ar^{2+} is not detected.

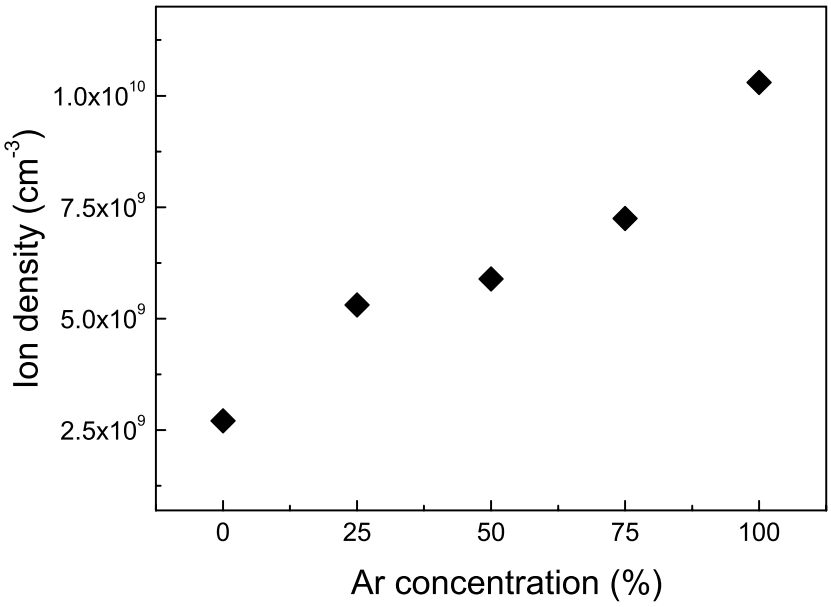

Figure 6.4: Ion density as a function of the Ar concentration in the discharge, measured at 0.1 Pa and 225 W discharge power.

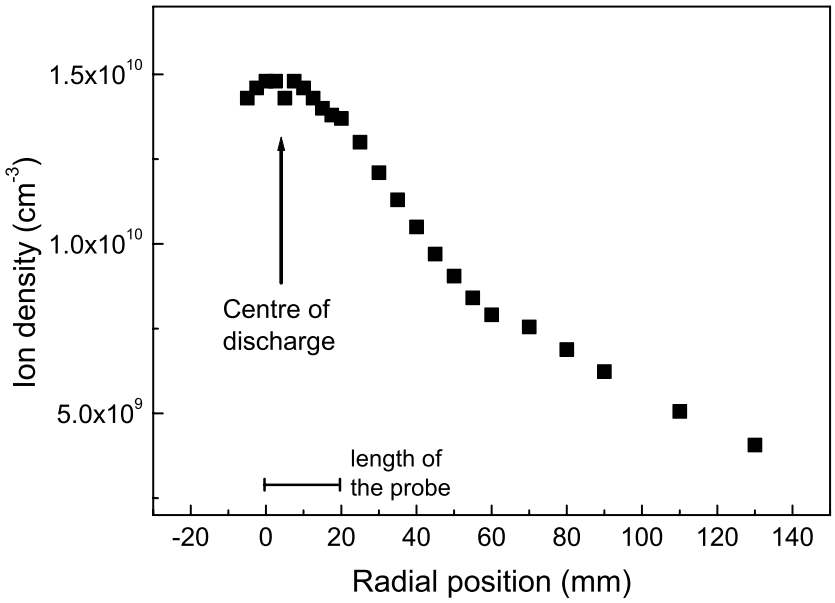

Figure 6.5: Radial distribution of the ion density across an Ar discharge, measured at 0.1 Pa and 225 W discharge power.

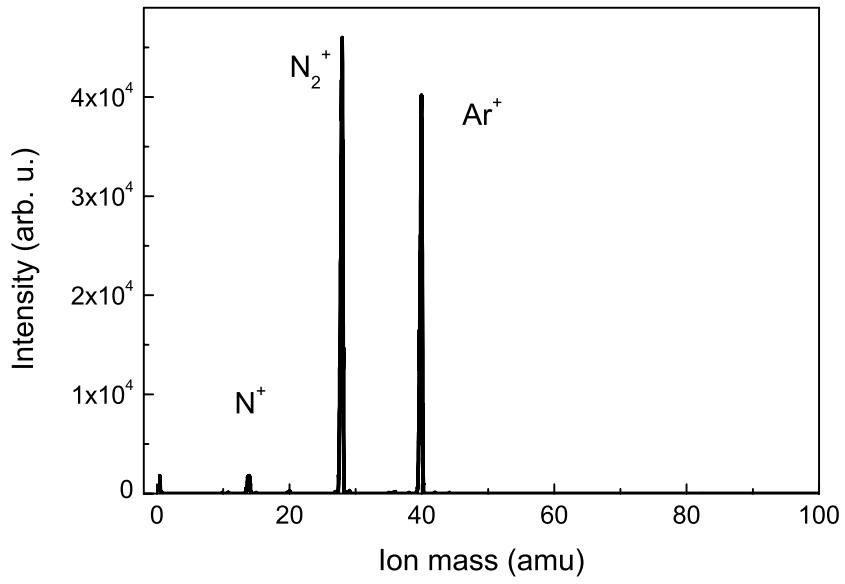

Figure 6.6: Ion mass spectrum of an Ar/N_2 discharge. The Ar and N_2 gas flows were 10 sccm each, the total pressure was 0.1 Pa and the discharge power was 225 W.

Figure 6.7 shows the representative Ar^+ and N_2^+ ion energy distributions (IED) in an 50% Ar/50 % N_2 discharge recorded with the plasma monitor. These IED consist of a single narrow peak with full width at half maximum (FWHM) of about 4 eV. The width of the ion energy distribution mainly arises from the ion optics of the plasma monitor and the resolution of the energy analyzer. The narrow IED and the very small number of low energy ions indicate that the sheath is collisionless. Under these conditions the ion energy corresponds to the plasma potential, which is confirmed by Langmuir probe measurements (see below, fig. 6.8). The ratio of the integrated areas under the IED peaks yields an ion composition of 48 % Ar^+ and 52 % N^{2+}. Although the ion density increases with the Ar content in the discharge, the ion composition reflects the neutral gas composition. Since the ionization energy and the collision cross section for electron impact ionization are very similar for Ar^+ and N_2^+ ($\sim$ 15.7 eV and $2.5 \cdot 10^{-20} m^2$, resp. [132]), comparable ionization rates are reasonable. It is known that in argon discharges ionization occurs also due to collisions of excited neutrals, since their relaxation energy is higher than the ionization energy. This process, called Penning ionization, can explain the higher ion density in the argon rich plasmas.

Figure 6.8a shows the plasma potential as measured by the langmuir probe in Ar and N_2 plasmas as a function of the working gas pressure and in figure 6.8b the electron temperature dependence on the working gas pressure is presented. The plasma potential is independent of the r.f. power in pure Ar as well as in N_2 discharges. For pure argon the plasma potential exhibits very little dependence on the pressure and ranges from 35 to 45 V. In the case of nitrogen the plasma potential is high for low pressure (55 V at 0.1 Pa). As pressure increases, the plasma potential decreases towards a plateau of about 30 V. The evolution of plasma potential is related to the electron temperature: a decrease in the plasma potential is

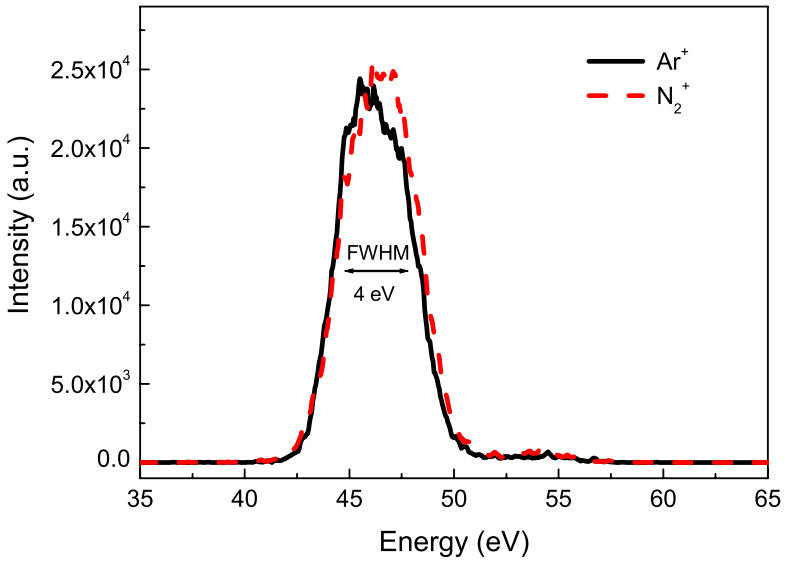

Figure 6.7: Ion energy distribution of Ar^+ and N_2^+ ions in a mixed Ar/N_2 discharge. The Ar and N_2 gas flows were 10 sccm each, the total pressure was 0.1 Pa and the discharge power was 225 W.

observed as the electron temperature decreases. In general the plasma potentials measured in the magnetron discharge are rather high compared with r.f. discharges without magnetic confinement (usually around 20 V). A reason could be an artificial loss of electrons due to the unbalanced magnetic field: the electrons follow the magnetic field lines and are driven out of the discharge and, as a consequence, a higher plasma potential is induced.

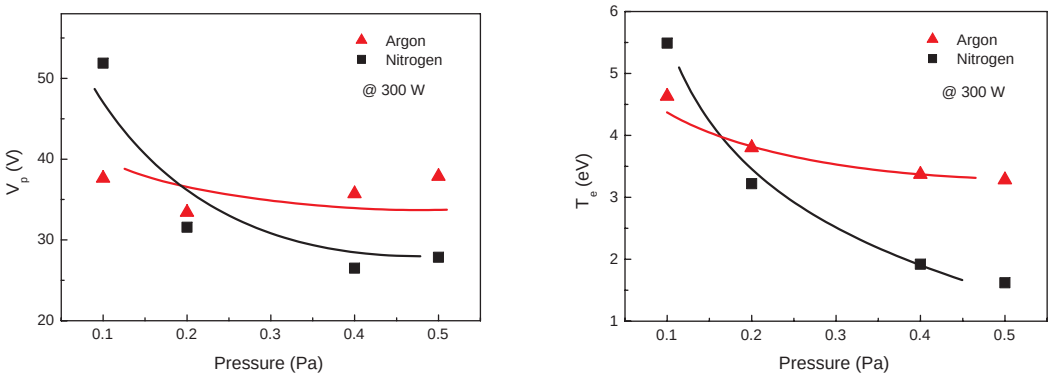

Figure 6.8: a) Plasma potential in Ar and N_2 discharges at a r.f. power of 300 W as function of the pressure and b) Electron temperature in Ar and N_2 discharges as function of the pressure

6.4 Neutral characteristics

In figure 6.9 a typical neutral mass spectrum measured with an electron impact energy of 70 eV is shown. The spectrum shows contributions from Ar^+, Ar_2^+, and N_2^+, which indicates the presence of Ar atoms and N_2 molecules in the plasma. N^+ ions are present in the spectrum and can be attributed to the presence of N_2 molecules and N atoms in the plasma, corresponding to dissociation or direct ionization, respectively, in the electron impact ion source of the plasma monitor. To distinguish the contributions of N_2 and N to the N^+ signal, appearance potential spectroscopy was applied [131]. This experiment showed the amount of atomic nitrogen to be under the detection limit, indicating a low dissociation rate of nitrogen molecules in the plasma and a neutral gas consisting mainly of Ar and N_2. In pure Ar discharges, N_2 is detected in small amounts. This points to the presence of residual nitrogen or the presence of nitrogen in the plasma which originates from the boron nitride sputter target. It is observed that the detected signal increases with r.f. power and hence with the sputter rate. Therefore it is suggested, that this nitrogen is sputtered from the target and subsequently undergoes recombination. In this low pressure a recombination seems more likely to take place on any surface (target holder or walls of the reactor), than by collision in the plasma, since the mean free path for N-N collision are 1.7 m at 0.1 Pa and 0.35 m at 0.5 Pa (calculated from the covalent radius of N atom).

In the neutral mass spectrum (figure 6.9) an H_2O^+ peak is observed revealing the presence of H_2O in the chamber. The moisture arises from desorption of water from the wall of the chamber and the surface of the sputter target. This amount of water in the system can be reduced effectively (by a factor of 10) by bake-out or running the discharge for 10 to 15 min prior to the deposition.

The neutral particle flux to the substrate was estimated in a series of deposition experiments in an argon discharge without bias voltage. In this way, no ionized nitrogen species but only sputtered atoms from the target are incorporated into the film. The elemental depth profile, measured with ERD (see section 7.2.2), of a BN film produced in this way is shown in figure 6.10. Due to the presence of ^{10}B and ^{11}B isotopes that can not be separated in the detector, the B depth profiles are shifted (see section 7.2.2). The integrated area densities are however correct and the B/N ratio is 1.8. The nitrogen deficiency correlates with the recombination of some sputtered nitrogen to volatile N_2. Stoichiometric films can be grown with a nitrogen concentration in the discharge of at least 30%. The amount of oxygen and hydrogen contamination from the residual gas are 3 at% and at%, respectively. The oxygen is concentrated mainly on the film/substrate interface and near the film surface. Its presence is likely due to the native silicon oxide and surface contamination. Hydrogen is distributed homogeneously through the film. It was found that hydrogen and in some cases also oxygen are present in high concentrations (up to 8 at %) in boron rich films, in stoichiometric films however,the H and O concentrations are less than 2 at% of the film composition.

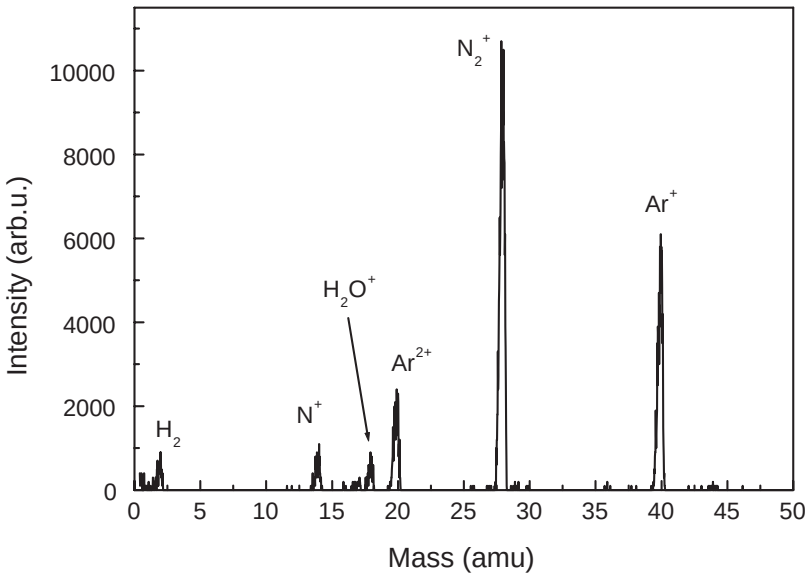

Figure 6.9: Neutral mass spectrum of an argon-nitrogen discharge. The Ar and N_2 gas flows were 10 sccm each, the total pressure was 0.1 Pa and the discharge power was 225 W.

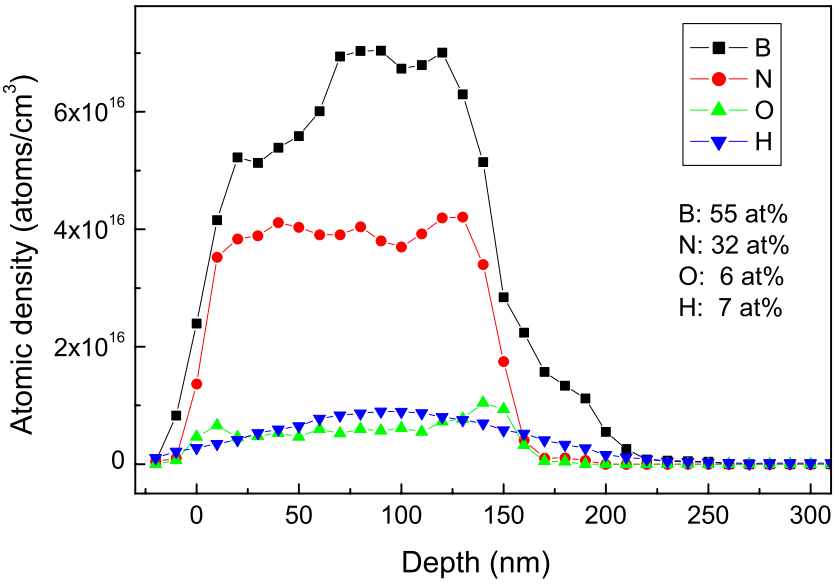

Figure 6.10: Elemental depth profile of a BN layer grown in Ar discharge at 0.1 Pa and 250 W r.f. power without substrate bias

6.5 Summary of the process analysis

Using the Child law the ion flux J_i to the substrate surface was calculated from the electron temperature kT_e and the averaged ion mass m_i according to

$$J_i = 0.6 \cdot N_i \cdot \sqrt{\frac{kT_e}{m_i}}. \tag{6.4}$$

Similar to the ion density, the ion flux is also increasing with the working gas pressure, the discharge power, and the argon content in the plasma. The results are summarized in figure 6.11 and table 6.1.

From the area density of boron and nitrogen the incorporation rates have been calculated. For a deposition in argon at 0.1 Pa , they are shown together with the calculated ion fluxes in figure 6.11 as a function of the r.f. power. Now it is possible to estimate roughly the ion to neutral flux ratio. For the given conditions it is in the order of 1 $\frac{ion}{(B+N\ neutrals)}$. Only a very rough estimation of the flux ratio can be made, since in deposition experiments nitrogen is added to the plasma and a considerable amount of nitrogen arrives as energetic ionized species at the substrate.

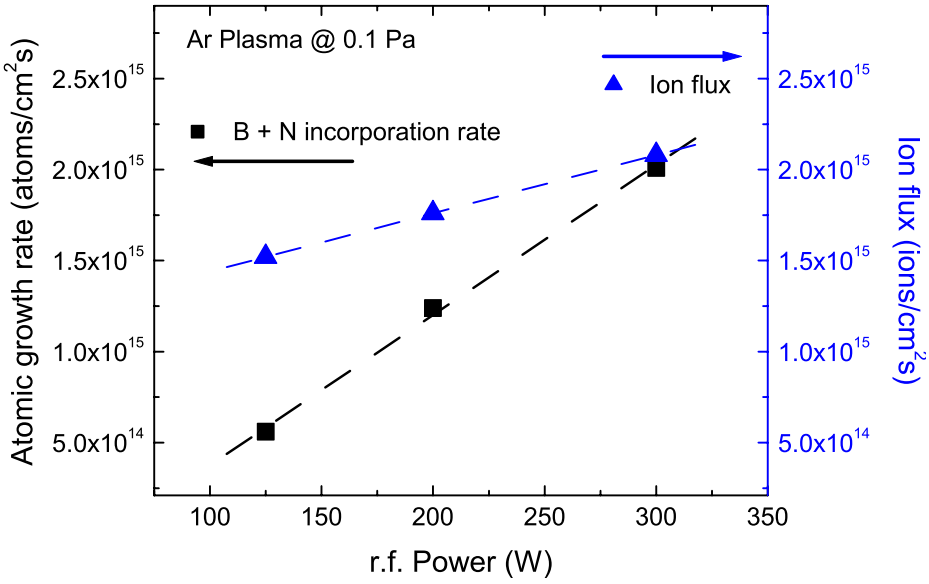

Figure 6.11: Ion flux and neutral (B + N) incorporation rate as a function of r.f. power for an Argon discharge at 0.1 Pa

The ion and neutral fluxes obtained for the standard deposition conditions (see table 4.1 in section 4.2) are summarized in table 6.1. Since N_2^+ ions dissociate upon impact on the substrate surface, the total flux of nitrogen ions to the substrate surface equals the argon flux. After the dissociation, the two nitrogen radicals are left with half the energy of the primary ion. The consequence of this is that in a mixed Ar/N_2 discharge the film surface is bombarded with ions of different energies.

Table 6.1: Ion and neutral particle fluxes to the growing film surface for standard deposition conditions (see table 4.1 in section 4.2).

Fluxes to the film surface	**Value** (particles/cm^{2}s)
B + N	$1.7 \cdot 10^{15}$
Ion flux (total)	$1.5 \cdot 10^{15}$
Ar^+	$9.75 \cdot 10^{14}$
N_2^+	$4.2 \cdot 10^{14}$
N^+	$1.05 \cdot 10^{14}$

7 Film characterization

7.1 In situ diagnostics

7.1.1 Stress measurement

In section 3 it was demonstrated how shear forces in a stressed thin film lead to a bending of the substrate. The principle of a bending substrate is therefore a useful tool for the analysis of stress in a thin film and was already described by Stoney in 1909 [106]. For the in situ analysis of stress in cBN films in this work a combination of laser deflection and spectroscopic ellipsometry is employed. The experimental set up and the data analysis were developed by Fitz and Fukarek et al. [8, 133] for IBAD and were adopted for magnetron sputtering during this work. The laser deflectometry and the stress measurement are described in this section, the experimental set up of the in situ spectroscopic ellipsometry is described in section 7.1.2.

According to equation 3.6 the substrate bending radius R and the film thickness d_f have to be known to calculate the force per unit with (FPUW) and the global film stress S. To obtain the depth distribution of S, i.e. the instantaneous stress σ, the differential film thickness and the bending radius as a function of the film thickness are required (eq. 3.7). In principle, R and d_f can be obtained ex situ for e.g. by measuring the substrate curvature and d_f by profilometry after certain steps of deposition or after stepwise back etching of the complete film [71] [134]. But to be able to resolve the layer structure of the BN films accurately, the FPUW and d_f have to be measured dynamically during the deposition. The experimental set up for the in situ stress measurement on cantilever substrates is schematically shown in figure 7.1. The cantilever is clamped into a molybdenum mask of 3" diameter that is placed on the substrate holder, as shown in figure 7.1. The mask is used to fix the cantilever and to ensure good electrical contact with the substrate holder since the substrate has to be biased. Outside the chamber a HeNe Laser is placed together with a beamsplitter in such a way that two parallel beams with 5 mm distance are directed onto the substrate. One laser beam is reflected on the cantilever tip, the other on the sample reference position. Using a rotating beam chopper either one of the beams is passed into the chamber or both are blocked and the offset is measured. The beams are denoted C, R, and off (cantilever, reference, and offset). Two photo diodes at the beam chopper report the actual state of the chopper to the personal computer (PC). After reflection on the cantilever, the laser beam hits a 2 dimensional position sensitive diode (PSD) of 20 x 20 mm area and induces a photo current. This current is measured in the x and y direction of the array (I_x and I_y, resp.). An amplifier converts the measured photo currents into output voltages for

the x and y direction (U_x and U_y) and corrects the voltages for field distortions of the array. An analog digital converter (ADC) measures and converts the voltages to digital data. All PSD data (cantilever beam, reference beam and off set) are recorded continuously by the PC together with the signal from the photo diodes. During the data analysis all the position data points are separated according to the C, R, and off position of the beam chopper.

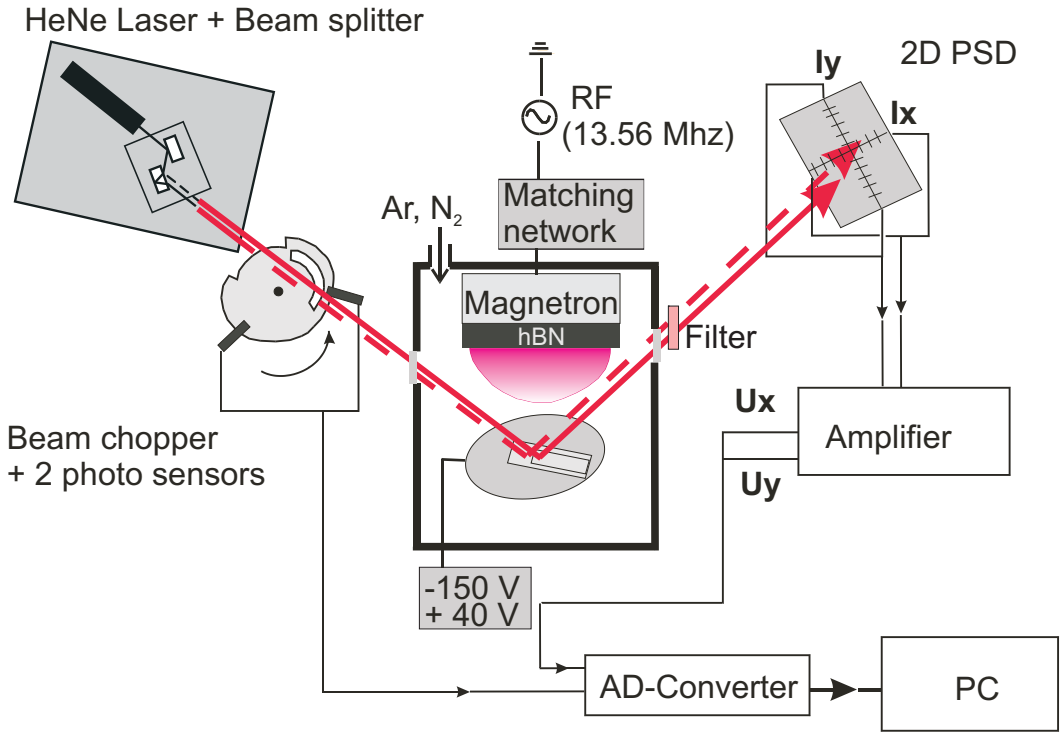

Figure 7.1: Experimental set up for the in situ laser deflectometry

The principle of laser deflectometry on a bending cantilever is shown in figure 7.2. Due to the bending of the cantilever, the position of the C-Laser beam on the PSD is shifted by x. By geometric considerations the bending radius of the cantilever can be calculated according to equation 7.1. The second laser beam is used as a reference beam and reflected on a fixed position on the cantilever frame. Then ΔX in equation 7.1 is the relative change of the distance between the two laser spots on the PSD. L is the distance between the cantilever tip and the PSD and is 280 mm, $l = 22$ mm is the length of the cantilever.

$$\frac{1}{R} = \frac{\Delta X}{2Ll} \tag{7.1}$$

The spatial resolution with which the position of the laser spot on the PSD can be determined depends on the preset sensitivity of the ADC board, which is the voltage range divided by 1024, and the noise level. Here, the voltage range was -10 V to +10 V giving a resolution limit of the ADC of 0.02 V corresponding to ΔX of 20 μm. The resolution is limited however mainly by the level of noise, which is $\Delta U = 0.25$ V corresponding to $\Delta X = 25$ μm. From this the resolution of the bending radius is calculated to be 45 m and ΔFPUW is then 20 GPa*nm. The rotation frequency of the beam chopper is ~ 0.5 Hz, therefore a

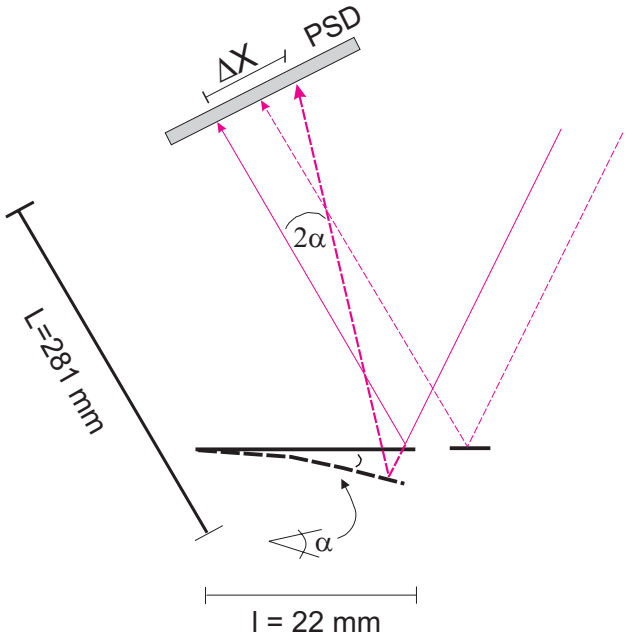

Figure 7.2: Deflection of two parallel laser beams on a bending cantilever substrate

full set of data (incl. U_x^C, U_y^C, U_x^R, U_y^R, U_x^{off}, and U_y^{off}) can be recorded each 2 seconds, which equals an increase of d_f of approximately 0.8 to 1.6 Å.

Since the substrate holder is solid and properly connected with the chamber walls, distortion due to heating is negligible and hence the laser deflection is not significantly influenced or misaligned by thermal movement of the substrate holder. Nevertheless a reference beam is required for the data analysis, since there is some signal of the PSD that originates from the magnetron plasma. An interference filter is used to block all other wave lengths besides the laser wave length (632 nm), and in principle the signal coming from the plasma is very low compared with the laser intensity. However, during growth the reflected laser intensity undergoes interference maxima and minima due to reflection of partial beams at the substrate/film interface. In the interference minima the reflected intensity is almost zero and the signal of the PSD is entirely caused by light emission from the plasma. The reference beam is here used to established the point of the interference minimum (to be sure, the signal is not coming from the cantilever bending). The data recorded during these minima are not evaluated (or interpolated) and during the experiments it was taken care not to induce any additional signal of cantilever bending by changing deposition parameters or nucleation of the cBN. In figure 7.3, the calculated FPUW are plotted on the left y-axis and for comparison the measured reflected intensity of the reference laser is plotted on the right y-axis. The interference minima appear at $\sim$ 80 and 250 nm film thickness. In this regions the FPUW data are marked red and for the analysis of the instantaneous stress the curve is interrupted here. But since the real slope of the curve does not change in this regions, the data can be interpolated across the interference minima. The physical features of the FPUW curve are discussed in detail in sections 8.1 and 8.2.

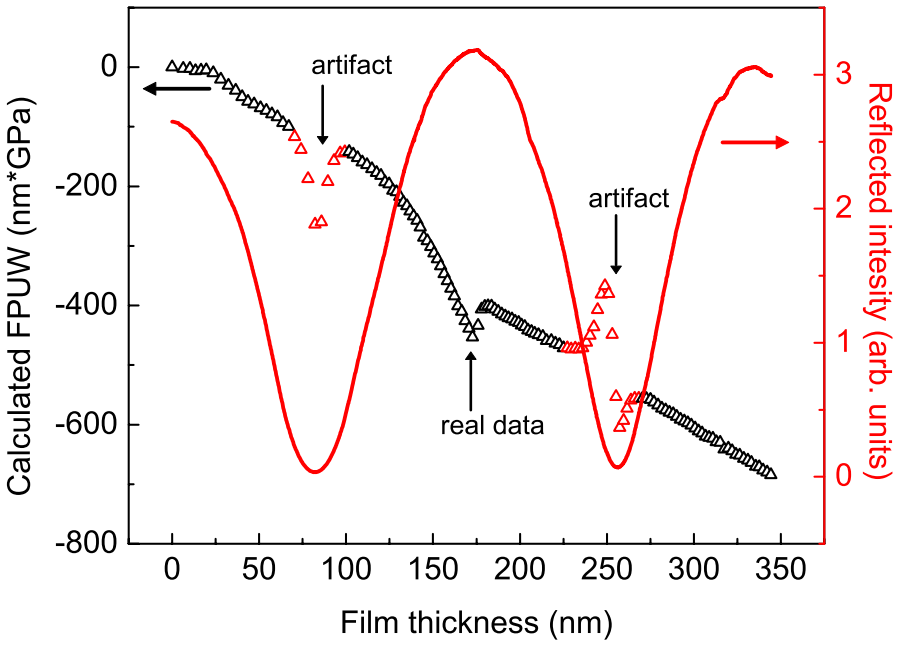

Figure 7.3: Calculated FPUW and reflected laser intensity showing the measurement artifacts due to interference minima in the reflected laser intensity.

7.1.2 Spectroscopic ellipsometry

Ellipsometry is a very sensitive tool for the analysis of optical properties of thin films and multilayer stacks. The technique is based on the measurement of the state of polarization of initially linear polarized light after reflection of the sample surface. In figure 7.4 the optical set up of an ellipsometry experiment is schematically shown.

In references [136] and [135] reviews on the theory of ellipsometry are given. The plane that is defined by the vectors of the incident and reflected beam and the normal to the sample surface is called the plane of incidence. The p- and s- direction denote vectors parallel and perpendicular to the plane of incidence, respectively. The incident polarized light (superscript i) is characterized by the components of the electric field in p and s direction E_p^i and E_s^i. The polarization state of the incident wave is defined as $\chi^i = E_p^i/E_s^i$. The same conventions are used for the wave reflected of the sample surface and the reflected polarization state is $\chi^r = E_p^r/E_s^r$.

For isotropic media the electric field components of the reflected wave are $E_p^r = r_p E_p^i$ and $E_p^s = r_s E_s^i$ where r_p and r_s are the complex amplitude reflection coefficients with $r_{p,s} = e^{i\delta_{p,s}}$. The change of the polarization state due to interaction of the light with the sample is characterized by the Fresnel reflection coefficient ratio ρ and often expressed with the ellipsometric angles Ψ and Δ:

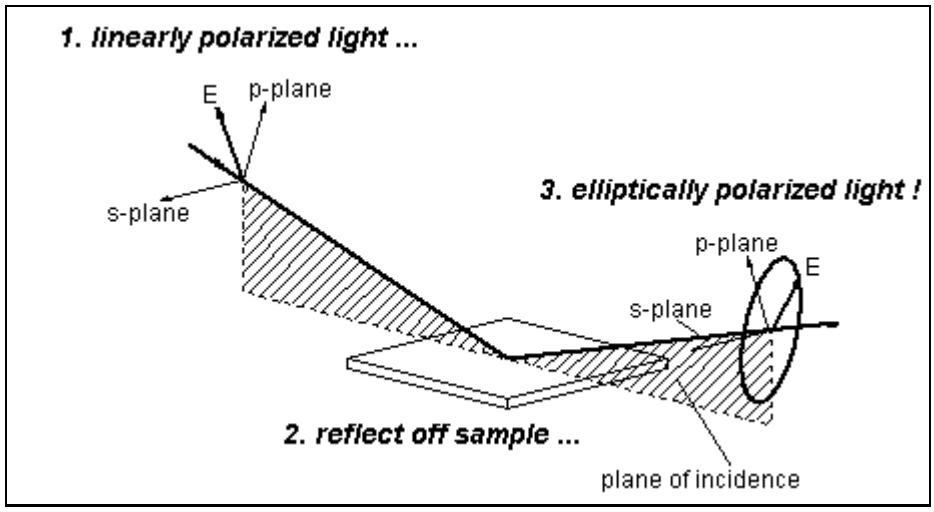

Figure 7.4: Geometry of an ellipsometric experiment showing the p- and s- planes [135]

$$\rho = \chi_i/\chi_r = r_p/r_s = tan\Psi e^{i\Delta} \tag{7.2}$$

where Ψ and Δ denote the ratio of the Fresnel reflection coefficients and the phase shift between the Fresnel reflection coefficients in p and s direction.

In ellipsometry only the ratio of the measured quantities is required, which is much more precise than measuring absolute intensities. Each of the parameters in equation 7.2 is dependent on the wave length λ, the angle of incidence Φ, the dielectric function of the sample, and in case of investigations on thin films also the film thickness. In the experimental set up an in situ M44 spectroscopic ellipsometer (J.A. Woollam Co., Inc. Lincoln, NE, USA) was used that measures at 44 wave lengths in the range between 340 nm and 630 nm under an fixed angle of incidence of 70°. During deposition, a full spectrum of Ψ and Δ values is taken approximately every 2 s.

To obtain the dielectric function and the thickness of the film each Ψ and Δ spectrum is fitted with an optical layer model using the WVASE software by J.A. Woollam Co., Inc. [135]. The layer model consists of the silicon substrate at 400°C, 1.5 nm SiO_2, and an hBN and cBN layer. Bulk highly oriented hBN is uniaxial negative[1] with $n_e = 1.65$ (E||c) and $n_o = 2.17$ (E $\perp$ c) [137]. Thus n_o of hBN can be even higher than the refractive index of cBN ($n_{cBN} = 2.11 - 2.13$ at 630 nm [137]). In the visible range both BN phases are essentially transparent [138]. Due to this similarity of the optical constants of hBN and cBN in the visible range, it is not possible to distinguish clearly between the phases using the M44 Ellipsometer. If the spectral range is extended to either the UV [139, 140] or the infra red [80, 141], hBN and cBN can be very well distinguished by ellipsometry due to the position

[1] i.e. the material is optically anisotropic. In trigonal, tetragonal and hexagonal crystals two different refractive indices n_o and n_e exist along different crystallographic orientations. Perpendicular to the c axis is the *ordinary* direction with n_o, and parallel to c is the extraordinary direction with n_e. If $n_o > n_e$, the material is uniaxial negative. Crystals with lower symmetry have three different refractive indices along the three crystallographic orientations and are optically biaxial.

of the band gap or the different phonon positions.

The total film thickness and the growth rate of an hBN/cBN film however can be obtained with good accuracy from in situ ellipsometry in the visible range, as it is done in this work. As an example, in figure 7.5 the hBN and cBN layer thickness as well as the total calculated films thickness are shown. The slight oscillations of the individual layer thickness, especially after the deposition was stopped, arise from the proximity of the dielectric constants. But the total film thickness increases continuously and remains constant after the deposition has been stopped. Due to the different densities of hBN and cBN, the growth rate decreases significantly during the cBN nucleation and grain coalescence.

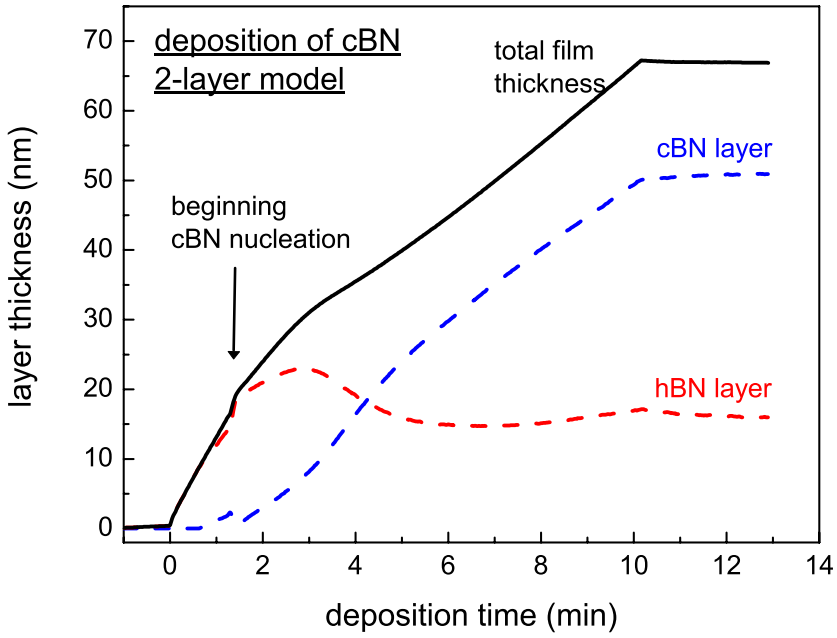

Figure 7.5: Resulting thickness of the hBN and cBN layer of the optical layer model and the total film thickness as a function of the deposition time

In situ ellipsometry is also used to determine the temperature of the silicon substrate before the beginning of the deposition. For this, one takes advantage of the fact that the band gap of silicon shifts to lower energies with increasing temperature. In figure 7.6, a Δ/Ψ plot for room temperature (RT) and deposition temperature is shown. Using a calibration at 10 different temperatures between RT and 450° C, the temperature of the measured sample is estimated by interpolation to be 340°C ± 20°C.

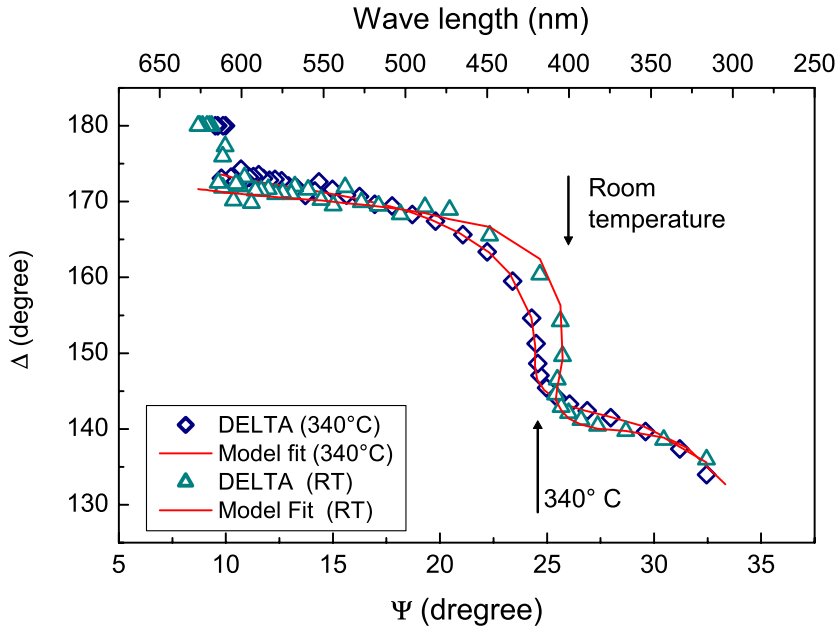

Figure 7.6: Δ/Ψ plot for Si at room temperature and 340 °C, showing the temperature induced shift of the band gap position

7.2 Ex situ diagnostics

7.2.1 Infrared spectroscopy

Infrared spectroscopy is the most widely used technique to characterize the phase composition of boron nitride films, since it is non-destructive and provides fast and meaningful information. It is based on the absorption of the incident photons in the infrared region by lattice vibrations. If the film and the substrate material are both transparent in this spectral range (like BN films on silicon), IR spectra can be recorded in transmission geometry. In the case of either metallic films or substrates, e.g. BN films on TiN, reflection geometry has to be used. In this work, the spectra are recorded with a MagnaFTIR fourier transform infrared spectrometer (Nicolet) in reflection geometry with an angle of incidence of 9°. The incident beam is s-polarized, i.e. the E vector of the light is perpendicular to the plane of incidence. To compensate for the spectral dependence of the IR light source and the sensitivity of the detector, all sample spectra are normalized to a reference spectrum of an aluminum mirror.

As an example the IR spectrum of a boron nitride film that was deposited during this study is shown in figure 7.7.

The cubic boron nitride phase is identified by the presence of the cBN TO mode or Reststrahlen region, which appears in bulk material at 1065 cm^{-1} [142]. The in-plane B-N stretching and out-of-plane B-N bending modes of the hexagonal BN phase are located at 1367 cm^{-1} and 783 cm^{-1}, respectively [143]. The intensity ratio of the out-of-plane and the in-plane mode can provide information on the orientation of the hexagonal basal planes

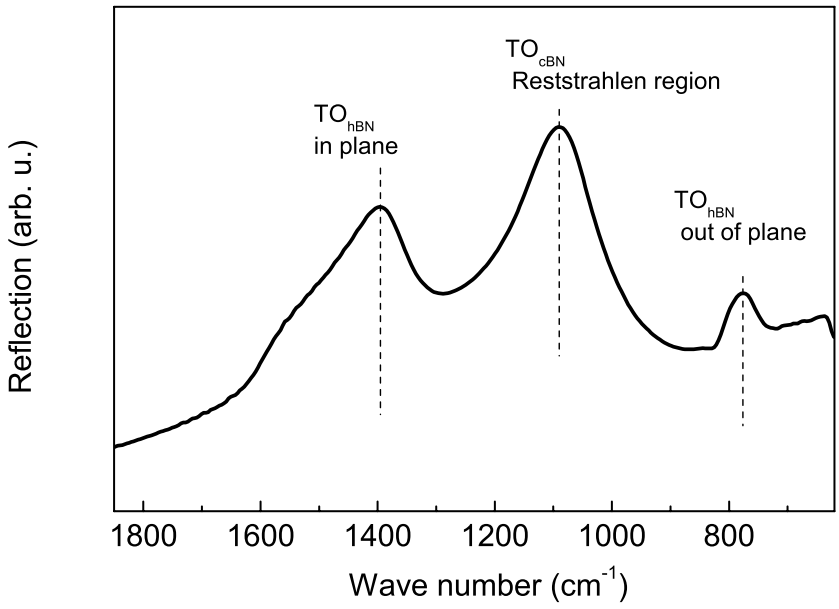

Figure 7.7: IR reflectance spectrum of a BN thin film showing the cBN Restrahlen region and the hBN in-plane and out-of-plane modes.

with respect to the substrate normal [144].

In the disordered tBN this intensity ratio can give also information on the degree of interplanar ordering [134].

In general, the volume fraction of cBN F_c in the films can be estimated by either the peak intensity ratio

$$F_c = \frac{I_c}{I_c + I_h} \tag{7.3}$$

or the peak area ratio

$$F_c = \frac{A_c}{A_c + A_h} \tag{7.4}$$

with I_c and A_c the normalized peak intensity and peak area of the cBN Reststrahlen region around 1100 cm^{-1} and I_h and A_h the peak intensity and peak area of the hBN absorption around 1400 cm^{-1}. Several data are available in the literature for the absorption coefficients of hBN (α_h) and cBN (α_c). However the ratio $\frac{\alpha_h}{\alpha_c}$ is in the order of unity [144], therefore equations 7.3 and 7.4 are widely used to estimate the relative cBN content of thin films. There are however some objections against this procedure. A strong orientation of the hBN with the axis parallel to the substrate can lead to an overestimation of the cBN content ([30] and references therein). Further, for thin films interference effects have to be considered due to multiple reflections on the substrate film interface. Also the layered structure of the BN films can not be resolved since the total film volume is sampled. In order to obtain the desired cBN content of the cBN top layer, the spectra should be either measured in situ [145] or by comparing the IR spectra of samples deposited with increasing time [60]. In

this way the contributions of hBN and cBN layers to the IR spectrum can be separated. A more precise analysis of IR spectra can be done by modeling the dielectric function with an optical layer model, where the TO phonons are described as damped harmonic oscillators [146, 147].

The resonance frequency ω_0 of phonons in crystalline material is related to the strain of the material, i.e. a measured shift of the resonance frequencies can give information about the stress of the sample. For bulk cBN the dependence of the TO phonon position on hydrostatic pressure P was measured by Raman spectroscopy [148] to be

$$\omega_0(P)/cm^{-1} = 1054.7 \pm 3.38 \cdot P/GPa \tag{7.5}$$

This experimental work is in agreement with theoretical calculations by Fahy [149] and Cardona et al. [150]. In the case of thin films, however it is very ambiguous to use the peak shift of the cBN phonon as a direct measure for stress in the layer. Fitz et al. [147] compared a number of stress and IR data published by different authors [12, 151, 152] and showed that there is no clear relation between the measured stress and the cBN TO phonon position. An effect of the film thickness can arise due to the reflection of partial waves at the interfaces. During the island-type nucleation of the cBN, (see section 2.2.4), a depolarization by the small and separated cBN grains cause a shift of the phonon frequency up to 80 cm^{-1}, which outranges the effect of strain. After coalescence still the cBN phonon frequency can be shifted by the gain size and stoichiometry [147].

7.2.2 Elastic recoil detection analysis

The boron and nitrogen contents of the BN films and the depth profile of the B/N ratio are investigated with elastic recoil detection (ERD) analysis. Also the contamination by the light elements H, C, and O is quantified with ERD. The samples are irradiated with 35 MeV $^{35}Cl^{6+}$ ions under an incidence angle of 15°. The elastically recoiled target atoms were detected with a Bragg ionization chamber as a function of the atomic number Z and the energy, which is related with the escape depth of the recoil. The depth resolution of the detector is $\sim$ 5 nm. Since with the Bragg chamber the recoils are detected as a function of Z and not of their mass, in the spectra the ^{10}B and ^{11}B isotopes can not be separated. The consequence of this is that the depth profile of B is shifted and the region close to the substrate appears to be boron-rich, where the surface appears to be boron-depleted. The integral area elemental densities are however correct.
Hydrogen was detected with a semiconductor telescope with a depth resolution of $\sim$ 20nm. Details of the experimental set up and data analysis are given in [153]. In all investigated samples C was present in concentrations $\ll$ 1 at %. Oxygen is present in concentrations $\sim$ 3 at %, but from the profiles it can be seen that it is mainly incorporated at the film substrate interface due to the native Si-oxide layer and on the film surface due to adsorption in air. It was found that hydrogen and in some cases also oxygen are present in high concentrations (up to 8 at %) in boron rich films, in stoichiometric films however,the H and O concentrations are less than 2 at% of the film composition.

7.2.3 Rutherford backscattering spectroscopy

Complementary to ERD analysis heavy element contaminations are identified with Rutherford backscattering spectroscopy (RBS). Here the sample is irradiated with 1.7 MeV He ions and the backscattered primary ions are detected in an semiconductor detector according to their energy. To analyze the obtained data, the spectra are simulated with the RUMP code by Doolittle [154]. The film is modeled to be a layered structure of cBN/hBN/Si with densities of 3.5g/cm^3 and 2.2g/cm^3 for cBN and hBN, respectively and with an B/N ratio of 1. Metal contaminations are mainly Mo, originating from the Mo-substrate holder. All metallic impurities occur in concentrations of less than 1 atomic %. Plass et al. [62] found for IBA deposited films that the Argon distribution is $\sim$ 4at% in the hBN and $\sim$ 2.5at% cBN layer. These results can be reproduced also with the magnetron sputtered samples: here $\sim$ 4.2at% and $\sim$ 2.5at% Ar have been measured in the hBN and cBN layer, respectively.

7.2.4 X-ray absorption near edge spectroscopy

Information about the short range structure of especially light element material can be obtained by x-ray absorption spectroscopy (XAS). Since the XAS spectra originate from a depth max. 10-20 nm below the surface, it is a very sensitive tool for surface analysis. Usually XAS experiments are performed with synchrotron light, since a precise control of the photon energy and a photon current are required. The principle of XAS is shown in figure 7.8. The incident photons have energies in the range of 100 to 1000 eV. Above an energy threshold the photons are absorbed by core level electrons, which promote to unoccupied states in the conduction band. As a result of the absorption, secondary electron and photon emission from the sample occurs. Therefore the absorption coefficient at each incident wave length is proportional to the total photon or electron emission (total yield). The XAS spectrum can be divided in two regions: the near edge region (XANES or NEXAFS), extending $\sim$ 50 eV from the edge and the extended fine structure (EXAFS) between $\sim$ 50 and $\sim$ 1000 eV from the edge. In the near edge range, the position and shape of the absorption edge provide information about the chemical bonding. On the other hand in EXAFS the long range oscillations of the absorption coefficient are used to extract informations about the geometrical structure, in particular the bond length, the bond angle, and the coordination number.

Since XANES allows the study of light element, nanocrystalline or amorphous material, this study was focused on the near edge structure of boron and nitrogen. Specially XANES can give very distinct signatures of sp^2 and sp^3 hybridization.

XANES measurements were performed at the SuperAco synchrotron at the Laboratoire pour L'Utilisation de Rayonnement Electromegnétique (LURE) in Orsay, France. The data were acquired in the total electron yield mode by recording the current drained to the ground from the sample. The intensity was normalized to the simultaneous signal from a gold covered grid located upstream in the x-ray path to compensate photon flux variations coming from the synchrotron ring. The sample was set up in the "magic angle" geometry (55° with respect to the incident beam) to eliminate the angular dependence of the absorption intensity of the π -bonds on the natural horizontal polarization of the synchrotron radiation. For

comparison highly oriented pyrolytic hexagonal boron nitride (HOPBN) and poly-crystalline cubic boron nitride powder were used as reference materials.

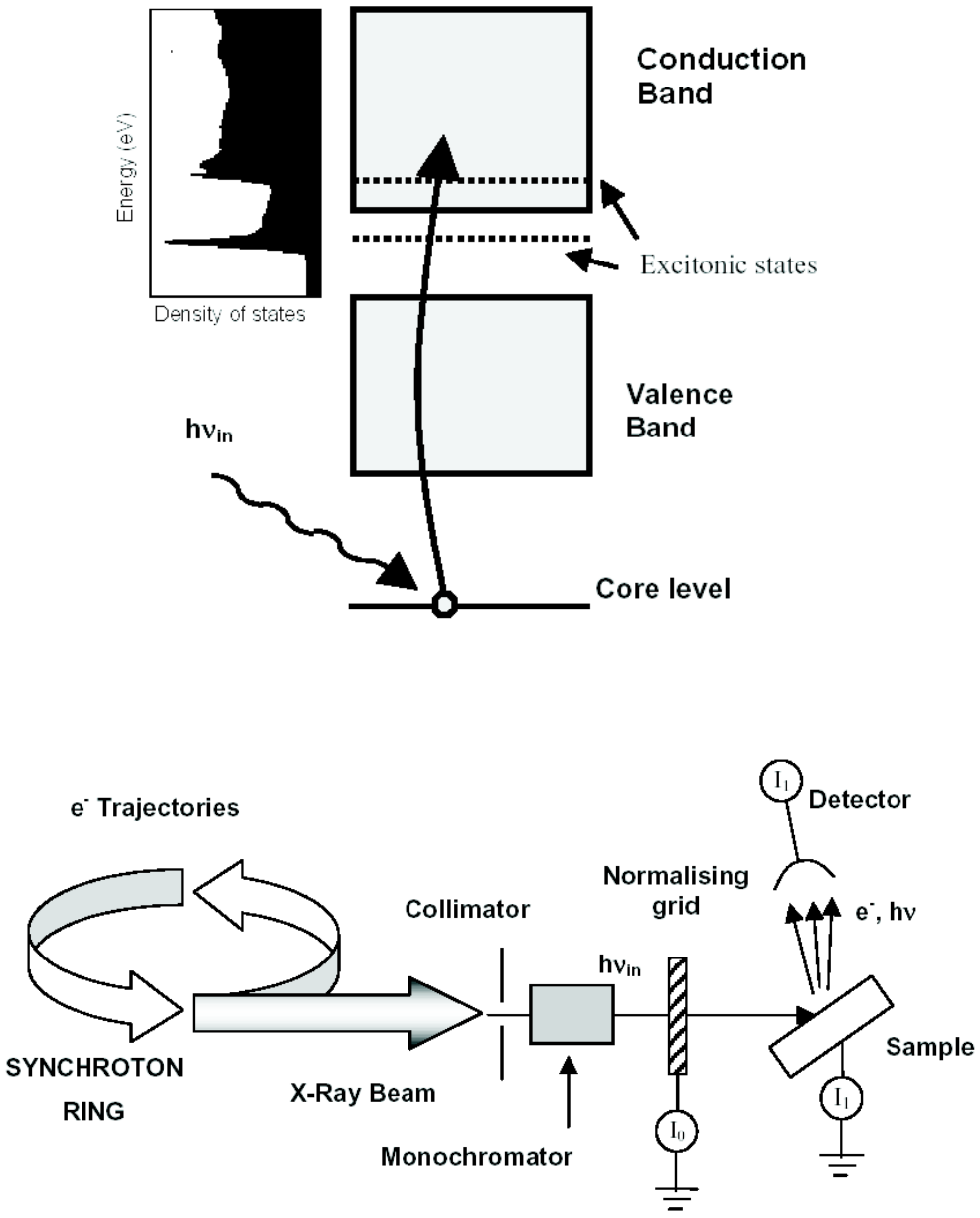

Figure 7.8: Scheme of x-ray absorption spectroscopy and instrumentation for a XAS experiment

7.2.5 X-ray diffraction

Complementary to the stress measurement by cantilever bending, x-ray diffraction experiments were performed. Suitable for the analysis of thin films, grazing incidence diffraction (GID) was used. The x-ray diffraction experiments were carried out at the European Synchrotron Radiation Facility (ESRF) in Grenoble at the Rossendorf Beam Line (ROBL).

The x-ray wave length was $\lambda = 1.2$ Å and the samples were mounted in a six-circle goniometer. The incident beam hit the sample at an angle of 0.2°. In this geometry, the information originates mainly from the surface regions and the signal from the substrate is largely suppressed. The geometry of the GID experiments is shown in figure 7.9.

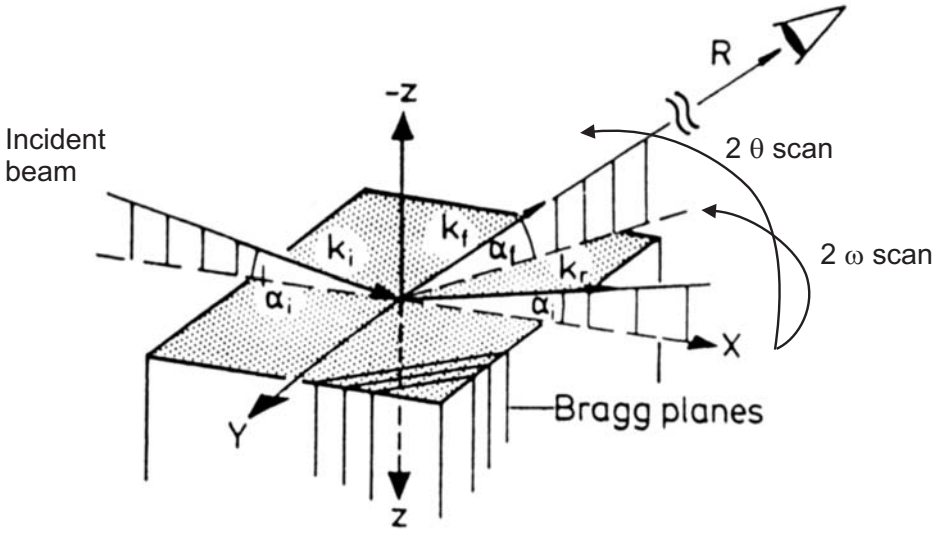

Figure 7.9: Geometry of grazing incidence x-ray diffraction, with α_i= angle of incidence, k_i= incident wave vector, k_r= reflected wave vector, k_f= scattered wave vector, k_i x Z = plane of incidence [155]

The diffracted beams originating from the diffraction at one specific set of lattice planes, lie all on the Debye-Scherrer-cone. In a non-textured and non-strained material, the cross section of the cone is circular and the diffracted intensity is homogeneously distributed. In textured material, the diffracted intensity varies across the Debye-Scherrer-cone according to the orientation of the lattice planes with respect to the plane of incidence. In material under stress, the lattice is strained, i.e. the lattice distances deviate from the equilibrium value. As explained in chapter 3, thin films are biaxially stressed. That means for compressive stress, the spacings between lattice planes parallel to the surface are compressed whereas the spacing perpendicular to the surface is strained, i.e. the Debye-Scherrer-cone becomes ellipsoidal.

In order to be able to detect a biaxial state of stress, 2ω (in plane) and 2θ (out of plane) scans were performed. At 'in plane' geometry, lattice planes oriented perpendicular to the surface are detected, whereas in 'out of plane' geometry the planes parallel to the surface are scanned. The positions of the diffraction peaks are obtained by a fitting procedure using the program PEAKFIT. From the position of the diffraction peaks on the 2ω and 2θ circle, the lattice distances are calculated respectively according to the Bragg law:

$$n\lambda = 2d_{||}sin(\omega) \tag{7.6}$$

$$n\lambda = 2d_{\perp}sin(\theta). \tag{7.7}$$

From the full width at half maximum (FWHM) of the diffraction peaks the coherently diffracting domain size L can be estimated by the empirical Scherrer formula:

$$L = \frac{0.94\lambda}{cos(FWHM)}, \tag{7.8}$$

where FWHM is given in radians.

7.2.6 Transmission electron microscopy

The layered structure and the microstructure of the individual layers were investigated with transmission electron microscopy (TEM). TEM cross sections were prepared by gluing two 5 x 5 mm^2 pieces of the sample with the film face together. This sandwich structure is first mechanically thinned, finally the sample is sputtered with Ar ions of 1 keV at an angle of incidence of 2° (ion milling). The sample preparation is a very time consuming and destructive procedure, therefore only a few selected samples were investigated. A Phillips CM300 microscope operated at 300 keV is used for the investigations. Using electron diffraction hBN and cBN crystallites can be identified according to the hBN (0002) and the cBN (111) lattice spacing.

8 Results and discussion

In the following, the effect of ion bombardment of the growing film is described. In the experiments described here, there are generally two ion energy regimes with different effects on the growing film:

1. low energy regime: Ion energies are in the range of $\sim$ 100-200 eV and are used to enable cBN nucleation and growth. In our case the ions are accelerated by the low voltage dc bias. In this range the plasma potential of about 40 V (see page 39) contributes significantly to the energy of the ions. Ions in this energy range produce high compressive stress in the films (see section 3.3).

2. high energy regime: In the context of this work, the high energy regime comprises ion energies in the order of 1-8 keV. The ions are accelerated by the high voltage bias pulses and serve for the relaxation of the compressive stress.

Approximately 80 % of the nitrogen ions are present in the molecular form. Upon impact, they are dissociated and leave the two N-radicals with slightly less than half of the primary energy (the dissociation energy of $\sim$15 eV is spent).

The effects of the ion bombardment are described and discussed in terms of intrinsic stress and stress relaxation, microstructure, bonding structure and stoichiometry in sections 8.1, 8.2, and 8.3, resp. In section 8.4 the characterization of the near surface zone is described. In section 8.5, the results from sections 8.1 - 8.4 are summarized and interrelations between stress and the microstructure as well as possible stress relaxation mechanisms are discussed. The problem of poor adhesion of the films is addressed in section 8.6 and possible solutions to this problem are suggested there.

8.1 cBN growth

If not stated else in the text, all films have been prepared under the same conditions. For details of the preparation see section 4.2 and table 4.1. The ion and neutral fluxes to the substrate under standard conditions are summarized in table 6.1. The typical layered growth sequence of cubic boron nitride films [9] reflects very well in the evolution of the FPUW and the growth rate throughout the deposition. In figure 8.1, this is demonstrated for a deposition of a 60 nm cBN film, where the low voltage substrate bias was set to -150 V. Figure 8.1a shows the evolution of the FPUW data calculated from cantilever bending, and

fig. 8.1b pictures the film thickness obtained from ellipsometric data, both as a function of the deposition time.

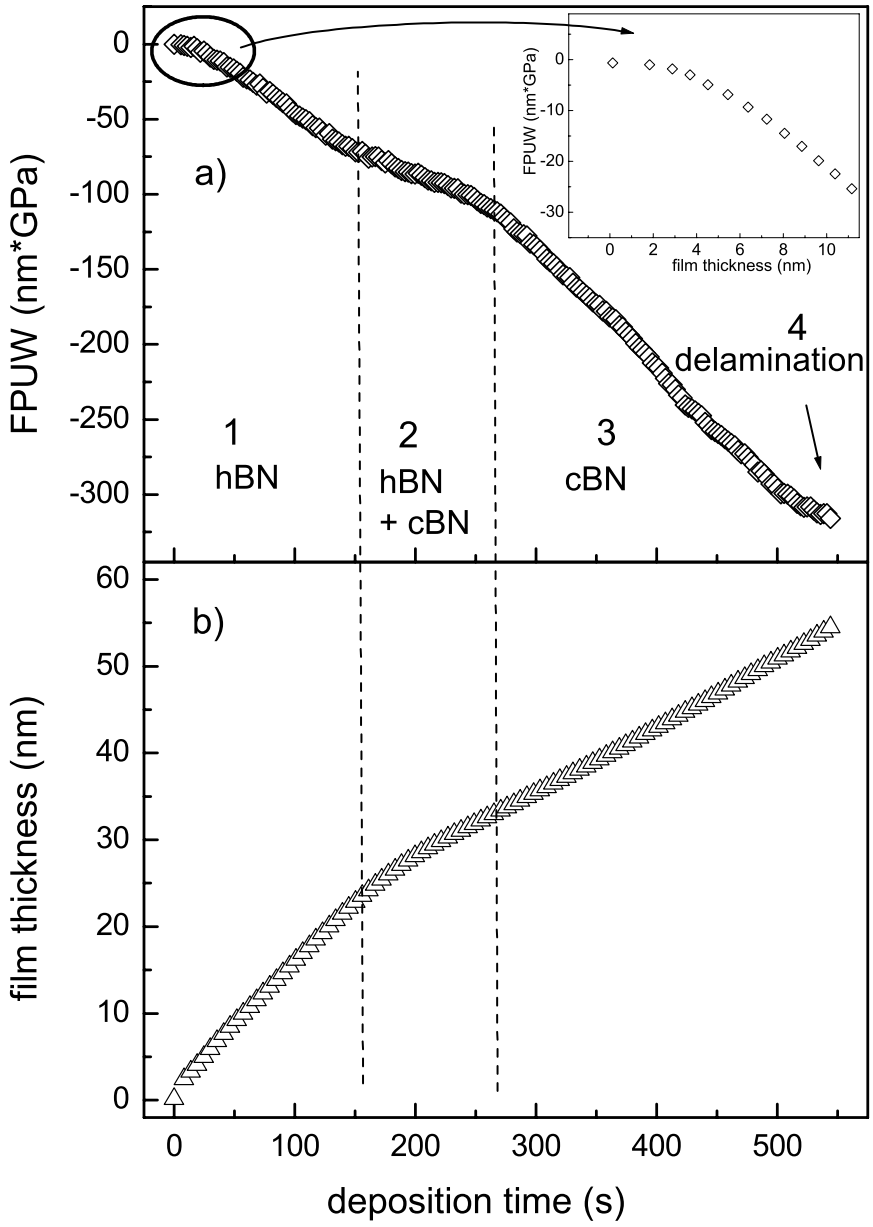

Figure 8.1: Evolution of the FPUW (a) and the film thickness (b) during the deposition of a cBN film. For deposition conditions and plasma parameters see tables 4.1 and 6.1.

As described in section 2.2.4, the layered growth of the BN films consists of 1.) hBN growth (including the formation of an amorphous layer at the interface), 2.) island-type nucleation of cBN and growth of the isolated nuclei until coalescence, and 3.) growth of nearly phase-pure cBN. The three stages are indicated in fig. 8.1.

During the growth of the first 2 or 3 nanometers, as shown in the insert in figure 8.1 (note: here the FPUW is plotted versus the film thickness), the FPUW stays at almost zero. Most likely, this corresponds to the implantation of the ions into the substrate and amorphization of the silicon substrate (see section 2.2.4 and references [9, 78, 79]). Therefore no stress is build up in the initial stage of deposition. The formation of an amorphous layer was detected by in situ Ellipsometry [9] for IBAD using 500 eV Ar ions. In magnetron sputtering, however, the inclusion of an amorphous layer in the optical layer model did not improve the fitting results. Therefore the thickness of such layer is much less than 2 nm.

Further on, during the hBN-growth, both the growth rate and the increase of the FPUW are constant. The beginning of stage 2 is characterized by a decrease of the growth rate and at the same time, the FPUW increases less. The decrease of the growth rate is attributed to the formation of the denser cubic phase and the decrease from 8.5 nm/s to 4.5 nm/s corresponds to an increase of the density from 2.2 to 3.5 g/cm^3. X-ray reflectivity data confirmed that the densities of the hBN and cBN layer are within 90 % of the nominal bulk density. As stage 3 begins, the growth rate is constant again and the slope of the FPUW curve increases sharply. At the end of the deposition time, the slope of the FPUW decreases, indicating the beginning of cracking or delamination of the film.

In order to obtain the instantaneous stress σ from the recorded FPUW and film thickness data, the FPUW is plotted as a function of the film thickness, as shown in figure 8.2. With eq.3.7 on page 18, σ is the first derivative of the FPUW with respect to the film thickness. To obtain a useful and informative numerical derivation, a very low noise level of the data would be required.

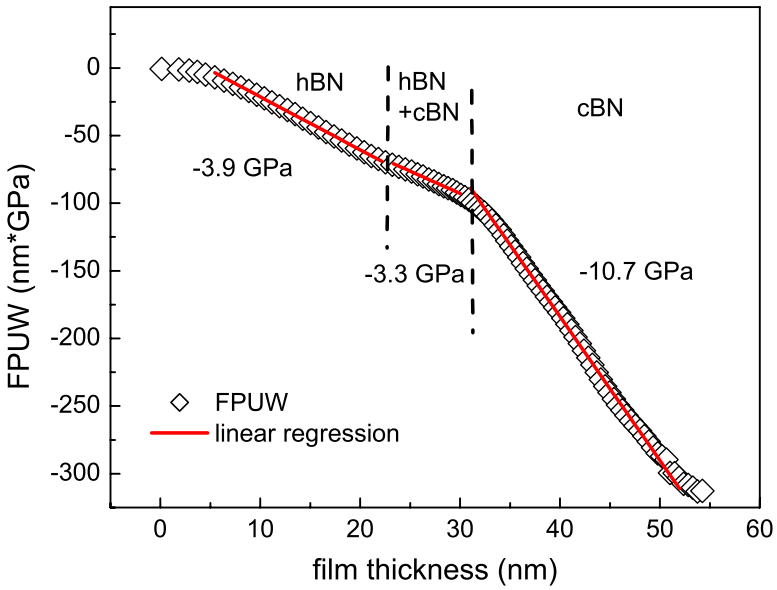

Figure 8.2: FPUW recorded during the deposition of a cBN film as function of the film thickness (open diamonds) and regression lines (straight lines), from whose slopes the instantaneous stress is obtained. For deposition conditions and plasma parameters see tables 4.1 and 6.1.

Since however, the FPUW increases linearly with the film thickness (after cBN coalescence and without any parameter changes) linear regressions are used to analyze the evolution of σ. In the remainder, when the FPUW vs d_f curve is discussed for different experiments, the instantaneous stress σ always refers to $\frac{d(FPUW)}{d(d_f)}$ obtained from linear regressions at the point of deposition indicated.

In figure 8.2 linear regression were fitted to the particular sections of the FPUW curve. As indicated in the figure, the instantaneous stress in the hBN is -3.9 GPa , slightly decreases in the cBN nucleation stage (-3.3 GPa), and increases sharply to -10.7 GPa when the nuclei have coalesced. This results are in agreement with the model of a cBN nucleation in the subsurface region, since the formation of the denser cubic phase below the surface is accompanied by a volume decrease and hence a reduction of compressive stress in the surrounding hBN. During this nucleation stage the compressive stress in the cBN grains can be compensated, since the surrounding compliant hBN allows an expansion of the cBN grains. After complete cBN coalescence, an expansion is inhibited by the neighbouring cBN grains resulting in the observed sharp increase of σ.

This sharp increase of σ enables the determination of the point of completed cBN nucleation in real time. Although the evolution of the FPUW is very characteristic, the absolute values of σ vary between -2 and -4 GPa in hBN and -8 to -11 GPa in cBN. These variations are mainly attributed to changes in the thickness of the hBN layer (but also orientation and curvature of the hBN planes, the conditions at the substrate interface, impurities etc.), since the microstructural features determine the elastic properties of the film. This typical evolution of σ during the deposition of an hBN/cBN layered structure confirms the results obtained previously by IBAD experiments [52].

8.2 Stress relaxation

In this section the effect of high energy ion bombardment on the instantaneous stress σ of the growing film is described and analyzed. As shown in the experimental section 4.2 on page 26 the high energy ion bombardment is realized by a pulsed high voltage bias that is combined with the usual growth assisting low voltage bias. The evolution of σ is investigated in terms of ion energy and ion flux, which are controlled by the pulse voltage and the pulse duty cycle. In the experiments described here, the pulse voltage and duty cycle range from 2 - 8 kV and 0.3 to 1.2 %, respectively. The low voltage bias consisted always of sequences of -150 V(80 μs) followed by +80 V(3 μs) as described in section 4.2.

Eyhusen et al. [42] found that the hBN/cBN interface is unstable against energetic ion bombardment for energies $\geq$ 2.5 keV and cBN is transformed back to hBN. Therefore, before starting the high voltage pulses, 20 nm cBN have been grown at a bias voltage of -150 V after the nucleation and grain coalescence. Since the mean projected ion range for 8 keV Ar ions (highest energy used in the experiments) is $\sim$7 nm and replacement collisions occur up to $\sim$15 nm depth (see chapter 5), 20 nm cBN should be sufficient to protect the hBN/cBN interface[1].

[1]The range of N ions is higher (R_p= 13 nm) but cBN and the cBN/hBN interface are more tolerant to N ion impact. Also the atomic nitrogen ion makes up for $<$ 10 % of the total ion flux

As an example for ion-induced stress relaxation, the evolution of the FPUW during a deposition experiment with high voltage pulses of 8 kV and a duty cycle of 0.6% is shown in figure 8.3. While the growth of the hBN interlayer, nucleation, and coalescence of cBN, the evolution of the FPUW resembles qualitatively the results shown in Fig. 8.2. Upon starting the high voltage pulses the FPUW decreases immediately. After a few nanometer growth the sign of the curve changes again and, the FPUW increases further linearly resulting in an instantaneous stress of -1.1 GPa.

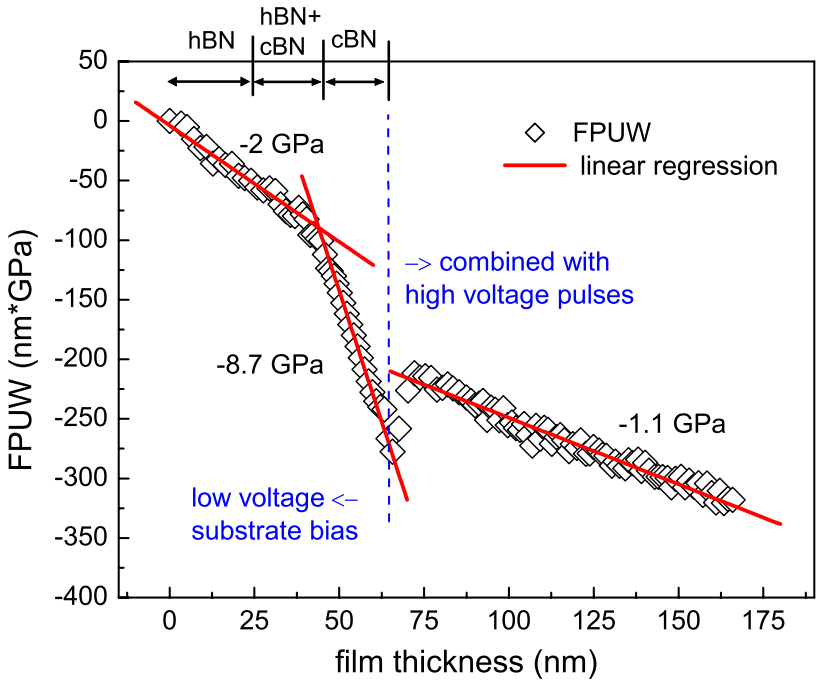

Figure 8.3: FPUW recorded during the deposition of a cBN film with simultaneous high energy ion bombardment as function of the film thickness (open diamonds) and regression lines (straight lines). The bias pulse were set to -8 kV with a duty cycle of 0.6%. For deposition conditions and plasma parameters see tables 4.1 and 6.1.

The positive slope of the FPUW curve in the first few nm growth after the onset of the HV pulses would indicate a tensile stress. However, the decrease of the FPUW can not be interpreted as such. Since the ion bombardment affects material, which is already grown, it should be seen as the relaxation of stress below the surface, so that eq. 3.7 cannot be applied in this range. Thermal stresses due to heating by the high energy ion bombardment are not likely to produce the release of the FPUW, since the additional heating power is negligible (see section 4.2). In addition the thermal expansion coefficient α of the Si substrate is slightly smaller than that of cBN and an increase of the temperature would result in additional compressive stress [2].

In figure 8.4 the width of that part of the FPUW curve with $\frac{dFPUW}{dd_f} \geq 0$ is plotted

[2] with $\alpha_{Si} \approx 4 \cdot 10^{-6} K^{-1}$ (at deposition temperatures of $\sim 400°C$ [156]) , $\alpha_{cBN} = 5 \cdot 10^{-6} K^{-1}$ and $E/(1-\nu) \approx 800\ GPa$ [157] the thermal stress induced by a temperature increase of 100°C would be around - 0.08 GPa

together with the mean projected ranges of Ar, N_2, and N ions (calculated with SRIM) as a function of the pulse voltage (at different duty cycles). The error bars result from uncertainties in the turning points of the FPUW vs. d_f curve. It becomes clear that the width of this region is increasing with the pulse voltage and hence the ion energy. Further it can be seen that the extent of $\frac{dFPUW}{dd_f} \geq 0$ in depth is correlated with the mean projected ion range.

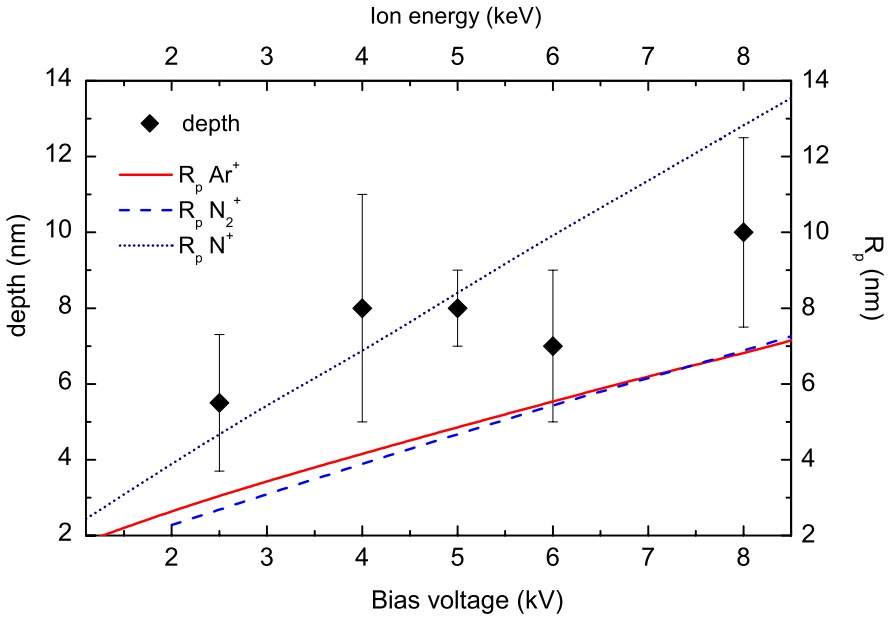

Figure 8.4: Width of that part of the FPUW curve with $\frac{dFPUW}{dd_f} \geq 0$ as a function of the pulse voltage (diamonds). The lines show the mean projected ion range as a function of the ion energy obtained from SRIM of Ar^+(solid line), N_2^+(dashed line), and the atomic N^+(dotted line). Note: R_p of N_2^+ is considered to be equal to R_p of N^+ at half the energy.

Considering the dynamic evolution of the damage profile (see section 5), it becomes clear that the release of the FPUW ($\frac{dFPUW}{dd_f} \geq 0$) happens until the bulk damage value is reached, i.e. when the film has overgrown the thickness of the mean projected ion range. Until this point, the damage is accumulating in the subsurface region and thereby, more and more stress is released. This means that here the stress is released at a higher rate in the depth than the stress is newly formed in the surface region. Finally, the level of the stationary bulk damage is reached and a balance between compression in the surface region by the low energy ions and relaxation below the surface by the high energy ion impact is established, resulting in the further steady increase of the FPUW curve.

As already mentioned the cBN/hBN interface is not stable upon ion bombardment and the stress relaxation can be applied only when sufficient cBN has been grown and the high energy ions cannot penetrated to the hBN/cBN interface. The consequences of this restriction are:

1. the underlying hBN and the cBN nucleation layer remain stressed.

2. the late onset of the stress relaxation leads to stress gradients over the film which causes curling and delamination of the film.

By using ions with a lower energy for the stress relaxation (as low as possible), the thickness of the untreated cBN could be reduced. The deposition of multilayer structures of hBN and low-stress cBN could also offer a solution to this problem in the sense that the more compliant hBN can compensate some amount of the remaining stress and in this way reduce the stress gradient over the total film thickness.

The instantaneous stress that was measured as a results of film growth under low energy ion bombardment and relaxation under high energy ion bombardment, is summarized in table 8.1 for different pulse voltages and duty cycles. All samples were produced with a 50 nm thick hBN buffer layer (see section 8.6), a $\sim$ 20 nm cBN nucleation layer and $\sim$ 150 nm growth under HV pulses. In all samples the instantaneous stress in the cBN nucleation layer before the on set of the HV pulses was between -8 and -9 GPa.

Table 8.1: Calculated stationary bulk damage and measured instantaneous stress for different ion bombardment conditions. The errors arise from the quality of the regression and the noise level of the data.

pulse voltage (kV)	duty cycle	stationary bulk damage (dpa)	instantaneous stress (GPa)	Error (GPa)
-8	0.6%	1.2	-1.6	$\pm$ 0.1
-8	0.6%	1.2	-1.9	$\pm$ 0.25
-6	0.6%	0.9	-1.6	$\pm$ 0.13
-2.5	1.2 %	0.7	-1.8	$\pm$ 0.1
-4	0.6%	0.69	-1.7	$\pm$ 0.1
-8	0.3%	0.6	-2	$\pm$ 0.25
-4	0.3%	0.34	-4.3	$\pm$ 0.5

The degree of stress relaxation increases with both the pulse voltage and the pulse duty cycle, leading to the conclusion that not only the ion energy but also the ion dose plays an important role in the relaxation process. This can be expressed by the stationary damage values for the different ion bombardment conditions (for the calculation of the damage see chapter 5), which are given in table 8.1. In figure 8.5 the stress values are shown as a function of the high energy ion induced damage.

It can be seen that the instantaneous stress in the films decreases with increasing damage. That means that the relaxation of stress is enhanced by an increasing number of atomic rearrangements. But, when the number of dpa is exceeding a certain level (around 0.8 dpa), no further stress relaxation can be achieved under these deposition conditions and the stress vs. dpa curve reaches a plateau. It is important to note that the same stress relaxation can

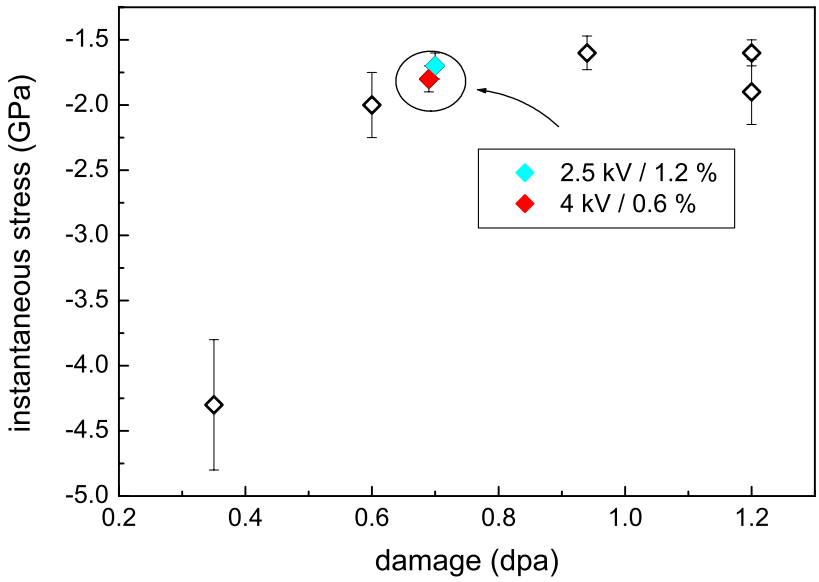

Figure 8.5: Instantaneous stress measured during cBN deposition with additional energetic ion bombardment as a function of the ion induced stationary bulk damage. For deposition conditions and plasma parameters see tables 4.1 and 6.1.

be achieved with different ion energies if the same damage is introduced by the energetic ion implantation, i.e. if the duty cycle is adjusted accordingly.

This is an important result if pulsed substrate voltages are to be used for stress relaxation in commercial processes, since power supplies operating in the few kV- range can be easily integrated into large scale coating systems and are cost efficient. Using a lower ion energy also allows to start earlier with the high voltage pulses, i.e. closer to the cBN/hBN interface, since the mean projected range of the ions is decreased (see figure 8.4). In this way the part of the film which remains unrelaxed can be minimized.

Results of ion induced stress relaxation during filtered arc deposition of carbon, TiN, and AlN films have shown a comparable dependence on the product of the pulsed bias voltage (2-20 kV) and pulsing frequency [118, 158], indicating a dependence of the stress relaxation on ion energy and ion flux as in the results reported here. In all three materials the resulting compressive stress could be described with a power function $S = -(V \cdot f)^{-2/3}$, where V and f are the voltage and the frequency of the substrate bias pulses. This power law, however, does not describe the stress relaxation in the cBN films. A reason might be that in BN a phase transformation could be induced by the energetic ions. Then the measured stress would not only be the result of relaxation in the cBN. With a phase transformation to hBN the elastic properties would change and in consequence the measured stress would change even though the strain might still be the same. This will be discussed in section 8.3.

8.2.1 Comparison with results from x-ray diffraction

The measurement of the substrate curvature yields the film stress on a macroscopic scale, even if it is measured depth resolved. In order to study the stress relaxation on microscopic scale, the cantilever bending measurements were complemented by grazing incidence diffraction (GID). The measured samples include one reference sample that was grown without stress relaxation, three samples with different degree of stress relaxation, and one sample that was grown with simultaneous ion bombardment inducing 1.2 dpa and that was annealed after the deposition at 900°C. In this sample most of the residual stress should be eliminated due to the fact that above 600°C plastic deformation occurs in the silicon substrate. The relaxation conditions, the resulting stationary damage and the stresses measured by cantilever bending are summarized in table 8.2.

Table 8.2: Calculated stationary bulk damage and measured instantaneous stress for different ion bombardment conditions of the samples used for GID. (*): This sample was prepared in a 100% N_2 discharge at 0.1 Pa and 250 W discharge power, the ion flux ($N_2^+ + N^+$) was 7.8 ions/cm^{2}s

pulse voltage (kV)	duty cycle	stationary bulk damage (dpa)	instantaneous stress (GPa)	Comments
-	-	-	-9 GPa	non relaxed cBN
-8	0.3	0.5	-2.6 ± 0.1 GPa	N ions only *
-4	0.6	0.7	-1.7 ± 0.1 GPa	Ar^+/N_2^+
-8	0.6	1.2	-1.6 ± 0.1 GPa	Ar^+/N_2^+
-8	0.6	1.2	-	annealed (900°C); fully released cBN

For each sample in-plane (2ω) and out-of plane (2θ) scans were performed, which allows to map the biaxial state of stress in the films, since lattice planes that are oriented parallel and perpendicular to the surface can be detected. The recorded in-plane and out-of-plane diffraction patterns are shown in figure 8.6a and b, respectively. The cBN layer in the non-relaxed film was only 30 nm to prevent delamination before the measurement was finished. Therefore the scattered intensity is very low, and due to texture the (111) diffraction peak in the in-plane geometry is very weak as can be seen in the enlarged spectrum in figure 8.6a. In consequence the error in the fitted cBN peak position is large. Due to the texture of hBN with the c axis oriented parallel to the surface, the hBN (0002) diffraction peak cannot be detected in the out-of-plane geometry.

The d_{111} values obtained from a peak fitting procedure are summarized in figure 8.7. For comparison, the d_{111} lattice spacing of poly crystalline cBN is given as well [159].

The lattice spacings are larger in the out-of-plane than in in-plane direction, indicating a pronounced compressive biaxial state of stress. Only the annealed sample shows isotropic lattice spacings with equal in-plane and out-of-plane values, which confirms a complete

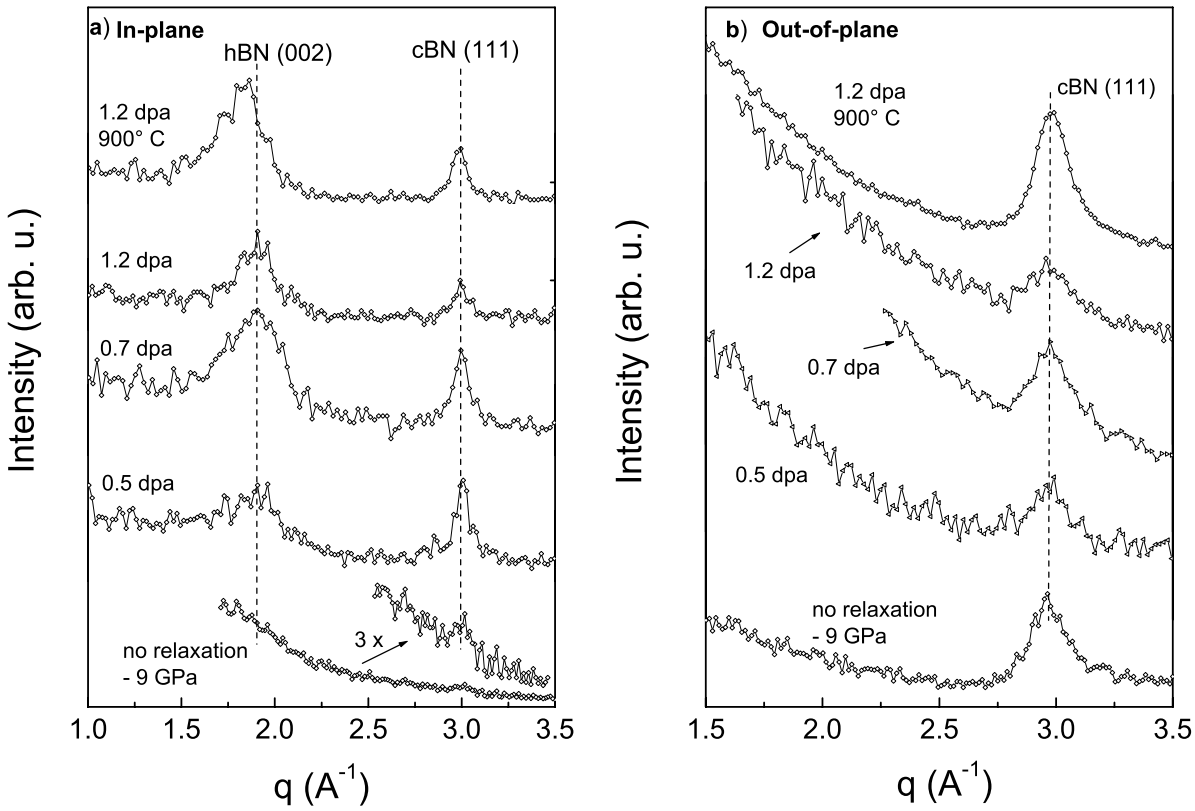

Figure 8.6: XRD patterns as a function of the momentum transfer of cBN samples grown under different ion bombardment parameters resulting in different degrees of stress relaxation. The annealed sample (900°C) is regarded as a reference for a fully released cBN film. The in-plane scans are shown in panel a) and the out-of-plane scans are presented in panel b).

relaxation of the in-plane stress. Even with the presence of compressive stress, the in-plane d(111) values of all samples are larger than the powder reference value. This is most likely due to the nanocrystalline structure and incorporation of defects as a result of the deposition process. With increasing ion induced damage the in-plane and out-of-plane lattice spacings converge towards the value of the annealed sample. This is a clear signature of strain relaxation within the cBN grains.

Taking the d_{111} value of the annealed sample as reference for a non stressed nano crystalline cBN, the residual strain in the other samples can be calculated. To calculated the stress the elastic modulus and the Poissons ratio have to be known. Using the values for E and ν given in reference [157], $E/(1-\nu) \approx 800$ GPa, the residual stress parallel to the surface in the sample irradiated with 8 keV Ar and N_2^+ ions (with 1.2 dpa) would be 2.8 GPa. Reliable data of elastic constants are available only for single crystal cBN, in thin films, the cBN should be more compliant due to defects and poor crystallinity [160] and hence the residual stress should be lower, which is in agreement with table 8.2.

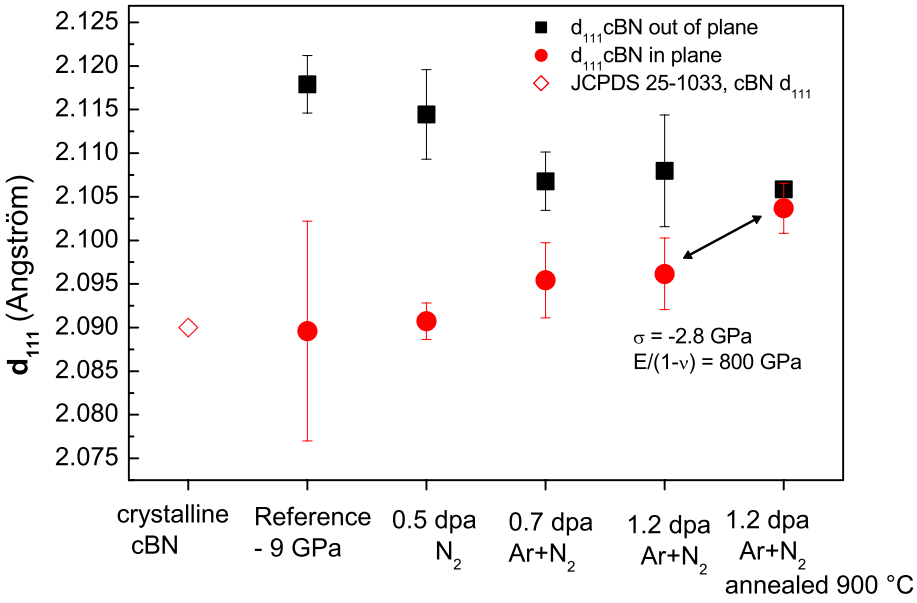

Figure 8.7: d_{111} lattice spacings in in-plane and out-of-plane direction for cBN samples with different state of intrinsic stress obtained from peak fitting of the diffraction patterns shown in fig. 8.6. The value for polycrystalline cBN is taken from [159].

8.2.2 Effect of low voltage substrate bias on film stress

In this section the effect of the low energy ion bombardment, i.e. the cBN forming ions is investigated, since ions in this energy range are responsible for the formation of compressive stress. It was not possible to investigate the effect of the low energy ions without stress relaxation, since the samples delaminated in situ or the results were not reproducible due to varying thickness of the underlying hBN nucleation layer. Therefore, the films were all deposited in the following order: 50 nm hBN buffer layer, a $\sim$ 20 nm cBN nucleation layer

and $\sim$ 150 nm cBN growth under pulses of -8kV and 0.3% duty cycle. The cBN nucleation took place at -180 V for all samples. With the starting of the HV pulses, the low voltage substrate bias was changed to values between -150 and -90 V. Using a bias voltage of -180 V results in a very high resputter rate of the cBN films and a significant reduction of the growth rate.

In Figure 8.8 the instantaneous stress that was measured during the growth under simultaneous stress relaxation is shown as a function of the low voltage substrate bias. The dashed line is used as a guide for the eye. One can see that σ is low at high substrate bias. At $\sim$ -120 V the stress reaches a maximum and decreases again to lower voltages. Since the relaxation of the stress should be equal in all samples, it is concluded that at a bias voltage of -120 V (the actual ion energy is some 20 eV higher) a maximum of compression is build into the films. The data are qualitatively in agreement with the Davis model. This means that at a bias voltage of -120 V the highest concentration of defects is produced. At lower bias voltage less defects are produced and at higher voltages a part of the defects are already annealed in thermal spikes.

The model of Davis comprises ion energies between 0 and more than 600 eV, and the data points shown here lie within a very narrow range of the Davis curve, just about the maximum, which is insufficient for a satisfactory fit of equation 3.9 to the data.

The data point at -90 V should be regarded with care, since in this sample the cBN content is lower than in the other samples (see below). Due to a voltage drop that occurs across the insulating film (see section 4.2), the final ion energy at this low substrate bias was probably already too low to sustain the cBN growth.

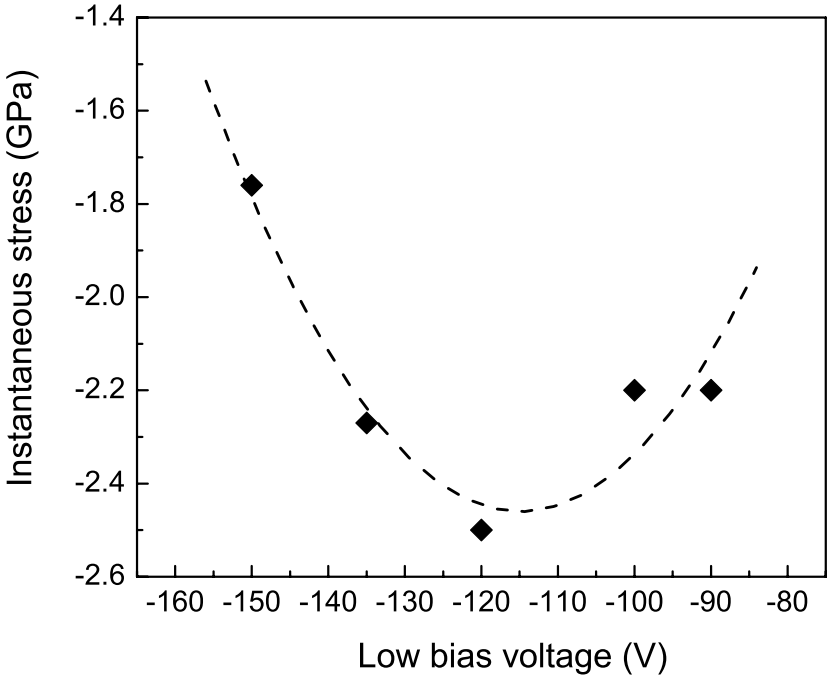

Figure 8.8: Instantaneous stress measured during cBN deposition with additional energetic ion bombardment as a function of the low voltage substrate bias (diamonds). The dashed line serves as a guide for the eye. The high voltage pulses were set to -8 kV/0.6 %. For deposition conditions and plasma parameters see tables 4.1 and 6.1.

8.3 Microstructure and bonding characteristics

In this section the effect of the ion bombardment on the micro- and bonding structure of the films is investigated. Especially the question is discussed, whether the observed stress release is related with strain release in the cBN or if it is caused by a transformation of the cubic structure to the more compliant hBN structure.

8.3.1 Effects of high energy ions

The total cBN content in the film is measured by infrared spectroscopy. In Figure 8.9 the FTIR spectra of the samples corresponding to the data points a) 0.6, b) 0.9, and c) 1.2 dpa out of figure 8.5 are shown. From the ratio of the peak intensities at 1400 cm^{-1} and 1090 cm^{-1} the cBN content was estimated to be approximately 65% in sample (a), 45% in sample (b), and 33% in sample (c). It has to be considered that the hBN buffer layer is 50 nm thick in all three samples and contributes to the peak intensity of the stretching mode with approximately 20% (for a total film thickness of 230 nm). This leads to the conclusion, that a phase transformation of cBN to hBN takes place in a considerable amount if the damage due to ion bombardment exceeds 0.8 dpa and becomes more pronounced with a further increase of the number of atomic displacements. If the damage is below this value, the transformation to hBN takes place at very low rates.

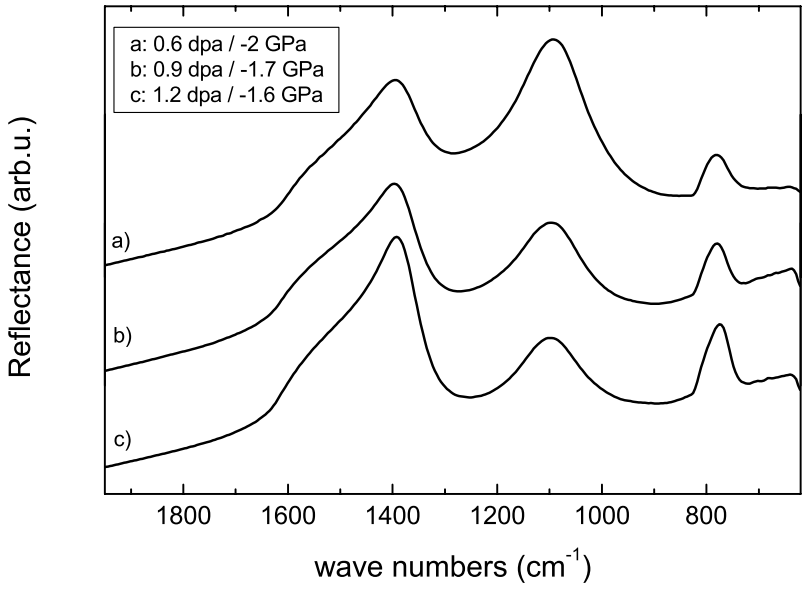

Figure 8.9: IR spectra of cBN films grown with pulsed high voltage substrate bias. The corresponding ion-induced stationary damages were a): 0.6 dpa, b): 0.9 dpa, and c): 1.2 dpa. All samples have a total film thickness of 230 nm including a 50 nm hBN, 20 nm cBN nucleation layer, and 150 nm cBN grown under HV pulses. For the settings of the pulsed bias voltage and the resulting instantaneous stress see table 8.1. For deposition conditions and plasma parameters see tables 4.1 and 6.1.

Comparing the cBN content in the films with the stress relaxation as shown in figure 8.5, one can see that in the 'low damage range' where the relaxation increases with the number of dpa the transformation rate to hBN is low. On the other hand in the 'high damage range' where no further stress relaxation could be achieved with increasing the number of dpa, an increasing hBN content is observed. From this result, the conclusion is drawn that in the 'low damage range' in fact strain is released within the cBN. If more than ~ 0.8 dpa are induced, an enhanced transformation from cBN to hBN takes place instead of a further strain release.

These findings are not in agreement with the findings in reference [42], where cBN was observed to remain stable in post deposition ion implantation experiments with Ar ions of 30 keV energy and fluences up to 10^{15} ions/cm^2 (corresponding to a damage of 2.5 dpa). However as mentioned in this reference, not only the hBN/cBN interface is unstable upon ion impact, but also a high amount of hBN on the cBN grain boundaries and in-between the grains (which basically resembles an hBN/cBN interface) can lead to a pronounced instability of cBN under ion irradiation. The sp^2 bonded surface layer represents an hBN/cBN interface as well. In dynamic ion bombardment with 8 keV ions this 'surface-interface' might be more critical than it is in 30 keV post deposition implantation, since much more rearrangement processes take place close to the surface.

From the empirical Scherrer formula (equation 7.8), an average size of coherently scattering domains can be calculated from the FWHM of the XRD peaks. For the investigated samples, this shows that the cBN grain dimensions are ~ 6 nm and 3-4 nm in directions parallel and perpendicular to the surface, respectively. The hBN domain size is around 2 nm in all samples (along the c axis and in the direction parallel to the surface). These domain sizes do not change due to ion bombardment, annealing or delamination of the film. In other words this means that although an increased hBN content is observed with increasing ion damage, the domains of ordered cBN are not decreased in their size. A possible explanation might be the presence of sp^3 bonded material with only short range ordering located in between the grains, which is preferably transformed to hBN already at rather low ion damage.

The cross sectional TEM micrograph in figure 8.10 shows an image of a cBN film grown with simultaneous stress relaxation. The white lines indicate the direction parallel to the surface. The upper left part of the image shows the hBN buffer layer, clearly identified by the elongated hexagonal basal planes oriented perpendicular to the surface. The middle part shows the cBN nucleation layer. Here the structure is dense and no hexagonal planes can be found. The on set of the high voltage pulses is marked by a bright stripe parallel to the surface. This stripe is also visible in lower magnifications and stretches along the whole sample. The brightness indicates a lower density, although there is no disruption. In some places lattice planes extending across this bright line are visible. In the lower right part the film was grown including high energy ion bombardment. Here areas with cBN structure as well as with hBN basal planes are mixed. In this part of the sample the hBN planes do not show a preferred orientation and some are slightly curved. The TEM image of the part of the film grown under high energy ion irradiation is generally more bright than the cBN-nucleation part and gives only very scarce evidence of crystalline material. This would confirm an ion induced phase transformation but could be also an artifact from the sample preparation.

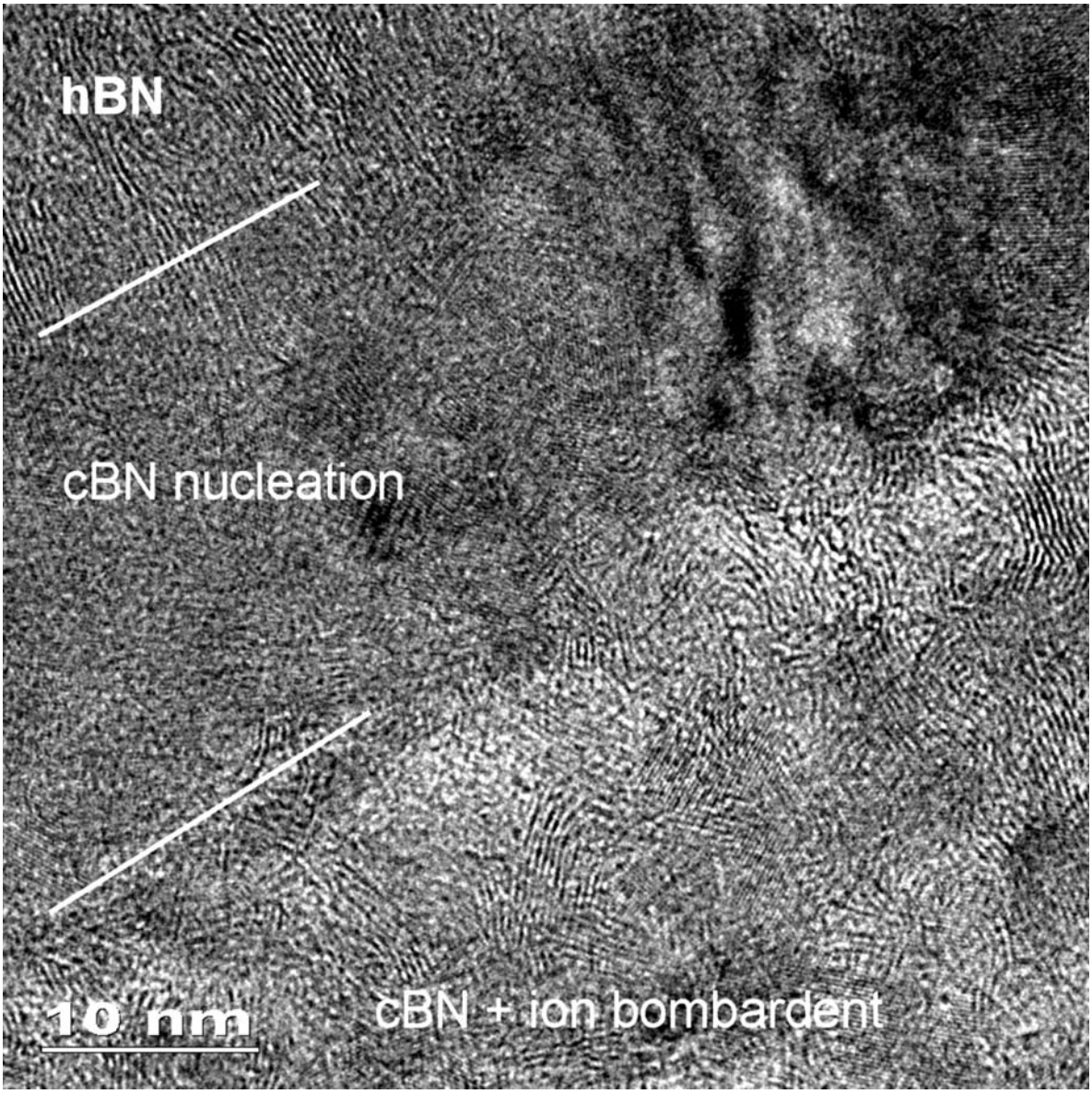

Figure 8.10: TEM cross section of a cBN film grown with simultaneous stress relaxation. The pulse voltage and duty cycle were 8 kV and 0.6%, respectively. The white lines indicate the direction parallel to the surface. Upper left corner: hBN buffer layer, middle part: cBN nucleation layer, lower right part: cBN grown with simultaneous stress relaxation.

8.3.2 Effects of low energy ions

The effect of the low energy ions on the bonding structure is investigated in figure 8.11. The FTIR spectra correspond to the samples that were analyzed in section 8.2.2 and figure 8.8 (see page 69). As described there, the cBN was nucleated on top of a 50 nm hBN buffer layer and after cBN grain coalescence, the deposition was continued with pulsed bias of 8 kV and a duty cycle of 0.3% for all samples. At the same time the low bias voltage was reduced. The values were chosen between -90 and -150 V as indicated at the corresponding FTIR spectra. From the area ratio of the cBN Restrahlen region and the hBN stretching mode the cBN fraction was calculated. With decreasing bias voltage the cBN content increases from 61% to 73%. For the given layer structure, this means that at -100 V the top layer consist of almost 100% cBN. At the same time as the cBN content increases also the growth rate increases from 7.1 to 8.6 nm/min. Since the increase of the growth rate is not due to an increased hBN content it is accounted to a lower sputter rate. An estimation of the sputter rate by TRIM (for 1.5 ions/cm^{2}s $Ar^+ + N_2^+$) gives $\sim 3 \cdot 10^{13}$ atoms/cm^{2}s at -100 V and $\sim 1.2 \cdot 10^{14}$ atoms/cm^{2}s at -200 V. Therefore it is suggested that a high sputter yield favors the growth of hBN although the ion energy and ion to neutral ratio are within the cBN growth conditions.

Comparing these data with the stress measured in these samples (figure 8.8), another important conclusion is drawn: obviously the cBN content in the layer is not correlated with the amount of stress. That means that a relaxation of the stress can be achieved within the cBN and the formation of highly hexagonal layers due to the ion bombardment can be avoided.

8.3.3 Effect of ion species: Argon and Nitrogen

From previous results [13] it is known that 35 keV Ar ion implantation during IBA deposition of cBN films leads to a non-stoichiometric boron-rich film. Also in MSIBAD experiments [42] it could be shown that cBN is more degraded due to Ar ion bombardment than by N ions in energy range of 20 to 30 keV.

The changes of the microstructure due to Ar ion implantation are investigated by comparing film growth and stress relaxation in a 100% N_2 discharge with that in the common Ar/N_2 discharge as in the previous experiments. Two films have been prepared with approximately the same thickness of about 400 nm with an hBN buffer layer of 120 nm. For the stress relaxation after cBN nucleation the voltage and the duty cycle of the substrate bias pulses were 5 keV/0.6% and 8 kV/0.6% in the Ar/N_2 and in the N_2 discharge respectively. Resulting damage values are 0.55 for Ar/N_2 sample and 0.6 for the N_2 sample (Note: for the damage calculation the actual growth rates were considered since for the nitrogen discharge it is only 60 % compared to the Ar/N_2 mixture). The measured instantaneous stress was -1.6 GPa and -1.8 GPa in the Ar/N_2 sample and the N_2 sample, respectively. The resulting bonding structures are compared in figure 8.12.

It is obvious that in the case of a pure nitrogen discharge (sample b), the cBN content of the film is significantly higher than for sample a. Due to the transparency of the film, the reflectance intensity in the infrared spectrum results from reflection at the film and at the

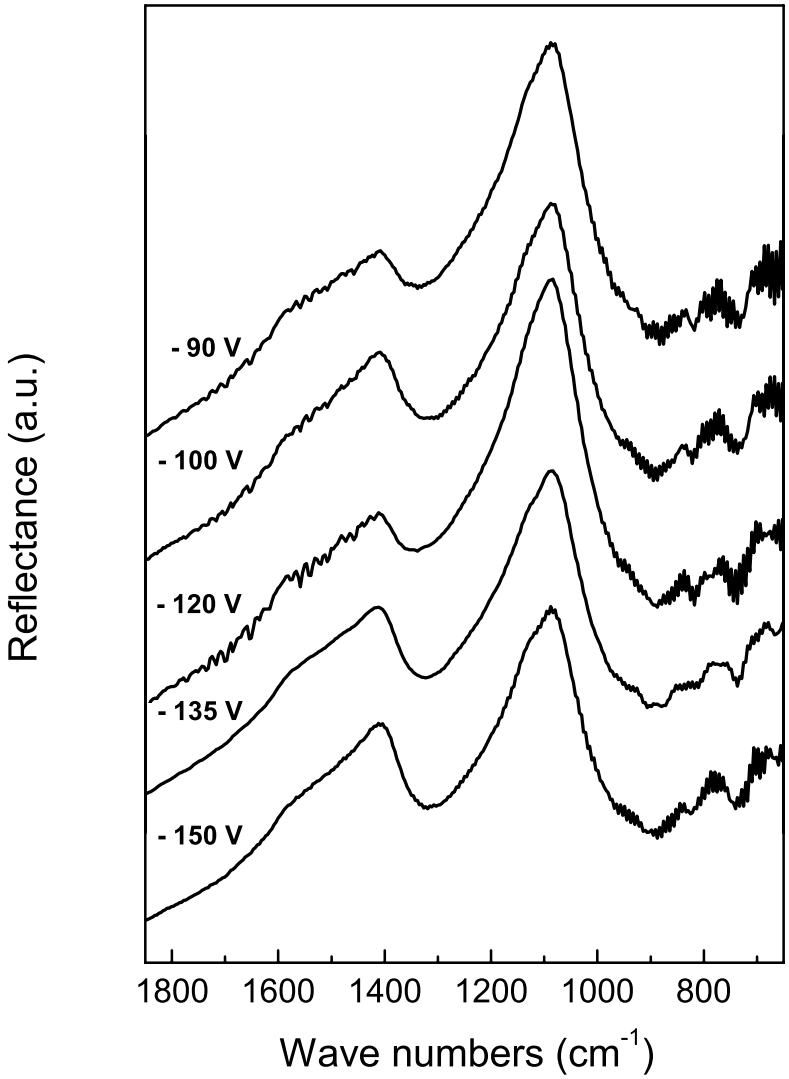

Figure 8.11: IR spectra of cBN films grown with pulsed high voltage substrate bias set to -8 kV and a duty cycle of 0.3 %. The stationary damage induced by the high energy ions is 0.6 dpa. The low voltage negative substrate bias was varied between -90 and -150 V. For all other deposition conditions and plasma parameters see tables 4.1 and 6.1.

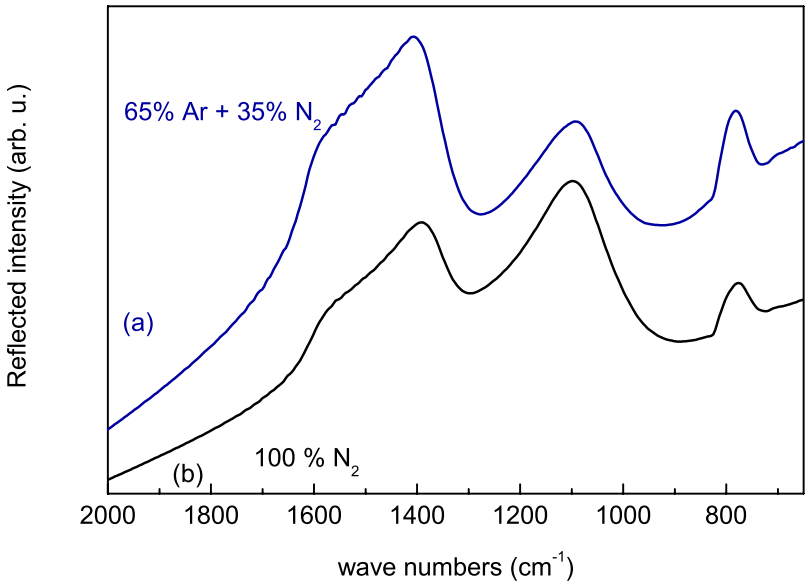

Figure 8.12: IR spectra of stress released cBN films grown with pulsed high voltage substrate bias, in a)Ar/N_2 and b)N_2 plasma. The pulse voltage and duty cycles were adjusted to result in a stationary damage of a) 0.55 dpa and b) 0.6 dpa (see text).

substrate. Due to the large film thickness this leads to interference minima and maxima in the spectrum and the exact evaluation of the cBN content from the IR spectrum becomes difficult.
There might be different reasons for the enhanced instability of cBN under Ar ion bombardment. As shown in reference [13], the Ar^+ bombardment leads to a nitrogen deficiency, which could favor the formation of sp^2 bonds within the collision cascades. Also, impact of Ar ions induces a higher sputter rate at the film surface. As suggested in section 8.3.2, this could lead as well to an increased hBN content of the films.

Finally, it has to be noted that in our magnetron sputter process the assistance of Ar ions is not needed for the cBN nucleation nor for the successful stress relaxation. But it has to be considered that using only nitrogen as working gas leads to significantly lower sputter rates at the target and hence to lower growth rates. Second, due to the dissociation of the N_2^+ ions upon impact on the film surface, the substrate bias voltage has to be doubled to maintain the required ion energy. The low voltage power supply that is used in this set up has an upper limit of -200 V. In the case of cBN growth on top of a thick hBN buffer layer, -200 V might not be sufficient to initiate cBN nucleation.

8.4 Analysis of the near surface region

The stress that is measured by the cantilever bending method as well as the structural information obtained by infrared spectroscopy are representative for the bulk of the films.

In the process of stress relaxation by simultaneous ion bombardment, however, the near surface region undergoes less displacement collisions than the material in the bulk (see figure 5.2). This should lead to a different state of stress and microstructure in the top 10 to 15 nm. Therefore low stress cBN films have been investigated by x-ray absorption near edge spectroscopy (XANES), which is very sensitive to the bonding structure near the surface of light element materials.

Figure 8.13 shows the B(1s) XANES spectrum of a cBN sample produced by magnetron sputtering (MS) without high voltage bias pulses for stress relaxation. Under this conditions the intrinsic stress in the cBN layer is about -10 GPa. The spectra of reference samples from cBN and wBN powders and of HOPBN are also shown as signatures of sp^2 and sp^3 bonding environments. In the following discussion the focus is laid on the B(1s) edge since it contains more detailed information than the N(1s) spectrum, although similar trends are observed.

In the case of hBN, the XANES spectrum shows two absorption edges with thresholds around 191 and 197 eV corresponding to transitions from 1s levels to π^* and σ^* states, respectively. In addition, a sharp π^* peak at 192 eV is observed that originates from an excitonic state located a few tenth of eV below the continuum [162]. For the case of cBN, the spectrum shows a single edge corresponding to 1s $\rightarrow \sigma*$ transitions around 194 eV. In this case, no π^* resonance peaks are observed. Wurtzite-type BN shows like the cBN only one absorption edge around 195 eV with an absorption maximum between 195 and 196 eV. The onset of the σ^* edge is different for each allotrope and, therefore, the presence of the different edges and their position is a direct fingerprint of the bonding environment.

For the sample grown by magnetron sputtering, the σ^* edge is located around 194 eV. This and the presence of the π^* resonance peak at 192 eV indicate the presence of both sp^3 and sp^2 hybrids. The low intensity of the π^* resonance peak with respect to the σ^* edge and the shape of the σ^* edge revealing the presence of only one edge, however indicate the dominance of sp^3- bonds in the structure.

In order to estimate the sp^3/sp^2 ratio, usually a spectrum fit with a linear combination of the reference spectra of hBN and cBN is done. However, this method is not applicable for the MS sample due to the peculiar shape of the σ^* edge: Instead of a broad absorption maximum at 198 eV typical for polycrystalline cBN, which corresponds to 100% sp^3 hybrids without intrinsic stress, the edge shows a square-like shape with a plateau from 195 to 198 eV. This is interpreted as filling of states which originate from bonding environments differing from the non-stressed tetrahedrally coordinated bonding of cBN. Also the presence of wBN-like environments can not be assumed since a combination of the spectra from hBN, cBN, and wBN reference samples is not able to fit the spectrum of the MS sample satisfactory, since the filling of states between 194 and 195 eV can not be explained.
Therefore, the sample can not be considered as a plain mixture of these phases and the high intrinsic stress has to be accounted for. As the analysis of the cBN (111) lattice spacings in section 8.2.1 shows and as is described in the literature [112], the state of stress in such films is biaxial compressive, i.e. the cBN (111) lattice spacings are compressed in the plane of the film, whereas in out-of-plane direction d_{111} of cBN is extended ($d_{111}|| = 2.0896$ Å and $d_{111} \perp = 2.1179$ Å).

The spectrum of the MS sample is therefore interpreted as an sp^3 matrix with a distri-

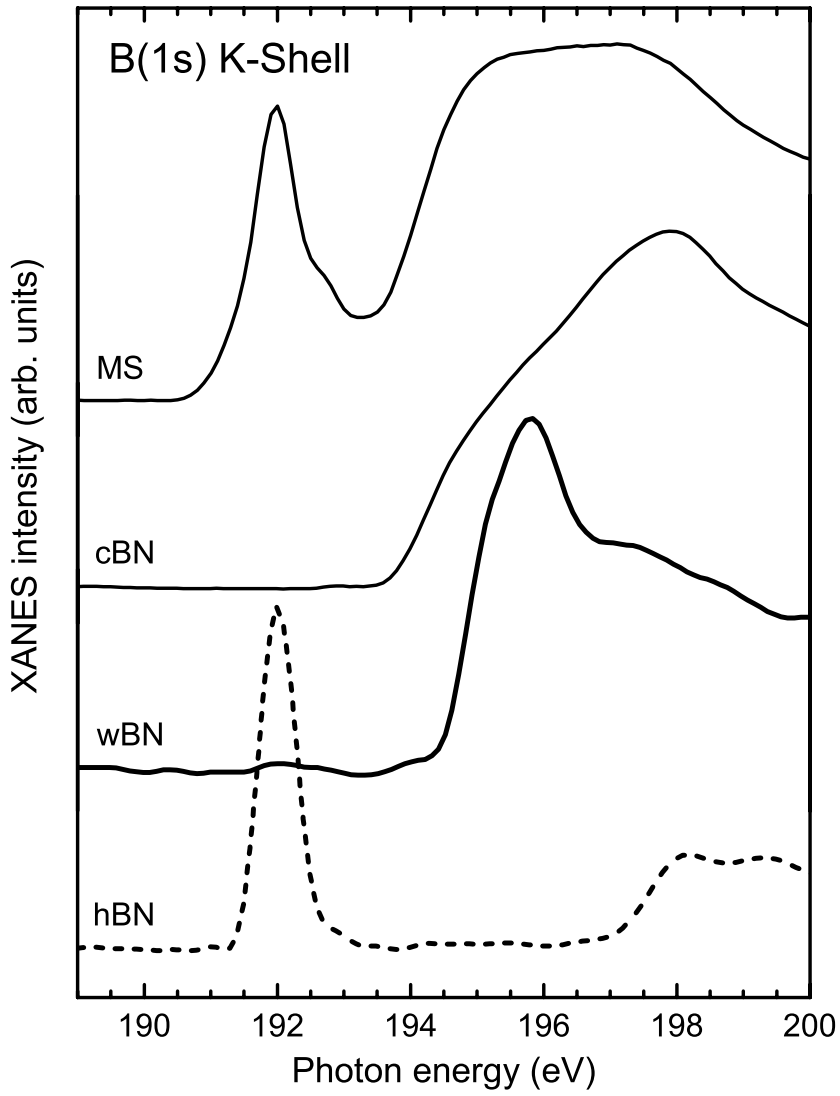

Figure 8.13: XANES B1s spectra of a magnetron sputtered cBN sample (MS) with high intrinsic stress (-10 GPa). The reference spectra of cBN, wBN and hBN are also shown for comparison. The wBN spectrum is taken from Terminello et al. [161].

bution of bond lengths induced by the high biaxial stress and with the intercalations of sp^2 sites. Since the position of the σ^* edge depends on the bond length [163], such a distribution of bond lengths would lead to the presence of several σ^* edges and the measured spectrum would be the composition of all of them. Therefore, the shape of the B(1s) XANES spectra for the sample grown with MS is considered to be the result of distortion and strain of the bond length of sp^3 hybrids and closely related to the high biaxial stress in the sample.

In the following, samples with different degree of stress are analyzed in order to affirm the correlation between the stress of the sample and its bonding characteristics. The XANES spectra originate from the near surface region of the sample, i.e. max. 10-20 nm below the surface. In this region the dynamic damage is less than the stationary bulk damage (see section 5). Hence, the stress in the near surface region should be higher than in the bulk. In figure 8.14, the dynamic damage profile for cBN growth under 8 keV Ar/N_2 ion bombardment with a duty cycle of 0.6 % is shown. The dashed area marks the analysis depth that is covered by XANES. It becomes clear that the stationary bulk damage can not be used to characterize the degree of stress relaxation in the near surface region. Therefore, an average damage value has been calculated for the near surface of the cBN film by an integration of the dynamic damage profile. For the samples analyzed by XANES the instantaneous stress, the stationary bulk damage, and an average damage value for the integration from 0-10 nm and from 0- 20 nm depth are summarized in table 8.3. Since the XANES spectrum itself represents an average over the bonding states in the surface region, the surface damage values should be regarded as margins only.

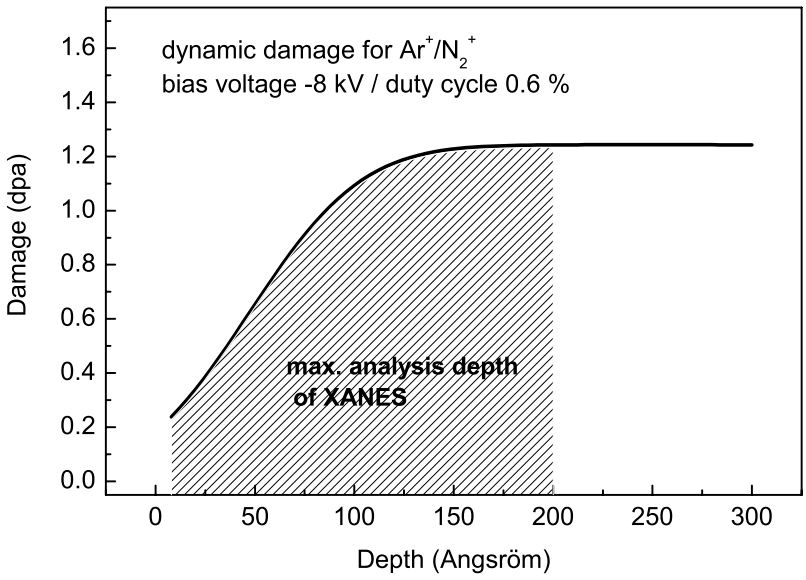

Figure 8.14: Dynamic damage distribution for 8keV Ar^+/N_2^+ implantation during cBN deposition. The dashed area demonstrates the maximum analysis depth of the XANES.

Figure 8.15 shows the B(1s) XANES spectra for cBN films with different level of intrinsic stress as described in table 8.3. The spectrum of the sample produced with 0 dpa refers to

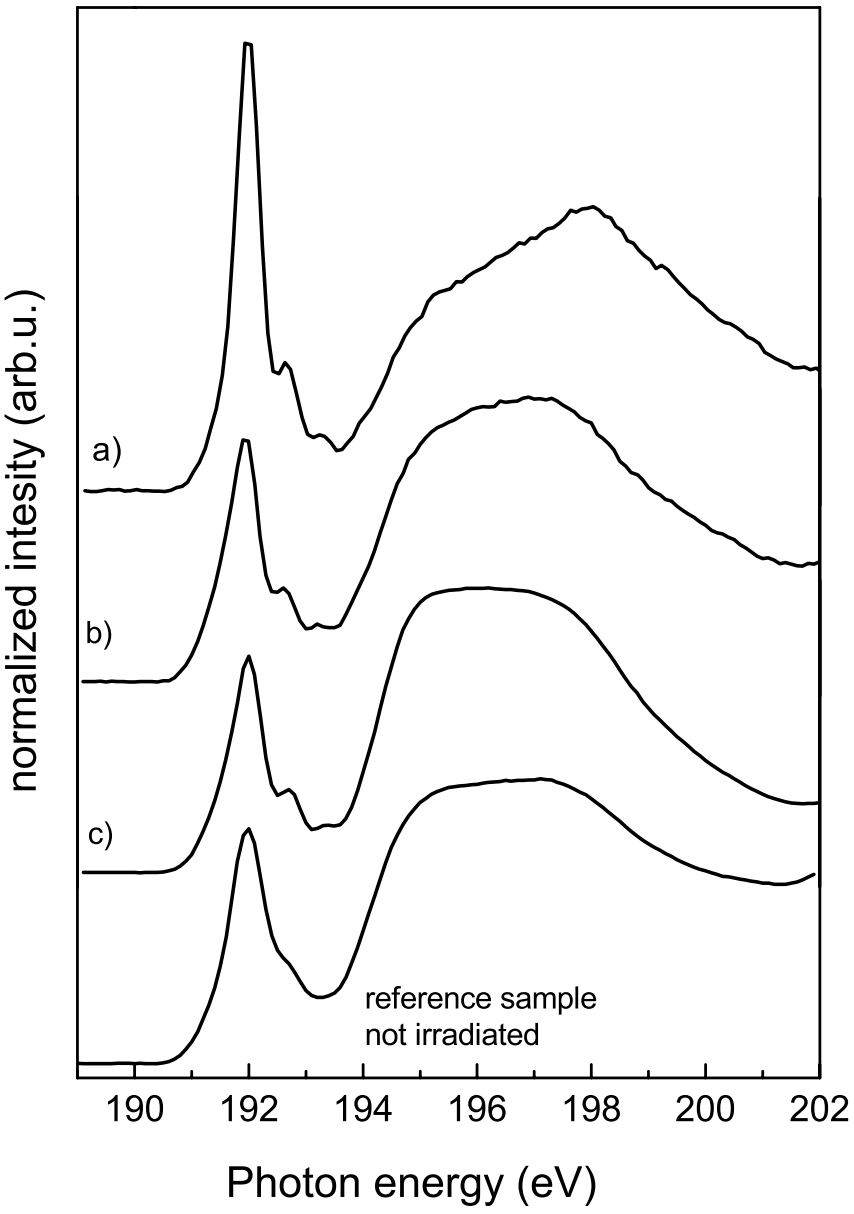

Figure 8.15: XANES B1s spectra of cBN films produced with different degrees of ion induced damage and different levels of intrinsic stress. Instantaneous stress and average surface damage values are summarized in table 8.3.

Table 8.3: Instantaneous stress in the cBN, stationary bulk damage, and surface damage values obtained from averaging the dynamic damage profile over 0 - 10 nm and 0 - 20 nm for the samples analyzed by XANES.

sample	instantaneous stress (GPa)	stationary bulk damage (dpa)	average surface damage 0-10 nm (dpa)	average surface damage 0-20 nm (dpa)
a	-1.6	1.2	0.63	0.91
b	-1.8	0.7	0.46	0.57
c	-2	0.6	0.31	0.45

the sample produced without simultaneous medium energy bombardment and corresponds to that shown in figure 8.13. The samples grown in the low damage range (< 1 dpa) show the same square-like shape of the absorption edge and low signal from the π^* resonance than the non irradiated reference sample (0 dpa). Only for the sample that was grown under 1.2 dpa, the shape of the σ^* edge approaches that of the polycrystalline stress-free cBN reference spectrum. In this sample, the intensity of the π^* resonance increases substantially, indicating the transformation of cBN to hBN or an increased domaine size and ordering of the sp^2 environments. The latter is unlikely since the analysis of the XRD domain size of hBN showed no increased degree of ordering due to ion bombardment. This result is, however, in agreement with results from infrared spectroscopy (see section 8.3.1) where an enhanced transition to hBN was observed for damage values > 0.8 dpa. For the samples grown in the low damage range, only very subtle changes in the spectra with respect to the MS reference sample are observed, where at the same time a large difference of stress is measured. This could be attributed to the fact that cantilever bending can measure the stress depth resolved but cannot resolve the stress from the very surface region, which is the origin of the XANES spectra. Also the ion induced damage in the near-surface region is below the stationary bulk damage and therefore the maximum possible stress relaxation is not achieved there. It is concluded that XANES can give, complementary to the cantilever bending method, XRD, and IR spectroscopy, information about the stress and bonding environment in the near surface region.

More detailed comparisons can be extracted from the derivative of the XANES intensity (fig. 8.15), as shown in Figure 8.16. The different maxima indicate the onset of the different absorption edges (ionization potential or IP energy). In these samples, the most prominent feature appears around 194-195 eV, which indicates, in comparison with the reference samples, that the bonding environment corresponds mostly to cBN. Only the sample that was grown at 1.2 dpa shows a weak second maximum at 197.4 eV in the derivative spectrum indicating some increase of the sp^2 content. This phenomenon could also be related with an enhancement of the typical sp^2 surface layer. Looking at the IP of the sp^3 hybrids, a broadening of the maximum is observed for the samples with high stress and low amount of ion induced damage. This is interpreted, in analogy to the broad absorption maximum of the 0 dpa sample, as a result of a distribution of bonding environments due to stress. The position of the maximum of the σ^* edge (i.e. the intersection with the solid line corre-

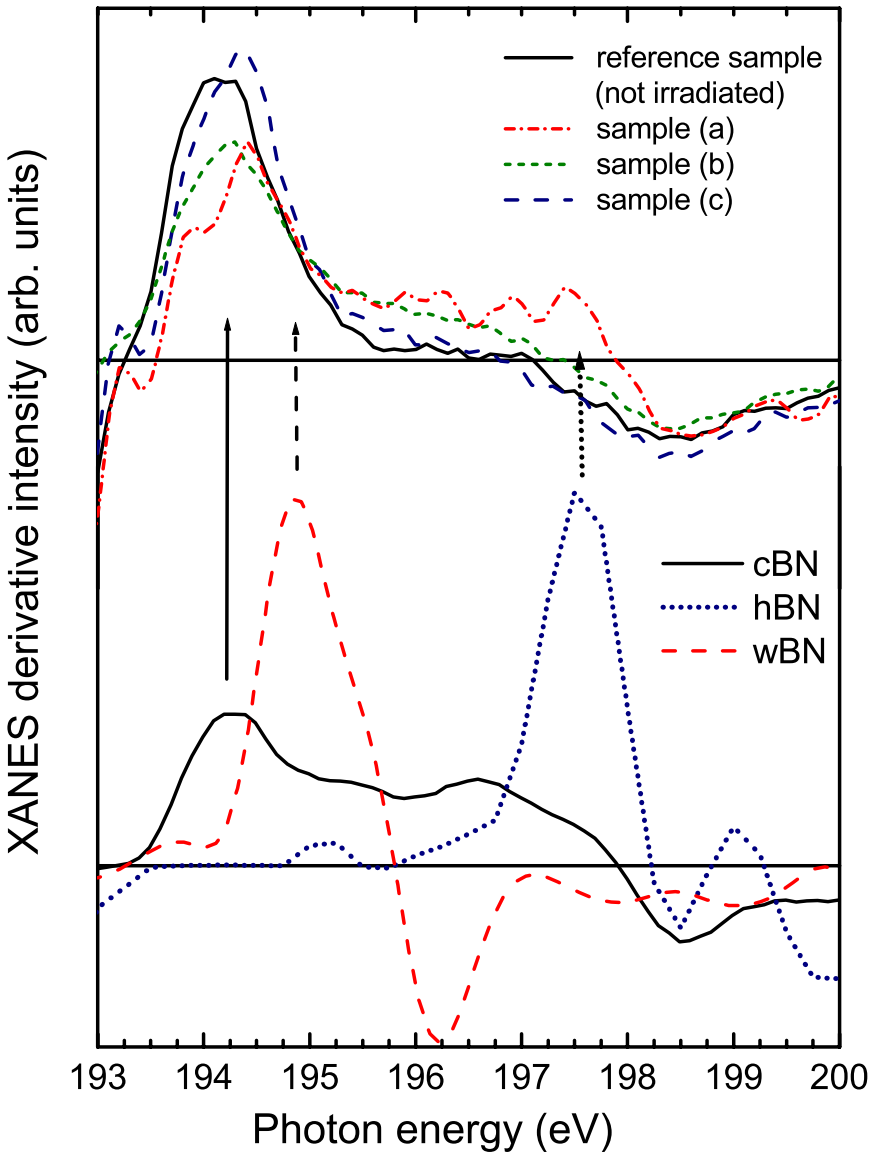

Figure 8.16: Derivative XANES signal of the spectra shown in figure 8.15. For comparison also the derivative spectra of the cBN, hBN, and wBN reference spectra shown in figure 8.13 are shown. Instantaneous stress and average surface damage values are summarized in table 8.3.

sponding to 0) with respect to the IP is correlated with the bond length [163]. By carefully analyzing the derivative spectra, a shift of the maximum of the σ^* edge to higher energies is observed, corresponding to an increase of the bond length by 0.02 Å between the high stress and the low stress sample. Such an increase of the bond length is in qualitative agreement with the observed increase of the in-plane lattice distance by XRD.

8.5 Summary of stress and microstructural investigations

In this section an attempt is made to summarize the results obtained from all stress and microstructural investigations and to draw some conclusions about the correlation between the state of stress, the ion induced damage, and the microstructure.

1. cBN as deposited without pulsed high voltage bias

   From TEM cross sectional images and XANES analysis it can be stated that once nucleated, the cBN grows almost phase pure. The domain size calculated from x-ray diffraction patterns is about 6 nm parallel and 3-4 nm perpendicular to the surface. Hexagonal BN is present in the buffer layer, but also some small amount is found by XANES in the surface region. In the XRD spectrum, the hBN signature originates most likely from the buffer layer and shows that the basal planes there are oriented perpendicular to the surface. This can be seen also in the TEM micrographs. Angular studies of the XANES π^*/σ^* intensity ratio reveal no preferred orientation of the hBN in the surface region. The hBN in the surface region most likely originates from a thin sp^2 bonded surface layer although it is not visible in the TEM images. The analysis of the B1s $\sigma*$ edge reveals a bonding structure that can not be explained by a composition of cBN + hBN. The stress in the as deposited cBN is -9 to -11 GPa and by XRD is confirmed to be biaxial. It is suggested therefore that the shape of the B1s $\sigma*$ edge is the result of a distribution of bond length due to the high biaxial compressive stress. The XRD analysis confirms the large difference of the lattice distances in in-plane and out-of-plane direction.

2. Low stress cBN

   The compressive stress in cBN can be released during growth by simultaneous ion bombardment in the energy range of 8 - 2.5 keV. The residual stress can be reduced to -1 to -2 GPa and results from an equilibrium between stress formation by low energy ions in the very near surface region and relaxation by the high energy ion in 5 to 15 nm depth. In the range of low damage that is induced by the high energy ions, the stress relaxation increases with increasing number of dpa. Above a critical value of about 0.8 dpa no further stress relaxation is achieved. It could be shown that by adjusting the energy and the flux of the high energy ions keeping the ion induced damage constant, also the resulting stress relaxation is constant. In this way cBN growth with an instantaneous stress of -1.6 GPa could be achieved with pulse voltages of only -2.5 kV.

In the low damage range IR spectroscopy showed that cBN is stable, in the high damage range, however, an increased transformation to hBN is observed. The cBN and hBN domain size are not changed due to the high energy ion bombardment. This means that cBN with long-range order across the grains is rather stable against ion bombardment, and the observed transformation to hBN occurs probably from short-range ordered material that contributes to the infrared signal but not to the XRD intensity. This short-range ordered material could be composed of a mixture of sp^3 and sp^2 bonded sites, similar as in ta-C, and become more and more sp^2-like with increasing ion-induced damage.

The shape of B1s $\sigma*$ edge of those samples deposited with an ion induced damage below 0.8 dpa, did not show any significant changes compared to the non relaxed sample. Considering that the number of displacements in the surface region is lower than in the bulk, the XANES results indicate that the biaxial stress remains very high in the surface region. Only when more damage is introduced (1.2 dpa in the bulk), the number of displacements is increased sufficiently to induce a change of the bonding structure and stress relaxation also in the surface region.

Finally the analysis of the low energy ions revealed that the cBN content in films grown under energetic ion bombardment can be increased significantly by reducing the energy of the assisting ions to 100 eV. From this result it is concluded that a high sputter yield hinders the cBN growth and advances the formation of hBN. Comparing the cBN content with the stress measured in this samples, it can be stated that the cBN content is not correlated with the amount of stress in the layer.

Possible mechanisms of stress relaxation

Cantilever bending enables a macroscopic analysis of the instantaneous stress, whereas x-ray diffraction gives insight to the microscopic strain of the material. By both methods an ion induced stress/strain relaxation is observed and the degree of relaxation increases with the number of atomic rearrangements. The stress measured by cantilever bending levels out at $\sim$ -1.5 GPa. On the other hand the XRD data converge towards a fully relaxed structure, however due to the low number of data points it cannot be concluded that a full stress relaxation by ion bombardment is possible.

Two different mechanisms of stress relaxation are discussed. On microscopic scale the stress is released by a relaxation of strain within the grains, i.e. due to atomic rearrangements defects like self-interstitials and 3- or 5-fold coordinated atoms are annealed. In the model of the thermal spike [55], which is implied also in the stress model of Davis [110] the ratio of newly formed defects and annealed defects is very low for high ion energies. This suggest that a full relaxation can be achieved.

On macroscopic scale another mechanism must be involved to explain the out-leveling of the curve in figure 8.5. A possibility would be a partial transformation from cBN to hBN. This was observed by FTIR with increasing ion induced damage (see above). Since the XRD domain size is not decreased by the ion bombardment, the increased hBN content is most likely located at the grain boundaries. During the deposition of cBN (see section 8.1), σ increases when the nuclei coalesce and not directly upon nucleation , i.e. when the cBN crystallites are not anymore isolated by an hBN surrounding but are neighboring each other.

The same mechanism may apply during ion induced stress relaxation and could explain the experimental findings in figure 8.5: if compliant sp^2 bonded material is created due to the ion bombardment between the cBN grains, the stress could be reduced by an expansion of the cBN grains. If each cBN grain is surrounded completely by a compliant and low ordered phase of mixed sp^2/sp^3 sites, the residual stress would then originate from this matrix. And as it is known from ta-C, such structures can have large compressive stress. This would explain, why on macroscopical level, the stress can not be relaxed below $\sim$ -1.5 GPa.

Probably, the observed stress relaxation behavior could be a result of competition between both mechanisms. During the collision cascade and the subsequent thermal spike the compressive stress due to interstitial-type defects and overcoordinated atoms could be released within the grains. But, on the other hand, the collision cascades affect also low ordered material in between the cBN crystallites. And here atomic rearrangements could induce a transformation of short-range ordered predominantly sp^3 bonded material to short-range ordered sp^2 bonded material, which maintains a residual compressive stress due to the low degree of ordering.

8.6 Adhesion

In this section the issue of film adhesion is discussed. It has to be admitted that although the film stress can be released to values, which are typical for example in commercial TiN films, the adhesion to silicon substrates is still very poor. For magnetron deposition of cBN without any stress relaxation, the films often delaminate already during deposition when a critical film thickness of 80 to 100 nm is exceeded. When the films are grown with simultaneous stress relaxation this did not occur, even for the deposition of 700 nm cBN (with a 150 nm buffer layer of hBN). But under atmospheric conditions, the films delaminate within short time. Figure 8.17 shows an optical micrograph of a cBN film that was grown under simultaneous stress relaxation. The film delaminated after the sample was removed from the vacuum chamber. It reveals that the film has detached from the substrate, but is not disrupted. This points to a good cohesion within the layer with the failure taking place at the interface. The detached film has wrinkled, probably due to a gradient of residual stress over the film thickness. Due to the fact that the relaxation of the stress takes place only after the cBN has nucleated (plus the growth of additional 20 nm high stress cBN), the underlying hBN can still possess very high stress. This layered structure leads obviously to stress gradients in the film and causes the curling when the film has detached from the substrate.

Apart from stress gradients in the layer, the ambient conditions have strong influence on the film stability. For low stress cBN films, even for d_f = 800 nm, delamination does not occur during deposition, nor as long as the samples are kept in vacuum. Also storage at atmospheric pressure in nitrogen atmosphere does not lead to delamination. Only when the films are exposed to air, they delaminate within hours. Therefore it is believed that moisture is determining the adhesion. On the other hand, cBN films with high stress produced by laser ablation of a BN target [63] and by magnetron sputtering from a B_4C target employing a BCN gradient layer [96], were reported to be stable under ambient conditions for years. Also the magnetron sputtered films produced during this work are absolutely stable after

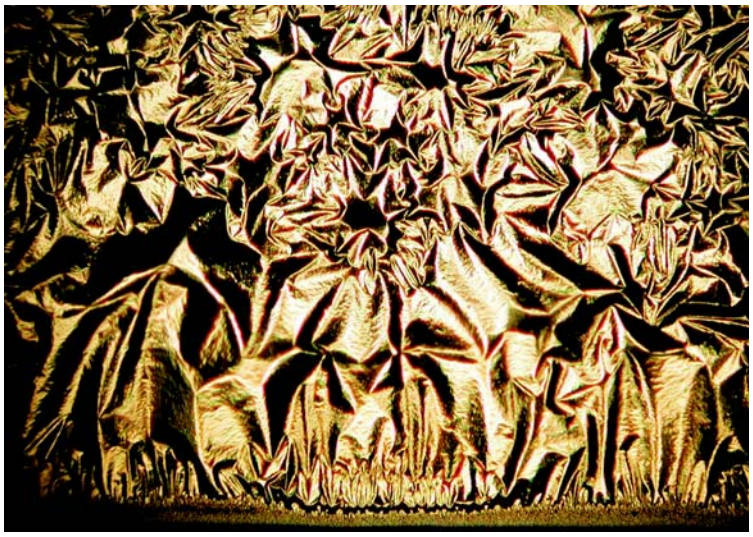

Figure 8.17: Optical micrograph (100x magnification) of a beautifully delaminated cBN film. The film was deposited using the high voltage substrate bias pulses and the measured FPUW is shown in fig. 8.3.

annealing at 900° C. This leads to the conclusion that a delamination due to moisture depends on the microstructure of the layer. It is likely that H_2O and OH migrate along grain boundaries and through porosity to the film/substrate interface. Since it was found in this work (see section 7.2.2), that boron-rich films contain up to 8 at% hydrogen, whereas in stoichiometric films the H content is below 2 at %, it is suggested that preferably excess boron is involved in chemical reactions producing boron oxides or boron hydroxides (boric acid). Consequently, a volume increase leads to delamination. In laser ablation, boron and nitrogen arrive as energetic ablated particles at the substrate (particle energies are around 100 eV). This might lead to a dense structure with little migration paths and to an overall stoichiometry, specially at the film/substrate interface, and hence minimize the presence of excess boron. The same effect may be attained by the presence of carbon, leading to the formation of boron carbide bonds rather than B-B bonds, oxidation of boron, or the reaction with hydroxides.

In this work, in order to improve the film adhesion, a thick graded hBN buffer layer was grown prior to cBN nucleation. One aim hereby was to improve the adhesion by an interface mixing. A second aim was to minimize the stress gradients with a graded buffer layer. To achieve interface mixing, in the beginning of the deposition the high voltage bias was set for 3 minutes to 5 μs pulses of -2 kV without any low voltage bias. Then, the low voltage substrate bias is increased step wise from 0 to -180 V until approximately 120 nm hBN are deposited. At -180 V, cBN nucleation takes place. The resulting evolution of the FPUW is shown in figure 8.18.

During the interface mixing and the time with no bias voltage the instantaneous stress in the sample is close to zero. When the bias voltage is increased, σ is very high, up to -5 GPa, for a bias voltage of -50 V, but remains then at a low value of about -1 GPa for substrate voltages from -75 to -180 V. Only with the beginning of cBN nucleation at -180 V,

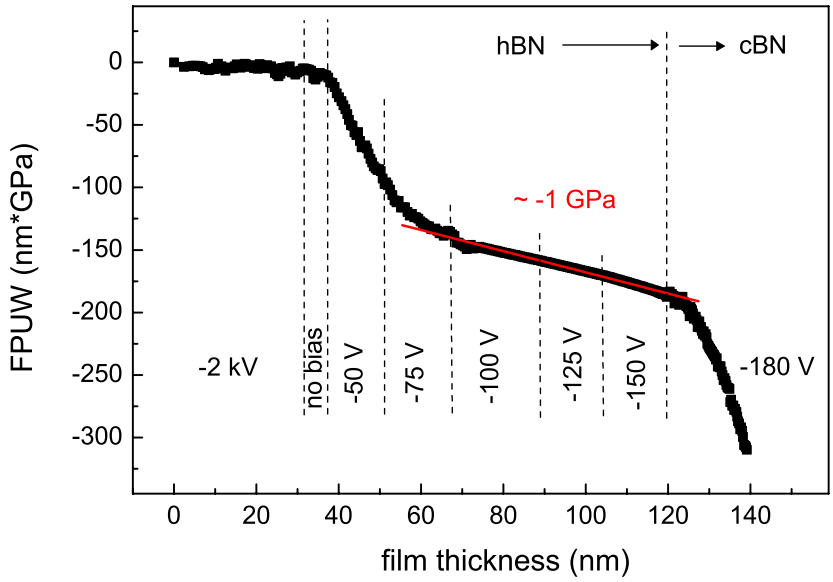

Figure 8.18: FPUW evolution with the film thickness during the deposition of a graded hBN buffer layer during initial interface mixing and gradually increasing low voltage substrate bias from 0 to -180 V.

σ increases to $\sim$ -9 GPa, which is typical for cBN growth.

Comparing the FPUW data with the corresponding evolution of the microstructure shown in the TEM image in figure 8.19, one can see that close to the substrate (left side) the structure a $\sim$ 5 nm thick amorphous layer is formed due to the interface mixing. Then follows a part where the hBN basal planes do not show any preferential orientation but some are bended. This corresponds to the film that was deposited with the substrate bias set to -50 V and σ is -5GPa. Further on, in the right part of the image, the basal planes are oriented parallel to the substrate. This well aligned structure does not change until the point of cBN nucleation (not shown). From this it is concluded that with increasing bias voltage (from 0 to $\sim$ -75 V) the orientation of the hBN basal planes changes from more or less parallel to the surface to perpendicular to the surface. This change of the texture is accompanied by a large instantaneous stress. But once the orientation of the basal planes has changed to perpendicular to the surface, the instantaneous stress does not increase even though the ion energy is increased. In the case when the substrate bias is -150 V during the total deposition time (see section 8.1), σ is constant around -4 GPa in the hBN layer.

Using this type of buffer layer, the adhesion could be improved, but not sufficiently. Under ambient, humid conditions the layers still delaminate after some days.

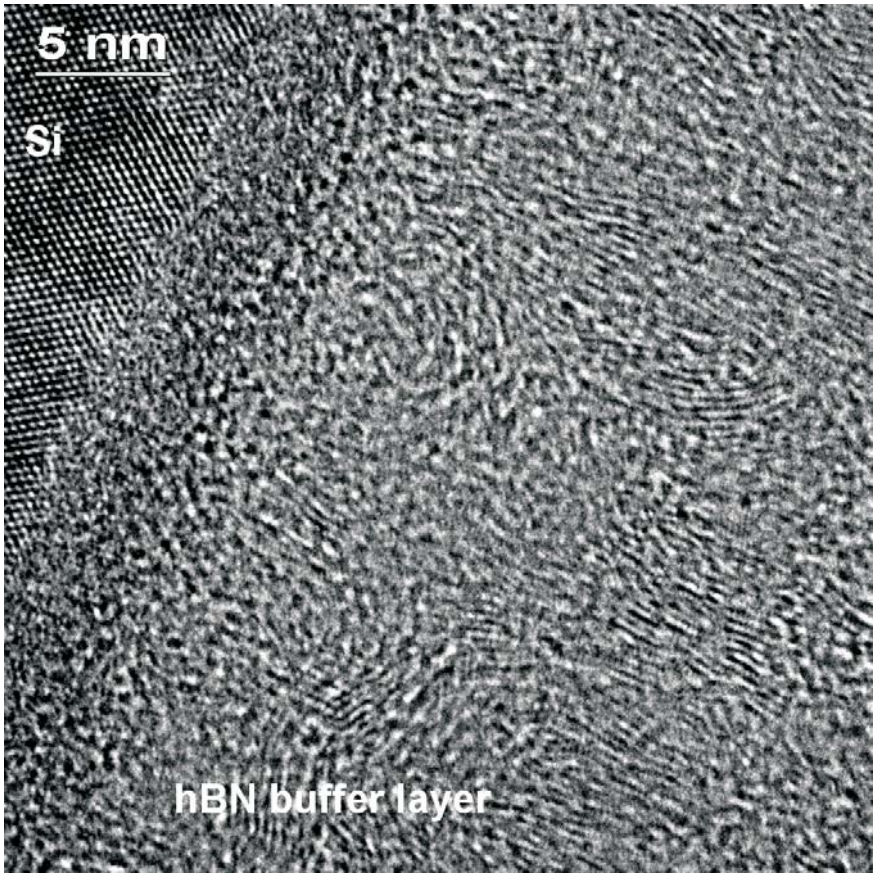

Figure 8.19: TEM cross sectional image of a hBN buffer layer deposited with initial interface mixing and gradually increasing low voltage substrate bias from 0 to -180 V.

9 Conclusions and Outlook

The aim of the presented work was to deposit cubic boron nitride thin films by magnetron sputtering under simultaneous stress relaxation by ion implantation.

In order to get a closer understanding of the film growth, first a plasma analysis was performed. The results yield the basic physical parameters of the film growth like the ion to neutral arrival ratio and the ion energy distribution.

An in situ instrument for stress measurement based on laser deflectometry and in situ ellipsometry, developed for IBAD experiments, was adjusted for magnetron sputter deposition. An important insight was that for the detection of the reflected laser beam with a position sensitive diode, one has to take into account the signal that is induced by light emission from the plasma.
The characteristic evolution of the instantaneous stress during the layered growth of cBN films observed in IBAD experiments, could be reproduced for magnetron sputter deposition.

To achieve simultaneous stress relaxation, a complex bipolar pulsed substrate bias source was constructed. This power supply enables the growth of cBN thin films under low energy ion irradiation and, for the first time, the simultaneous implantation of ions with an energy of up to 8 keV during high voltage pulses. It was demonstrated that the instantaneous stress in cBN thin films can be released down to -1.1 GPa by simultaneous ion bombardment during the high voltage pulses. A simultaneous stress relaxation during growth is possible in the total investigated ion energy range between 2.5 and 8 keV. These are the lowest ion energies reported for the stress relaxation in cBN. Since such a substrate bias power supply is easy to integrate in existing process lines, this result is important for industrial deposition of thin films, not only for cubic boron nitride films. Also bias voltages in the order of some kV are feasible in commercial production.

Using in situ cantilever bending it was found that the amount of stress relaxation depends on the damage that is induced by the high energy ion bombardment and is therefore dependent on the ion energy and the high energy ion flux. In practise this means that the stress relaxation is controlled by the product of the pulse voltage and the pulse duty cycle or frequency. This means that the same stress relaxation can be achieved with different ion energies if the same number of dpa is introduced by the energetic ion implantation, i.e. if the duty cycle is adjusted accordingly.
In the low damage range, below 0.8 dpa, the relaxation increases with the number of displacements. In the high damage range, dpa > 0.8, however no further stress relaxation can be achieved.

The cantilever bending measurements were complemented on microscopic scale by x-ray

diffraction. The analysis of the cBN (111) Bragg diffraction peak revealed a pronounced biaxial compressive state of stress in a non-relaxed cBN film. Post deposition annealing at 900°C of a sample with an ion induced damage of 1.2 dpa, resulted in a complete relaxation of the lattice with equal in-plane and out-of-plane lattice parameters. The obtained d(111) value are considered as a reference for stress-free cBN films produced by magnetron sputtering. In the case of medium-energy ion bombardment, the in-plane and out-of-plane lattice parameters approach the value of the annealed sample with increasing the ion induced damage as a signature of the stress relaxation.

The stability of cBN under ion bombardment was investigated by IR spectroscopy. It was found that for a dynamic damage above 0.8 dpa the cBN is partially transformed to hBN. The transformation rate increases with increasing damage. That means that below 0.8 dpa the stress is released in the cBN, whereas for higher damage instead of further stress relaxation only a transformation to hBN takes place.

On the other hand, the full width at half maximum of the XRD diffraction peaks remains constant independent of the ion bombardment, point to a pronounced stability of crystalline cBN. It is therefore proposed that in between the grains a short-range ordered, sp^3/sp^2-mixed phase exists, which could be similar to taC and could become more and more sp^2-like with increasing damage.

Comparing the results from substrate curvature measurement, XRD, and IR spectroscopy possible mechanisms of stress relaxation were discussed. The observed stress relaxation could be the result of two different processes. On the one hand, during the collision cascade and the subsequent thermal spike the compressive stress due to interstitial-type defects and overcoordinated atoms could be released within the grains. On the other hand, the collision cascades affect also low ordered material in between the cBN crystallites. And here atomic rearrangements could induce a transformation of short-range ordered sp^3/sp^2 bonded material to short-range ordered sp^2 bonded material, which maintains a residual compressive stress due to the low degree of ordering.

High energy argon ions seem to enhance the phase transformation to hBN. However, they are not required for the nucleation and growth of the cBN in this system. Also the stress can be released to about -2 GPa by using only nitrogen ions (i.e. using a pure N_2 discharge).

From the analysis of the near surface region by XANES, it can be concluded the stress relaxation by the energetic ion bombardment is less at the surface than in the bulk film. This is explained with the dynamic profile of the ion induced damage, that reaches the stationary bulk value in 15-20 nm depth, whereas it is decreasing towards the surface. This fits with the results that the stress relaxation is dependent on the amount of ion induced damage.

The influence of the growth assisting (the low energy) ions on the film stress and phase bonding structure have been investigated. In the range between 100 and 200 eV (bias voltage plus plasma potential) the cBN content and the growth rate increase with decreasing ion energy. The instantaneous stress has a maximum at $\sim$ -120 V and decreases for lower and higher bias voltages, in qualitative agreement with the Davis model. This leads to 2 conclusions: first, the stress in the film is not a function of the cBN content; and second an

enhanced sputtering at the film surface promotes hBN growth on the expense of cBN.

Although the stress in the films was released to values, which are typical for other hard coatings (e.g. TiN), the film adhesion was still not sufficient for any application. There are two possible reasons for this. On on side stress gradients can build up in the film, since the hBN and the hBN/cBN interface are not treated with the energetic ion bombardment. But probably more important is the sensitivity to moisture. Since our samples are stable after annealing at 900° C and also other groups report the production of stable films even though they have very high stress, it is concluded that the microstructure and stoichiometry can promote a chemical reaction with ambient H and O species.
The deposition of an hBN buffer layer before the cBN nucleation can help to improve the adhesion. The deposition of multi layered hBN/cBN structures could help to reduce the stress gradients over the total film thickness. Further it is suggested to use instead of an hBN buffer layer a carbon containing buffer layer, since those are reported to be inert against moisture.

More generally, it can be concluded that cBN thin film deposition is, although not yet fully understood, technical no longer problematic. The physical parameter window, in which the cBN growth is possible is known and can be translated to various deposition processes. The problem of excessive intrinsic stress has been addressed by a large number of scientists and possible solutions have been suggested to either decrease the stress formation, to relax the stress, or to provide a suitable interface that withstands the forces of a stressed film. Using energetic ion implantation has been shown to relax the residual stress to a level very well acceptable for hard coating applications. In this work it has been demonstrated that this ion implantation can be realized in common commercial processes for the application on hard coatings on tools at acceptable expenses. Already good experiences exist concerning various adhesion layer systems and the elimination of the hygroscopy. Therefore, to lead cBN films finally into application, now only an interface engineering is required, which combines the different aspects of the cBN research.

Bibliography

[1] H. Hollek, J. Vac. Sci. Technol. A 4 (1986) 2661.

[2] R. Andrievski, Int. J. Refr. Metals Hard Mater. 19 (2001) 447.

[3] L. Vel, G. Demazeau, J. Etourneau, Mater. Sci. Engin. B 10 (1991) 149.

[4] C. Ronning, E. Dreher, H. Feldermann, M. Gross, M. Sebastian, H. Hofsäss, Diam. Relat. Mater. 6 (1997) 1129.

[5] O. Mishima, K. Era, J. Tanaka, S. Yamaoka, J. Appl. Phys. 53 (1988) 963.

[6] G. Demazeau, Diam. Relat. Mater. 4 (1995) 284.

[7] R. Wentdorf, Chem. Eng. 68 (1961) 177.

[8] C. Fitz, Entwicklung und Relaxation mechanischer Spannnungen in Bornitrid Schichten, Ph.D. thesis, Technische Universität Dresden (2001).

[9] W. Fukarek, J. Vac. Sci. Technol. A 19 (2001) 2017.

[10] X. Zhang, H.-G. Boyen, N. Deyneka, P. Ziemann, F. Banhart, M. Schreck, Nature Materials 2 (2003) 312.

[11] J. Ullmann, J. Baglin, A. Kellock, J. Appl. Phys 83 (1998) 2980.

[12] H.-G. Boyen, P. Widmayer, D. Schertberger, N. Deyneka, P. Ziemann, Appl. Phys. Lett. 76 (2000) 709.

[13] C. Fitz, A. Koltisch, W. Möller, W. Fukarek, Appl. Phys. Lett. 80 (2002) 55.

[14] C. Fitz, W. Fukarek, W. Möller, Thin Solid Films 408 (2002) 155.

[15] J. Hahn, M. Friedrich, R. Pintaske, M. Schaller, N. Kahl, D. Zahn, F. Richter, Diam. Relat. Mater. 5 (1996) 1103.

[16] R. Pintaske, T. Welzel, N. Kahl, M. Schaller, J. Hahn, F. Richter, Surf. Coat. Technol. 90 (1997) 275.

[17] S. Ulrich, J. Schwan, W. Donner, H. Erhardt, Diam. Relat. Mater. 5 (1996) 548.

[18] S. Kouptsidis, H. Lüthje, K. Bewilogua, A. Schütze, P. Zhang, Diam. Relat. Mater 7 (1998) 26.

[19] A. Lousa, S. Gimeno, Diam. Relat. Mater. 10 (2001) 1347.

[20] J. Ye, U. Rothhaar, H. Oechsner, Surf. Coat. Technol. 105 (1998) 159.

[21] K. Sell, H. Hollek, H. Leiste, M. Stüber, J. Ye, Diam. Relat. Mater. 11 (2002) 1272.

[22] W. Otano-Rivera, L. Pilione, J. Zapien, R. Messier, J. Vac. Sci. Technol.A 16 (1998) 1331.

[23] K. Yamamoto, M. Keunecke, K. Bewilogua, Thin Solid Films 377-378 (2001) 331.

[24] C. Lee, T. Yang, C. Hsu, C. Cheng, M. Wong, Thin Solid Films 420-421 (2002) 130.

[25] T. Pfeifer, F. Richter, T. Welzel, H. Kupfer, P. Willich, J. Appl. Phys. 93 (2003) 2009.

[26] M. Johansson, I. Ivanov, L. Hultman, E. Münger, A. Schütze, J. Vac. Sci. Technol. A 14 (1996) 3100.

[27] J. Hahn, F. Richter, R. Pintaske, M. Röder, E. Schneider, T. Welzel, Surf. Coat. Technol. 92 (1997) 129.

[28] A. Kurdyumov, V. Solozhenko, W. Zelyavski, J. Appl. Cryst. 28 (1995) 549.

[29] K. McCarty, P. Mirkarimi, D. Medlin, T. Friedmann, J. Barbour, Diam. Relat. Mater 5 (1996) 1519.

[30] P. Mirkarimi, K. McCarty, D. Medlin, Mater. Sci. Engin. R21 (1997) 47.

[31] R. Pease, Acta. Cryst. 5 (1952) 356.

[32] T. Ishii, T. Sato, Y. Sekikawa, M. Iwata, J. Cryst. Growth 52 (1981) 185.

[33] F. Galasso, Structure and properties of inorganic solids, Pergamon Press, Oxford, 1970.

[34] F. Corrigan, F. Bundy, J. Chem. Phys. 63 (1975) 3812.

[35] V. Solozhenko, Thermochim. Acta 218 (1993) 221.

[36] K. Albe, Phys. Rev. B 55 (1997) 6203.

[37] H. Sachdev, R. Haubner, H. Nöth, B. Lux, Diam. Relat. Mater. 6 (1997) 286.

[38] D. Kester, R. Messier, J. Appl. Phys. 72 (1992) 504.

[39] P. Mirkarimi, K. McCarty, D. Medlin, T. Wolfer, T. Friedmann, E. Klaus, G. Cardinale, D. Howitt, J. Mater. Res. 9 (1994) 2925.

[40] W. Kulisch, S. Ulrich, Thin Solid Films 423 (2003) 183.

[41] H. Hofsäss, H. Feldermann, M. Sebastian, C. Ronning, Phys. Rev. B 55 (1997) 13230.

[42] S. Eyhusen, I. Gerhards, H. Hofsäss, C. Ronning, M. Blomenhofer, J. Zweck, M. Seibt, Diam. Relat. Mater. 12 (2003) 1877–1882.

[43] P. Mirkarimi, D. Medlin, McCarty, J. Barbour, Appl. Phys. Lett. 66 (1995) 2813.

[44] H. Feldermann, R. Merk, H. Hofsäss, C. Ronning, T. Zheleva, Appl. Phys. Lett. 74 (1999) 1552.

[45] Y. Panayiotatos, S. Logothetidis, M. Handrea, W. Kautek, Diam. Relat. Mater. 12 (2003) 1151.

[46] W. Dworschak, K. Jung, H. Erhard, Diam. Relat. Mater. 3 (1994) 337.

[47] A. Bergmaier, D. Dollinger, T. Faestermann, C. Frey, W. Dworschak, H. Erhardt, Diam. Relat. Mater. 4 (1995) 478.

[48] C. Ronning, A. Banks, B. McCarson, R. Schlesser, Z. Sitar, R. Davis, B. Ward, R. Nemanich, J. Appl. Phys. 84 (1998) 5046.

[49] R. Freudenstein, S. Reinke, W. Kulisch, Surf. Coat. Technol. 97 (1997) 270.

[50] D. McKenzie, D. Müller, B. Pailthorpe, Phys. Rev. Lett. 67 (1991) 773.

[51] S. Reinke, M. Kuhr, W. Kulisch, Diam. Relat. Mater. 3 (1994) 341.

[52] C. Fitz, W. Fukarek, A. Kolitsch, W. Möller, Surf. Coat. Technol. 128-129 (2000) 292.

[53] J. Robertson, Diam. Relat. Mater. 5 (1996) 519.

[54] H. Hofsäss, H. Feldermann, R. Merk, M. Sebastian, C. Ronning, Appl. Phys. A 66 (1998) 153.

[55] F. Seitz, J. Koehler, Solid State Phys. 3 (1956) 305.

[56] R. Heil, C. Aita, J. Vac. Sci. Technol. 15 (1997) 93.

[57] G. Cardinale, P. Mirkarimi, K. McCarty, E. Klaus, D. Medlin, W. Clift, D. Howitt, Thin Solid Films 253 (1994) 130.

[58] K. Inagawa, K. Wantanabe, H. Ohsone, K. Saitoh, A. Itoh, J. Vac. Sci. Technol.A 5 (1987) 2696.

[59] I. Caretti, I. Jimenez, R. Gago, D. Caceres, B. Abendroth, J. Albella, Diam. Relat. Mater. accepted.

[60] R. Gago, M. Vinnichenko, B. Abendroth, A. Kolitsch, W. Möller, J. Vac. Sci. Technol.A 21 (2003) 1739.

[61] D. Kester, K. Ailey, D. Lichtenwalner, R. Davis, J. Vac. Sci. Technol.A 12 (1994) 3074.

[62] M. Plass, W. Fukarek, A. Kolitsch, N. Schell, W. Möller, Thin Solid Films 305 (1997) 172.

[63] S. Weissmantel, G. Reisse, Appl. Surf. Sci 197-198 (2002) 331.

[64] A. Jankowski, Thin Solid Films 343-344 (1999) 238.

[65] A. Jankowski, J. Hayes, D. Makowiecki, M. McKernan, Thin Solid Films 308-309 (1997) 94.

[66] B. Abendroth, R. Gago, A. Kolitsch, W. Möller, Thin Solid Films in press.

[67] A. Schütze, K. Bewilogua, H. Lüthje, S. Kouptidis, S. Jäger, Surf. Coat. Technol. 74/75 (1995) 717.

[68] V. Linss, I. Hermann, N. Schwarzer, U. Kreissig, F. Richter, Surf. Coat. Technol. 163 (2003) 220.

[69] H. Yang, C. Iwamoto, T. Yoshida, Thin Solid Films 407 (2003) 67.

[70] M. Ye, M. Delplancke-Ogletree, Diam. Relat. Mater 9 (2000) 1336.

[71] W. Kulisch, R. Freudenstein, A. Klett, M. Plass, Thin Solid Films 377-378 (2000) 170.

[72] A. Soltani, P. Thevenin, A. Bath, Diam. Relat. Mater. 10 (2001) 1369.

[73] W. Zhang, S. Matsumoto, Jpn. J.Appl. Phys. 139 (2000) L443.

[74] W. Zhang, K. K. Matsumoto, S, Y. Bando, Diam. Relat. Mater. 10 (2001) 1881.

[75] C. Chan, W. Zhang, X. Meng, K. Chan, I. Bello, Y. Lifshitz, S. Lee, Diam. Relat. Mater. 12 (2003) 1162.

[76] W. Zhang, S. Matsumoto, J. Mater. Res 15 (2000) 2677.

[77] W. Zhang, S. Matsumoto, Phys. Rev. B 63 (2001) 73201.

[78] H. Yang, C. Iwamoto, T. Yoshida, J. Appl. Phys. 94 (2003) 1248.

[79] H. Hofsäss, C. Ronning, U. Griesmeier, M. Gross, S. Reinke, M. Kuhr, J. Appl. Phys. 67 (1995) 46.

[80] E. Franke, M. Schubert, H. Neumann, T. Tiwald, D. Thompson, J. Woollam, J. Hahn, F. Richter, J. Appl. Phys. 82 (1997) 2906.

[81] D. McKenzie, M. Bilek, J. Vac. Sci. Technol. A 16 (1998) 2733.

[82] G. Cardinale, D. Medlin, P. Mirkarimi, K. McCarty, D. Howitt, J. Vac. Sci. Technol. A 15 (1996) 196.

[83] K. McCarty, Diam. Relat. Mater 5 (1997) 1219.

[84] S. Fahy, C. Taylor, R. Clarke, Phys. Rev. B 56 (1997) 12573.

[85] P. Mirkarimi, D. Medlin, K. McCarty, D. Dibble, W. Clift, J. Knapp, J. Barbour, J. Appl. Phys. 82 (1997) 1617.

[86] D. Medlin, T. Friedmann, P. Mirkarimi, G. Cardinale, K. McCarty, J. Appl. Phys. 79 (1996) 3567.

[87] S. Weissmantel, G. Reisse, Thin Solid Films 355 (1999) 256.

[88] A. Ballal, L. Salamanca-Riba, C. Taylor II, G. Doll, Thin Solid Films 224 (1993) 46.

[89] K. Park, D. Lee, K. Kim, D. Moon, Appl. Phys. Lett. 70 (1997) 315.

[90] D. McKenzie, W. McFall, H. Simth, B. Higgins, R. Boswell, A. Durandet, B. James, I. Falconer, Nucl. Inst. Meth.B 106 (1995) 90.

[91] D. Litvinov, R. Clarke, Appl. Phys. Lett. 71 (1997) 1969.

[92] A. Schütze, K. Bewilogua, H. Lüthje, S. Kouptidis, Diam. Relat. Mater. 5 (1996) 1130.

[93] S. Weissmantel, G. Reisse, B. Keiper, A. Weber, U. Falke, M. Röder, Appl. Surf. Sci 127-129 (1998) 444.

[94] C. Fitz, A. Koltisch, W. Fukarek, Thin Solid Films 389 (2001) 173.

[95] C. Ronning, H. Feldermann, H. Hofsäss, Diam. Relat. Mater. 9 (2000) 1767.

[96] K. M., K. Weigel, K. Bewilogua, cBN auf Werkzeugen, Beschichtungsentwicklung und Charakterisierung; unpublished, 10. cBN-Expertentreffen, Hochschule Mittweida (September 29th to October 1st 2003).

[97] G. Reisse, S. Weissmantel, D. Rost, Diam. Relat. Mater. 11 (2002) 1276.

[98] R. Freudenstein, W. Kulisch, Thin Solid Films 420-421 (2002) 132.

[99] M. Kumagai, M. Suzuki, Y. Tanaka, Y. Setsuhara, S. Miyake, K. Ogata, M. Kohata, K. Higeta, T. Einishi, Y. Suzuki, Y. Shimoitani, Y. Motonami, Nucl. Inst. and Meth. B 127-128 (1997) 977.

[100] Y. Setshuhara, M. Kumagai, M. Suzuki, T. Suzuki, S. Miyake, Surf. Coat. Technol. 116-119 (1999) 100.

[101] H. Feldermann, C. Ronning, H. Hofsäss, Y. Huang, M. Seibt, J. Appl. Phys. 90 (2001) 12573.

[102] X. Wang, D. Mao, W. Li, X. Liu, A. Kolitsch, A. Muecklich, D. Manova, W. Fukarek, W. Möller, Surf. Coat. Technol. 131 (2000) 514.

[103] H. Göldner, F. Holzweissig, Leitfaden der Technischen Mechanik, VEB Fachbuchverlag, Leipzig, 1980.

[104] S. Tamulevicius, Vacuum 51 (1998) 127.

[105] W. Brantley, J. Appl. Phys. 44 (1973) 534.

[106] G. Stoney, Royal Soc. Proc. 82 (A553) (1909) 172.

[107] J. Thornton, D. Hoffman, J. Vac. Sci. Technol. 3 (1985) 576.

[108] J. Thornton, J. Tabock, D. Hoffman, Thin Solid Films 64 (1979) 1141.

[109] M. Bilek, D. McKenzie, R. Tarrant, S. Lim, D. McCulloch, Surf. Coat. Technol. 156 (2002) 136–142.

[110] C. Davis, Thin Solid Films 226 (1993) 30.

[111] J. Robertson, Mater. Sci. Engin. R 37 (2002) 129 – 281.

[112] J. Boettiger, P. Chevallier, P. Kringhoej, K. Schweitz, Adhesion Aspects of Thin Films 1 (2001) 1.

[113] N. Marks, D. McKenzie, B. Pailthorpe, Phys. Rev. B 53 (1995) 4117.

[114] P. Kazansky, L. Hultman, I. Ivanov, J.-E. Sundgren, J. Vac. Sci. Technol. 11 (1993) 1426.

[115] K. Sell, S. Ulrich, E. Nold, J. Ye, H. Leiste, M. Stüber, H. Holleck, Surf. Coat. Tecnol. 174 (2003) 1121.

[116] H. Xiao-Ming, T. Taylor, R. Lillard, K. Walter, M. Nastasi, J. Phys. D 12 (2000) L591.

[117] S. Lim, D. McCulloch, M. Bilek, D. McKenzie, J. Appl. Phys. 93 (2003) 4283.

[118] S. Lim, D. McCulloch, M. Bilek, D. McKenzie, Surf. Coat. Technol. 174 (2003) 76.

[119] S. Mukherjee, F. Prokert, E. Richter, W. Möller, Thin Solid Films 445 (2003) 48.

[120] M. Nastasi, J. Mayer, J. Hirvonen, Ion-solid interactions: Fundamentals and applications, Camebridge University Press, Camebridge, 1996.

[121] A. Anders (Ed.), Plasma Immersion Ion Implantation and Deposition, John Wiley & Sons, Inc., 2000, Ch. 3.

[122] J. Ziegler, J. Biersack, U. Littmark, The Stopping and Range of Ions in Solids, Pergammon Press, New York, 1985.

[123] E. Franke, M. Neumann, M. Zeuner, W. Frank, F. Bigl, Surf. Coat. Technol. 97 (1997) 90.

[124] J. Neidhardt, L. Hultman, B. Abendroth, R. Gago, W. Möller, J.Appl.Phys. 94 (2003) 7059.

[125] F. Chen, Plasma diagnostic techniques, Academic, New York, 1965, Ch. 4.

[126] J. Swift, M. Schwar, Electrical Pobes for Plasma Diagnostics, Elsevier, New York, 1971.

[127] J. Laframboise, Report No. 100, University of Toronto, Institute for Aerospacestudies, 1966.

[128] R. Clements, J. Vac. Sci. Technol. 15 (1978) 193.

[129] T. Minea, J. Bretagne, L. Magne, D. Pagnon, M. Touzeau, Surf. Coat. Technol. 116 (1999) 558.

[130] I. Ivanov, S. Statev, V. Orlinov, Vacuum 43 (1992) 837.

[131] R. Hoppler, S. Pfau, M. Schmidt, K. Schoenbach, Low temperature plasma physics, Wiley-VCH, Berlin, 2001.

[132] C. Vallance, P. Harland, M. R., J. Phys. Chem. 100 (1996) 15021.

[133] C. Fitz, W. Fukarek, A. Kolitsch, W. Möller, Surf. Coat. Technol. 128-129 (2000) 474.

[134] Y. Yap, T. Aoyama, Y. Wada, M. Yoshimura, Y. Mori, T. Sasaki, Diam. Relat. Mater. 9 (2000) 592.

[135] J.A. Woollam Co., Inc., Lincoln, NE, USA, Guide to using WVASE.

[136] I. Herman, Optical diagnostics for thin film processing, Academic Press, San Diego, USA, 1996.

[137] Data in Science and Technology, Semiconductors, Group IV Elements and II-V Compounds, Springer, Berlin, 1991.

[138] G. Doll, Properties of group III nitrides, INSPEC, London, U.K., 1994, Ch. 6.1.

[139] J. Zapien, R. Messier, R. Collins, Appl. Phys. Lett. 78 (2001) 1982.

[140] J. Zapien, R. Collings, R. Messier, J. Vac. Sci. Thechnol. A 20 (2002) 1395.

[141] K.-L. Barth, W. Fukarek, H.-P. Maucher, M. Plass, A. Lunk, Thin Solid Films 313 (1998) 697.

[142] P. Gielisse, S. Mitra, J. Plendl, R. Griffis, L. Mansur, R. Marshall, E. Pascoe, Phys. Rev. 155 (1967) 1039.

[143] R. Geick, C. Perry, G. Rupprecht, Phys. Rev. 146 (1966) 543.

[144] W. Dworschak, K. Jung, H. Ehrhardt, Thin Solid Films 254 (1995) 65.

[145] A. Lunk, P. Bachem, P. Scheible, L. Ulrich, Appl. Phsy. A 72 (2001) 557.

[146] M. Plass, W. Fukarek, A. Kolitsch, W. Möller, Nucl. Inst. Method B 127-128 (1997) 857.

[147] C. Fitz, W. Fukarek, W. Möller, Diam. Relat. Mater. 11 (2002) 1532.

[148] J. Sanjuro, E. Lopez-Cruz, P. Vogel, M. Cardona, Phys. Rev. B 28 (1983) 4579.

[149] S. Fahy, Phys. Rev. B 53 (1996) 11884(E).

[150] M. Cardona, E. Anastassakis, Phys. Rev. B 54 (1996) 14888.

[151] P. Widmayer, P. Ziemann, S. Ulrich, H. Erhardt, Diam. Relat. Mater. 6 (1997) 621.

[152] A. Klett, R. Freudenstein, M. Plass, W. Kulisch, Surf. Coat. Technol. 125 (2000) 190.

[153] U. Kreissig, R. Grötschel, B. Behrisch, Nucl. Instr. and Meth. B 85 (1994) 71.

[154] L. Doolittle, Nucl. Instr. and Meth. B 9 (1985) 344.

[155] H. Dosch, Critical Phenomena at Surfaces and Interfaces, Evanescent X-Ray and Neutron Scattering, Springer, Berlin, Heidelberg, New York, 1992.

[156] H. Ibach, H. Lüth, Festkörperphysik, Springer, Berlin, Heidelberg, New York, 1995.

[157] A. Mamalis, A. Branis, D. Manolakos, J. Mat. Process. Technol. 123 (2002) 464.

[158] M. Bilek, Correlations between stress and microstructure in thin film materials: The chicken or the egg, FZR seminar, not published (2003).

[159] Joint Committee on Powder Diffraction Standards, JCPDS, pattern 25-1033.

[160] T. Wittkowski, P. Cortina, J. Jorzick, K. Jung, B. Hillebrands, Diam. Relat. Mater. 9 (2000) 1957.

[161] L. Terminello, A. Chaiken, D. Lapiano-Smith, G. Doll, T. Sato, J. Vac. Sci. Technol. A 12 (1994) 2462.

[162] A. Chaiken, L. Terminello, J. Wong, G. Doll, C. Taylor II, Appl. Phys. Lett. 63 (1993) 2112.

[163] J. Stöhr, NEXAFS Spectroscopy, Springer, Berlin, 1992.

List of Tables

List of Figures

Erklärung

Hiermit versichere ich, die vorliegende Arbeit ohne unzulässige Hilfe Dritter und nur unter Benutzung der Angegebenen Hilfsmittel angefertigt zu haben. Die aus fremden Quellen oder indirekt übernommenen Gedanken sind als solche kenntlich gemacht. Die Arbeit wurde weder im Innland noch im Ausland in gleicher oder ähnlicher Form einer anderen Prüfungsbehörde vorgelegt. Die Arbeit wurde am Institut für Ionenstrahlphysik und Materialforschung des Forschungszentrums Rossendorf unter der wissenschaftlichen Betreuung von Herrn Prof. Dr. W. Möller angefertigt. Die Promotionsordnung der Fakultät für Mathematik und Naturwissenschaften der Technischen Universität Dresden vom 20.03.2000 erkenne ich an.

Dresden, den 17.2.2004

Acknowledgment

I would like to thank all people in the institute who contributed to the success this work. I am indebted specially to a number of people for scientific, practical, theoretical, experimental, and moral support:

- To Prof. W. Möller for the opportunity to work in the Institute for Ion Beam Physics and Materials Research of the Forschungszentrum Rossendorf. Also I would like to thank Prof. Möller for helpfull and comprehensive discussions.

- To W. Fukarek for the conception of this project and the excellent preparation of the experimental equipment beforehand. Also I would like to thank him for the excellent and fruitful supervision during unfortunately only a few weeks.

- To Raul Gago for very engaged supervision and scientific discussions and the introduction into the science of XANES. Also I am indebted to him for the opportunity to participate in beam times at LURE and the ESRF.

- To Andreas Kolitsch for helpful discussions and collegial supervision

- The FWII- team for a very collegial and pleasant working atmosphere.

- To Jörg Brutscher for the construction of this unique pulsed power supply and even more for the absolute reliable performance of the power supply.

- To Manfred Seidel for his help during the construction of the stress measurement system and for his help with all electrical difficulties.

- To Günther Anwand and Jürgen Grahl for mechanical constructions at the deposition chamber, the supply with media, and the mechanical construction of the stress measurement system.

- To Bernd Schmidt and Gabi Schnabel for the preparation of the cantilever structures.

- To Uli Kreissig and Max Mäder for ERD analysis and RBS spectroscopy and their help in understanding ion beam analysis.

- To A. Mücklich for engaged TEM analysis, although cBN thin films are not a very rewarding material for TEM.

- To F. Eichhorn and F. Prokert for XRD measurements in the Rossendorf lab but also for analysis and discussion concerning the ESRF beam time. And specially to F. Eihhorn for measuring an extra sample during his own beam time at ROBL and thus completing our results.
- To Thierry Chevolleau and J. Kourtev for their help during the plasma analysis. Special thanks to Thierry Chevolleau for his lectures on how to write a scientific paper.
- To Subroto Mukherjee and Anatoli Rogozin for very helpful discussions on plasma physics.
- To Clemens Fitz for help and discussions and specially for overcoming initial difficulties with cBN.
- To Nushy, Milko, and Manfred for refreshing scientific and non-scientific coffee breaks.
- To Martin for his help using LaTeX and specially for patiently bearing and comforting a stressed and nervous wife.
- To my familly
- To Eva for being a best friend.
- To Ursel and Sputnik

Furthermore, I would like to thank the Deutsche Forschungsgemeinschaft, DFG, for the financial support under the contract number DFG/FU303.

Theses

1. The aim of the presented work was to deposit cubic boron nitride thin films by magnetron sputtering under simultaneous stress relaxation by ion implantation.

2. In order to get a closer understanding of the film growth, first a plasma analysis was performed. The results yield the basic physical parameters of the film growth like the ion to neutral arrival ratio and the ion energy distribution.

3. An in situ instrument for stress measurement based on laser deflectometry and in situ ellipsometry, developed for IBAD experiments, was adjusted for magnetron sputter deposition. An important insight was that for the detection of the reflected laser beam with a position sensitive diode, one has to take into account the signal that is induced by light emission from the plasma.
   The characteristic evolution of the instantaneous stress during the layered growth of cBN films observed in IBAD experiments, could be reproduced for magnetron sputter deposition.

4. To achieve simultaneous stress relaxation, a complex bipolar pulsed substrate bias source was constructed. This power supply enables the growth of cBN thin films under low energy ion irradiation and, for the first time, the simultaneous implantation of ions with an energy of up to 8 keV during high voltage pulses.

5. It was demonstrated that the instantaneous stress in cBN thin films can be released down to -1.1 GPa by simultaneous ion bombardment during the high voltage pulses. A simultaneous stress relaxation during growth is possible in the total investigated ion energy range between 2.5 and 8 keV. These are the lowest ion energies reported for the stress relaxation in cBN. Since such a substrate bias power supply is easy to integrate in existing process lines, this result is important for industrial deposition of thin films, not only for cubic boron nitride films. Also bias voltages in the order of some kV are feasible in commercial production.

6. Using in situ cantilever bending it was found that the amount of stress relaxation depends on the damage that is induced by the high energy ion bombardment and is therefore dependent on the ion energy and the high energy ion flux. In practise this means that the stress relaxation is controlled by the product of the pulse voltage and the pulse duty cycle or frequency. This means that the same stress relaxation can be achieved with different ion energies if the same number of dpa is introduced by the energetic ion implantation, i.e. if the duty cycle is adjusted accordingly.
   In the low damage range, below 0.8 dpa, the relaxation increases with the number

of displacements. In the high damage range, dpa > 0.8, however no further stress relaxation can be achieved.

7. The cantilever bending measurements were complemented on microscopic scale by x-ray diffraction. The analysis of the cBN (111) Bragg diffraction peak revealed a pronounced biaxial compressive state of stress in a non-relaxed cBN film. Post deposition annealing at 900°C of a sample with an ion induced damage of 1.2 dpa, resulted in a complete relaxation of the lattice with equal in-plane and out-of-plane lattice parameters. The obtained d(111) value are considered as a reference for stress-free cBN films produced by magnetron sputtering. In the case of medium-energy ion bombardment, the in-plane and out-of-plane lattice parameters approach the value of the annealed sample with increasing the ion induced damage as a signature of the stress relaxation.

8. The stability of cBN under ion bombardment was investigated by IR spectroscopy. It was found that for a dynamic damage above 0.8 dpa the cBN is partially transformed to hBN. The transformation rate increases with increasing damage. That means that below 0.8 dpa the stress is released in the cBN, whereas for higher damage instead of further stress relaxation only a transformation to hBN takes place. On the other hand, the full width at half maximum of the XRD diffraction peaks remains constant independent of the ion bombardment, point to a pronounced stability of crystalline cBN. It is therefore proposed that in between the grains a short-range ordered, sp^3/sp^2-mixed phase exists, which could be similar to taC and could become more and more sp^2-like with increasing damage.

9. Comparing the results from substrate curvature measurement, XRD, and IR spectroscopy possible mechanisms of stress relaxation were discussed. The observed stress relaxation could be the result of two different processes. On the one hand, during the collision cascade and the subsequent thermal spike the compressive stress due to interstitial-type defects and overcoordinated atoms could be released within the grains. On the other hand, the collision cascades affect also low ordered material in between the cBN crystallites. And here atomic rearrangements could induce a transformation of short-range ordered sp^3/sp^2 bonded material to short-range ordered sp^2 bonded material, which maintains a residual compressive stress due to the low degree of ordering.

10. High energy argon ions seem to enhance the phase transformation to hBN. However, they are not required for the nucleation and growth of the cBN in this system. Also the stress can be released to about -2 GPa by using only nitrogen ions (i.e. using a pure N_2 discharge).

11. From the analysis of the near surface region by XANES, it can be concluded the stress relaxation by the energetic ion bombardment is less at the surface than in the bulk film. This is explained with the dynamic profile of the ion induced damage, that reaches the stationary bulk value in 15-20 nm depth, whereas it is decreasing towards the surface. This fits with the results that the stress relaxation is dependent on the amount of ion induced damage.

12. The influence of the growth assisting (the low energy) ions on the film stress and phase bonding structure have been investigated. In the range between 100 and 200 eV (bias voltage plus plasma potential) the cBN content and the growth rate increase with decreasing ion energy. The instantaneous stress has a maximum at $\sim$ -120 V and decreases for lower and higher bias voltages, in qualitative agreement with the Davis model. This leads to 2 conclusions: first, the stress in the film is not a function of the cBN content; and second an enhanced sputtering at the film surface promotes hBN growth on the expense of cBN.

13. Although the stress in the films was released to values, which are typical for other hard coatings (e.g. TiN), the film adhesion was still not sufficient for any application. There are two possible reasons for this. On on side stress gradients can build up in the film, since the hBN and the hBN/cBN interface are not treated with the energetic ion bombardment. But probably more important is the sensitivity to moisture. Since our samples are stable after annealing at 900° C and also other groups report the production of stable films even though they have very high stress, it is concluded that the microstructure and stoichiometry can promote a chemical reaction with ambient H and O species.

14. The deposition of an hBN buffer layer before the cBN nucleation can help to improve the adhesion. The deposition of multi layered hBN/cBN structures could help to reduce the stress gradients over the total film thickness. Further it is suggested to use instead of an hBN buffer layer a carbon containing buffer layer, since those are reported to be inert against moisture.